DISCLAIMER NOTICE

THIS DOCUMENT IS BEST QUALITY AVAILABLE. THE COPY FURNISHED TO DTIC CONTAINED A SIGNIFICANT NUMBER OF PAGES WHICH DO NOT REPRODUCE LEGIBLY.

MICROWAVE PROPERTIES OF CERAMIC
NONLINEAR DIELECTRICS

By
D. A. Johnson

Technical Note

Contract AF 49(638)-415
Project Number 47501

M.L. Report No. 825
July 1961

Microwave Laboratory
W. W. HANSEN LABORATORIES OF PHYSICS
STANFORD UNIVERSITY
STANFORD, CALIFORNIA

2 2 3 0 0

5 7 5 1 0 0

Microwave Laboratory
W. W. Hansen Laboratories of Physics
Stanford University
Stanford, California

MICROWAVE PROPERTIES OF CERAMIC NONLINEAR DIELECTRICS

By

D. A. Johnson

July 1961

M. L. Report No. 825

ABSTRACT

This investigation was undertaken to develop and apply new measurement techniques for obtaining the small-signal and large-signal microwave characteristics of ceramic nonlinear dielectrics. To this end, three different studies were made.

A transmission method for measuring the small-signal complex dielectric constant was derived and is described in detail. Measurements were made on representative ceramics in the X-band frequency range, and the results are given as curves of the real part of the relative dielectric constant and of the loss tangent as functions of temperature with dc bias levels up to 32 kv/cm.

An experimental curve of the relative dielectric constant of a 73% barium titanate-27% strontium titanate ceramic was obtained for the frequency range of 3 kMc to 270 kMc. The millimeter wavelength characteristics were obtained by measuring the transmission through a modified Fabry-Perot interferometer and show that the relative dielectric constant remains at approximately 2000 up to 60 kMc, but then decreases with increasing frequency to a value of 500 at 270 kMc. A curve showing the per cent change of the relative dielectric constant over the temperature range from 95°F to 125°F (the Curie temperature is approximately 72°F) was also obtained. The curve shows that this measure of the temperature nonlinearity has a maximum of 40% at 60 kMc but decreases rapidly with increasing frequency to become zero at 150 kMc, thus indicating that the polarization mechanism giving rise to the peak of the dielectric constant at the Curie temperature undergoes a relaxation in this frequency interval.

The large-signal microwave characteristics of a nonlinear dielectric were measured at 3 kMc by using a re-entrant coaxial cavity in which a cylindrical post of the ceramic was placed in the region of high electric field intensity. An equivalent circuit for the cavity was derived, and power series expansions were made for the large-signal dielectric constant and rf conductivity of the ceramic and included in the nonlinear differential equation describing the equivalent circuit. A condition on the solution of the differential equation was obtained which describes the response of the cavity to a constant level of incident power. The linear terms in the differential equation were evaluated with small-signal

- iii -

measurements, and curves of the large-signal response of the cavity were obtained as functions of frequency and incident power. The first-order nonlinear terms in the expansions for the large-signal dielectric constant and rf conductivity were evaluated by fitting theoretical curves calculated from the condition on the solution of the differential equation to the experimental curves of the cavity response. The resulting value of the rf conductivity is $8.5 + (5.7 \times 10^{-12} \pm 2.4 \times 10^{-12})E^2$ mhos/meter and that of the dielectric constant is $\epsilon_0[2200 - (6.5 \times 10^{-11} \pm 1.6 \times 10^{-11})E^2]$, where E is the electric field intensity in volts/meter and ϵ_0 is the dielectric constant of free space.

TABLE OF CONTENTS

LIST OF FIGURES

INTRODUCTION

In the last few years increased interest has focused on the use of ferroelectrics in microwave devices. The fundamental characteristic of a ferroelectric is that the curve of the material's polarization resulting from the application of a low-frequency electric field has the shape of a hysteresis loop. When a ferroelectric crystal is heated through a particular temperature, called the Curie temperature (or simply T_c), the polarization will reach a sharp peak and then drop. Above T_c the material will no longer be ferroelectric; however it may exhibit non-linearity with respect to the applied electric field over a considerable temperature range. In addition, the rf losses in the material decrease above T_c. Ferroelectric ceramics display the same general characteristics but the Curie temperature is not so well defined, and the peak of polarization at T_c is neither as high nor as sharp as that of the corresponding crystal.

It is this nonlinearity above T_c, i.e., the dielectric constant being a function of the applied electric field strength, that is of interest for microwave devices. Among the many possible small-signal applications of nonlinear dielectrics are cavity tuning, phase shifting, tunable filtering, and switching; and possible large-signal applications include frequency multiplying and parametric amplifying.

The use of ceramic nonlinear dielectrics has several advantages over other presently available nonlinear elements: the ceramics can be cut or ground to almost any desired shape, they require no bulky and expensive biasing equipment since they are biased by electric fields, and their dc resistance is typically 10^{12} ohm cm, so that the current drain on a bias supply is small. They have high-power handling capabilities, can be tuned rapidly, are isotropic when no bias is applied, and are relatively simple to make.

At present there are several disadvantages. Most nonlinear ceramics now offered commercially have high dielectric constants and relatively high loss. Although a high dielectric constant is desirable for some applications, such as capacitor miniaturization, it is a decided disadvantage

at microwave frequencies because of the difficulty met in matching into
and out of the materials and because an electrically large element will
usually be physically small and may require precision fabrication. The
ceramics are temperature sensitive; however, often they can be manufac-
tured to have a high enough operating temperature so that temperature
stabilization can be obtained with a simple thermoswitch and heating
element. Single crystals of a few ferroelectrics are available; but they
are difficult to grow, expensive, small in size, and strongly anisotropic
even without bias. They also have a higher dielectric constant than the
corresponding ceramic and are extremely temperature-sensitive.

There were three main objectives to this project:

(1) To develop a technique for measuring the small-signal complex
dielectric constant of low-loss, nonlinear, ceramic dielectrics; to obtain
curves of the dielectric constant as a function of temperature and dc bias
in the 8 to 12 kMc frequency range; and to derive the expected behavior
when used in several devices.

(2) To measure the frequency variation of the small-signal dielec-
tric constant of a ceramic nonlinear dielectric at millimeter wavelengths.

(3) To develop a technique for measuring the large-signal behavior
of one of the ceramics used in the small-signal measurements, and to
obtain curves with which the expressions derived to describe the large-
signal behavior can be evaluated.

Each of the following three chapters in this report describes the
manner in which one of the above objectives was attained.

In Chapter II the derivation and use of a new type of transmission
measurement technique is described. This technique is particularly well
suited for quickly measuring the small-signal complex dielectric constant
of high-permittivity ceramics. The measurement results for several repre-
sentative materials are given in the form of curves of the real part of
the relative complex dielectric constant and the loss tangent as a function
of temperature and bias. The results for a ceramic of 73% barium titan-
ate-27% strontium titanate are used to predict theoretically the behavior
of a phase shifter and a tuned cavity.

In Chapter III the measurements made at millimeter wavelengths are
reported and the results plotted as functions of frequency. One curve
gives the relative dielectric constant and a second shows the per cent

- 2 -

change of the relative dielectric constant in a stated temperature interval. The frequency varied from approximately 50 to 270 kMc.

In Chapter IV a new measurement technique is described for obtaining the coefficients of the two-power-series expansions used to describe the nonlinear behavior of a ceramic dielectric when subjected to large signals. The measurements were made with a coaxial re-entrant cavity that contained a cylinder of the dielectric. The power-series expansions for the nonlinear capacitance and the nonlinear conductance representing the dielectric in a lumped equivalent circuit of the cavity are used in the differential equation of the circuit, and a condition on the solution of the differential equation is derived. Curves of the response of the cavity were obtained and are given as a function of the drive frequency for various incident power levels. These curves were then used with the condition on the solution of the differential equation to obtain the coefficients in the power-series expansions. The cavity and its design are described as is the method used to fabricate the dielectric cylinders.

The derivations are, for the most part, given in the appendices.

SMALL-SIGNAL MICROWAVE CHARACTERISTICS

A. INTRODUCTION

The design of small-signal microwave devices employing a nonlinear element is greatly facilitated by the use of curves that specify the electrical characteristics of the element as a function of its design parameters.

In the case of a ceramic nonlinear dielectric, the macroscopic small-signal electrical characteristics can be described by the dielectric constant, relating the electric flux density, $\vec{D}$, and the electric field intensity, $\vec{E}$:

$$\vec{D} = \epsilon\vec{E} = \epsilon_0\kappa\vec{E} , \tag{1}$$

where ϵ_0 is the dielectric constant of free space,

          κ is the relative dielectric constant.

In general, ϵ can vary with both the magnitude and direction of the electric field intensity vector. However, since the small-signal characteristics were desired, the rf power levels used for the measurements described in this chapter were sufficiently small (one milliwatt or less) so that $\partial D/\partial E$ could not vary during an rf cycle. In this chapter, therefore, the value of ϵ is considered to be a constant at any given temperature and dc bias voltage. It is customary to include the effects of the loss mechanisms in a material by defining the complex dielectric constant

$$\epsilon = \epsilon' - j\epsilon'' \tag{2}$$

or the complex relative dielectric constant

$$\kappa = \kappa' - j\kappa'' . \tag{3}$$

The losses in a material can also be described by the loss tangent

$$\tan \delta = \frac{\epsilon''}{\epsilon'} = \frac{\kappa''}{\kappa'} . \tag{4}$$

It is easily shown that ϵ'' , or $\tan \delta$, corresponds to a loss by using Eq. (2) in the Maxwell curl equation,

$$\nabla \times \vec{H} = \frac{\partial \vec{D}}{\partial \tau} = \frac{\partial \epsilon\vec{E}}{\partial \tau} = j\omega\epsilon\vec{E} = (j\omega\epsilon' + \omega\epsilon'')\vec{E} = (j\omega\epsilon' + \sigma)\vec{E} , \tag{5}$$

- 4 -

where $\overset{\rightharpoonup}{\mathbb{E}}$ is assumed to vary in time as $e^{j\omega t}$ and

  σ is the dielectric conductivity;

hence,

$$\sigma = \omega\epsilon'' = \omega\epsilon' \tan\delta . \qquad (6)$$

The desired electrical characteristics of the ceramics are completely specified by the real part of the relative dielectric constant, κ' , and the loss tangent, $\tan\delta$.

The κ' and $\tan\delta$ of these materials undergo radical changes with variations of either the temperature or an applied dc electric field; hence dc bias and temperature are the design parameters sought and should be controlled in any measurement technique.

There are many methods available for measuring the dielectric constant of materials at microwa > frequencies.[1-7] However, since the nonlinear ceramics present a large discontinuity to an impinging wave because their relative dielectric constant is usually greater than 1000, the standard techniques which involve a measurement of the standing wave in front of a sample or the motion of a short on the load side of a sample are of little use.

One measurement method, described by von Hippel,[6] used by Jaynes and Varenhorst,[1] and later adopted by other investigators,[5,8,9] involves terminating a coaxial line with a small piece of dielectric placed between the end of the center conductor and a shorting plane. This geometry terminates the line with a capacitive load and allows the dielectric constant to be measured as a function of temperature and dc bias (applied between the center conductor and the shorting plane). This method involves obtaining the magnitude and phase of the impedance of the terminating element by measuring the VSWR and the position of the minimum in the line.

It was felt that there were two basic difficulties with this type of measurement. The first is that, as the frequency of measurement increases, it becomes increasingly difficult to obtain the required accuracy and virtually impossible to employ the method at or above 8 kMc since the measurement tolerances become impossibly small. The second is that most of the materials change their characteristics when subjected to mechanical stress, and such a stress can be applied when the sample is placed in

- 5 -

position for measurement. Furthermore, stresses can be set up within the ceramics either in their manufacture or fabrication. In any case, the result will be that the measured complex dielectric constant will not characterize the unstressed material. A measurement technique should be able to show whether or not the material is anisotropic.

A transmission-type measurement was employed by Powles and Jackson[2] in which a slab of dielectric was placed across a waveguide with the faces of the dielectric perpendicular to the axis of the guide. The transmission through the sample was taken as a function of frequency. As the frequency at which the sample was an integral multiple of half wavelengths long was approached, the transmission rose to a peak. This behavior is analogous to that of the current flow through a lumped-element-series resonant circuit when the frequency of the applied voltage approaches the resonant frequency. The dielectric constant was determined from the frequencies of two adjacent peaks of transmission. They found, however, that their experimental setup was unsuitable for measuring the real part of the relative dielectric constant when greater than 200, and abandoned this method in favor of another that involved the use of dielectric matching sections and the measurement of front-face impedance.

Schmitt[3] also used a waveguide transmission measurement method in which a crystal was placed in back of the sample to measure the trans-mitted power. The match of the crystal was controlled by an E-H tuner; hence his measurements were made at a single frequency, 9.4 kMc, and involved changing the sample thickness to obtain the maximum of tra s-mission. He also applied a dc voltage across the whole sample to obtain the bias dependency of the complex dielectric constant.

Davis and Rubin[4] measured (with a microwave bridge at 3.00 kMc) the shift in phase of a wave traversing a sample of nonlinear dielectric which filled the cross section of a 7/8" coaxial line. The shift in phase and the attenuation through the sample yielded the complex dielectric constant. They applied bias between the inner and outer conductor of the coaxial line and cemented a quarter-wave matching section of a linear dielectric onto both sides of the nonlinear dielectric. This method would be difficult to use at higher frequencies and would require fabri-cating samples for each frequency.

- 6 -

After a consideration of the methods and experiences of these authors and after preliminary experimental investigations, it was decided that a new transmission-type measurement technique should be devised. The sample geometry employed would resemble that used by Powles and Jackson; that is, the sample of ceramic nonlinear dielectric would be placed across the guide with no matching sections. The boundary value problem was solved to yield the complex dielectric constant, and the dependent variables were temperature, dc bias, sample length, and frequency. The instrumentation allowed a very sensitive measurement of transmission to be made when a matched termination was placed behind the sample. It was possible to sweep the frequency continuously over a large range (for example, 8.0 to 10.0 kMc). The transmission through the sample was displayed on an oscilloscope as a function of frequency so that a visual check could be maintained of the sample's behavior with changes of temperature and bias. Any inhomogeneities in the sample due to stresses or other causes distorted the transmission curve and could, therefore, be avoided. The measurement method obtained all the needed data quickly and simply, and can be used in any frequency range provided only that it is physically possible to grind the samples to the size suitable for the waveguide used. All measurements reported in this chapter were made in the frequency range of 7.6 to 12.4 kMc. The resulting curves of the complex dielectric constant were then used to predict theoretically the operation of several devices.

This chapter is devoted to showing how these curves were obtained and utilized.

B. BOUNDARY VALUE PROBLEM

The geometry employed is that of Fig. 1.
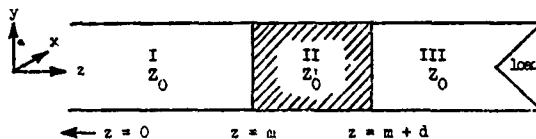
FIG. 1--Schematic diagram of sample configuration.

- 7 -

The nonlinear dielectric entirely fills the waveguide in Region II and extends a length d in the longitudinal direction. In Region II the characteristic impedance, Z_0' , and the propagation constant, Γ' , are both complex. Region III, an air-filled waveguide, is terminated by a matched load and therefore has no standing waves. In Region I, however, there is both an incident wave and a wave reflected from the front face of the dielectric. Regions I and III have a real characteristic imped-ance, Z_0 , as well as a real propagation constant, β . Since the faces of the dielectric are perpendicular to the longitudinal axis of the wave-guide, only the dominant mode should be excited. The wall losses in the waveguide can be neglected when compared to those in the dielectric. The boundary value problem can now be solved to give equations which will yield the real part of the dielectric constant, κ' , and the loss tangent, tan δ , from the experimental data. The solution is carried out in Appendix A and only the results of that solution are given here.

The equations derived in Appendix A for the determination of κ' and tan δ are:

(A.26),

$$\sin n\pi \frac{\Delta f}{f_0} = \frac{a}{15n} , \qquad n = 1,2,3,4\ldots,$$

where f_0 = the frequency of a maximum of transmission, T_{max}

$f_{1/2}$ = the frequency at $T_{max}/2$

Δf = $f_{1/2} - f_0$

a = $\dfrac{2[1 - (f_c/f)^2]^{1/2}}{(T_{max})^{1/2}} d' f_{0,kMc}$

d' = sample thickness in cm

$f_{0,kMc}$ = $f_0 \times 10^{-9}$

f_c = the cutoff frequency of the air-filled waveguide,

and (A.27),

$$(\kappa')^{1/2} = \frac{15n}{d' f_{c,kMc}} ,$$

and, (A.29),

$$\exp[(n\pi/2)\tan \delta] = \frac{H + \sqrt{H^2 + 4G}}{2} ,$$

- 8 -

where $\quad G = \dfrac{1 - F}{1 + F}$

$\quad\quad\quad H = \dfrac{2a/15n}{1 + F}$

$\quad\quad\quad F = \dfrac{a/15n}{(1/T_{max})^{1/2}}$.

The additional assumptions made in the solution of the boundary value problem are

$$\tan^2 \delta \ll 1$$

$$\kappa' = \frac{\epsilon'}{\epsilon_0} \geq 100$$

$$f \gg f_c \, , \text{ i. e., } \quad \omega^2 \mu \epsilon' \gg (\pi/a)^2 \, ,$$

where, in this case, a is the guidewidth. For the nonlinear ceramics measured these assumptions are all valid in the temperature range above T_c .

C. EXPERIMENTAL MEASUREMENT TECHNIQUE

A block diagram of the instrumentation is given in Fig. 2. The source can be either a mechanically swept klystron or a swept backward-wave oscillator. The incident and transmitted power levels are sampled by a 20 db and a 10 db multi-hole directional coupler respectively. The power in each coupler is rectified by one of a matched pair of broadband crystals whose output voltages are fed to the ratiometer. From the ratiometer, a direct reading of the transmission through the sample is obtained as well as a voltage (proportional to the transmission) which is fed to the y-axis of the oscilloscope. The swept oscillator supplies a voltage (proportional to frequency) to the x-axis of the oscilloscope. It is helpful if the cathode ray tube has a long persistence screen. A typical transmission curve as seen on the oscilloscope is shown in Fig. 3. The photograph was made with two exposures; the peak of the transmission curve moved to higher frequencies (i.e., to the left on the photograph) when a dc bias was applied, indicating a lowering of the dielectric con-stant. In a like manner, the peaks of transmission will move across the face of the oscilloscope toward the higher frequencies when the tempera-ture of the sample above T_c is increased. The trace allows a visual

- 9 -
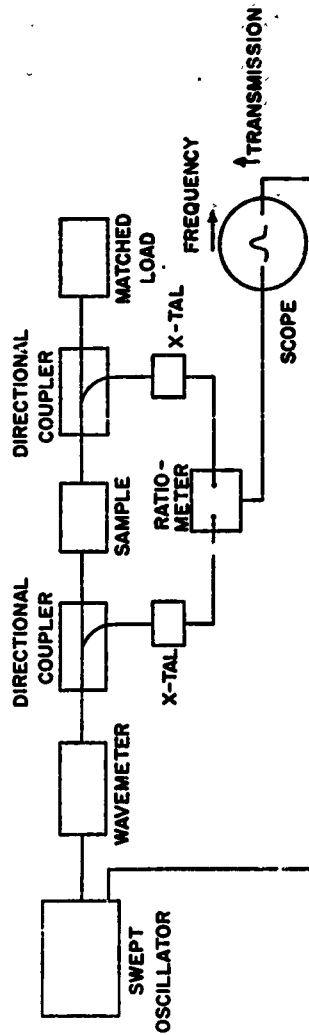
FIG. 2--Block diagram of apparatus used to measure the real part of the complex dielectric constant and loss tangent.
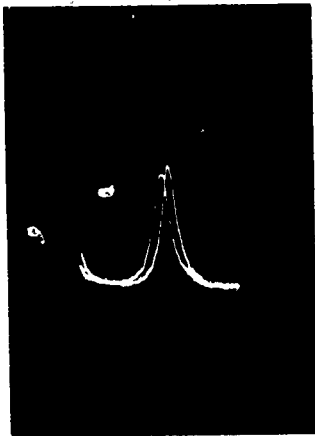
FIG. 3--Photograph of oscilloscope trace showing typical
transmission curves for 0.050" thick ceramic of
73% BaTiO$_3$-27% SrTiO$_3$. Frequency ranges from
7.9 kMc on the right to 12.4 kMc on the left.
The temperature is 155°F. The curve shifts to
higher frequencies upon application of a 10 kv/cm
bias.

check to be maintained while the data are being taken to assure that no
anomalous behavior is taking place in the sample; since--if for any
reason the dielectric constant is inhomogeneous across or through the
sample--the curve of transmission will be distorted, the data-taking
can then be stopped and the difficulty corrected. Inhomogeneities may
appear if the samples are wedged in the waveguide or if internal stresses
exist within a sample after it is fired and cut, in which case the sample
should be discarded.

It can now be seen that the needed data can be taken quickly and
easily. Before a run is made, the number, n , of half wavelengths in
the material must be determined at some temperature in the range of
interest. This can be done in two ways. The first method involves using
Eq. (A.26) and taking the "Q" of one peak of transmission. The tempera-
ture should be stabilized at some convenient point. The swept oscillator
is then set so that the frequency is that of a transmission maximum. The
value of the maximum is read from the previously calibrated ratiometer
and the frequency from the wavemeter. The frequency of the upper half-
power point, where the transmission is down 3 db, is then determined.
Since the sample thickness and the cutoff frequency of the waveguide are
known, the transcendental equation, Eq. (A.26), can now be solved for n .
There is, however, a simpler way to obtain n if two adjacent peaks of
transmission can be viewed at some one temperature, viz., Eq. (A.27) can
be solved for the n and (n + 1) of the two peaks which will yield
the same value of κ' :

$$(\kappa')^{1/2} = \frac{15n}{d' f_{0,kMc(n)}} = \frac{15(n + 1)}{d' f_{0,kMc(n+1)}} , \tag{7}$$

where $f_{0,kMc(n)}$ is the frequency in kilomegacycles of the maximum at
the lower frequency and $f_{0,kMc(n+1)}$ the frequency of the upper maximum.
On solving Eq. (7) for the ratio of n and (n + 1) , one finds

$$\frac{n}{n + 1} = \frac{f_{0,kMc(n)}}{f_{0,kMc(n+1)}} . \tag{8}$$

It should be noted that the latter method for obtaining n assumes that
there is no change in κ' in the frequency range between the two maxima.
Once the n has been obtained for a specific maximum, the n's for all

- 12 -

other maxima can be determined simply by watching how the peaks move with changes in temperature and bias. The only data that are then needed to establish curves of κ' and tan δ are the frequency and transmission of the maxima. Equation (A.27) will yield κ' and Eq. (A.29) can be solved for tan δ .

Experience showed that if the sample with its holder were heated to the maximum desired temperature (for example, $270^{\circ}F$ for 73% barium titanate-27% strontium titanate) and then allowed to drift toward room temperature, all the data needed to plot the curves of κ' and tan δ (when the bias was varied in steps between 0 and 32 kv/cm over the full temperature range of the drift) could be taken in less than three hours. The calculations to obtain the values of κ' can be made quickly; however, it is a tedious, although straightforward and simple job, to calculate the values of tan δ .

D. SAMPLE GEOMETRY AND BIASING METHOD

The sample configuration and method of applying bias is shown in Fig. 4. The sample fills 80% of the guide width; however as shown by Schmitt[3] and verified experimentally, the perturbation by such a filling factor to the fields in the dielectric is negligible. The experimental verification will be described in Section F of this chapter.

The dc bias is applied to the biasing electrode through a small hole in the side of the waveguide without distorting the fields. The electrode geometry is poor from the point of view of arc suppression, and it was difficult to achieve biasing fields of even 10 kv/cm when the guide was filled with air. The introduction of nitrogen gas at gauge pressures up to 60 lbs. per square inch helped a little to suppress the corona and the arcing from the biasing electrode across the surface of the dielectric to the waveguide. But the pressures needed to suppress arcing were great enough to cause the dielectric constant through the sample to be inhomogeneous; therefore, nitrogen could not be used. After much experimentation sulfur hexafluoride gas, SF_6 , was used in the waveguide at one atmosphere pressure (i.e., zero gauge pressure). With SF_6 it was possible to obtain biasing fields of 32 kv/cm without breakdown. It should be noted that while SF_6 is inert, it will break down into lower fluorides and free fluorine in the presence of an arc and that

- 13 -

CERAMIC SAMPLE

WAVEGUIDE

TO BIAS SUPPLY

BIASING ELECTRODE
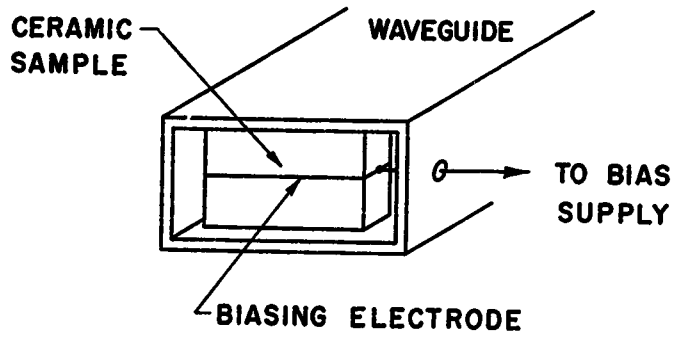
FIG. 4--Sample configuration.

some of the breakdown products can hydrolize into hydrofluoric acid.
The amount of breakdown products formed is roughly proportional to the
amount of power dissipated in the arc. This means that there are two
safety precautions that should be taken when SF_6 is used in this type
of system. The dc bias supply should have a high internal impedance so
that little power will be dissipated in an arc, and the waveguide com-
ponents should be set up in a fume hood so that both the equipment and
personnel will be protected in the event of breakdown.

To prevent arcing from the electrode to the side wall of the wave-
guide opposite the hole, a thin piece of teflon was placed between the
sample and the side of the waveguide. For the other side a flanged bush-
ing of teflon was made which was inserted through the hole from the
inside of the guide. The bushing was drilled to bring in the bias lead.

The sides of the sample which fitted against the waveguide walls
and against the biasing electrode were coated with either a brushed coat
of conducting paint or with a chemically deposited coat of metallic silver
upon which was electroformed a 0.0005" film of copper.

In order to insure the proper fit of sample pieces in the waveguide,
the biasing electrode was made into a weak spring. The sample pieces,
when finished, were each approximately 0.002" less than half the y-
dimension of the waveguide. The electrodes were cut from 0.001" spring
brass shim-stock and were slightly creased down their length (i.e., along
the x-axis of the waveguide). The electrode then became a spring which
would hold the samples firmly against the waveguide without wedging and
stressing the dielectric material.

All samples were cleaned prior to insertion in the sample holder.
They were first boiled in Versene for at least five minutes and then
rinsed in distilled water. They were then boiled in distilled water for
at least five minutes and, immediately upon being removed from the boil-
ing water, were plunged into acetone. After being cleaned, the samples
were stored until used in a container with a dessicating agent.

The waveguide containing the sample was mounted in a block of brass
around which was wound a lead-covered heating cable. A thermoswitch and
thermometer were mounted in the brass block with their sensing areas
directly over that part of the guide containing the sample. A Variac
was used to control the current through the thermoswitch and heating

cable. In this way the temperature could be controlled within $\pm 1^{\circ}$F.
Cooling of the sample was accomplished by packing the sample holder in
dry ice.

E. MEASUREMENT RESULTS

Curves of the real part of the relative dielectric constant, κ' ,
and loss tangent, tan δ , are given as functions of temperature with
varying bias for five ceramics in Figs. 5 through 13. All the data for
these figures were taken in the frequency range of 7.6 to 12.4 kMc.
Unfortunately, since all the ceramics were obtained commercially, it was
not possible to learn how they were fabricated or fired.

Figure 5 gives κ' as a function of temperature for titanium dioxide,
TiO_2 . Although biasing fields were applied over the complete temperature
range from 250°F to -50°F, they had no apparent affect. The loss tangent
is so low that it is only pos ble to give an upper limit of 0.0015" at
74°F since the assumption that the wall losses in the waveguide can be
neglected is probably no longer valid.

Figures 6 through 9 give κ' and tan δ for 73% barium titanate-
27% strontium titanate and κ' and tan δ for 50% barium titanate-50%
strontium titanate respectively. The curves for κ' and tan δ of the
two mixtures have approximately the same shapes and magnitudes; however,
the curves for the 50% $BaTiO_3$-50% $SrTiO_3$ ceramic are shifted downward in
temperature by approximately 55°F from those of the 73% $BaTiO_3$-27% $SrTiO_3$
ceramic. The shift of T_c to a lower temperature with the addition of
$SrTiO_3$ is well known; however, the shift is only about one half that
measured by Davis and Rubin[4] at 9.4 kMc. Their measurements indicate a
T_c of approximately 70°F for 73% $BaTiO_3$-27% $SrTiO_3$, which is in fair
agreement with the 0 bias curve of Fig. 6. However, a T_c of -54°F was
measured by them for 50% $BaTiO_3$-50% $SrTiO_3$, while the curves of Fig. 8
show a T_c of about 0 to 10°F, indicating that the ceramic represented
by Figs. 8 and 9 may, in fact, have had some other ratio than the purported
50% $BaTiO_3$-50% $SrTiO_3$.

Figures 10 and 11 give κ' and tan δ , respectively, f a ceramic
of 2% $NiTiO_3$-72% $BaTiO_3$-26% $SrTiO_3$. The nickel additive served to reduce
κ' and tan δ somewhat while still allowing the dielectric to be non-
linear; however, it was found that arcing would occur across the surface
of this ceramic more easily than the others.

- 16 -
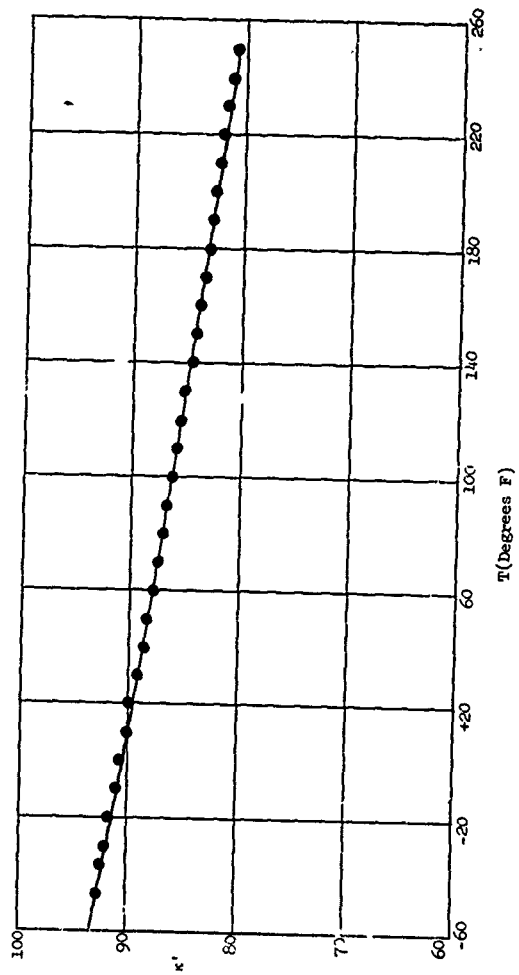
FIG. 5--κ' as a function of temperature for ceramic of TiO_2.
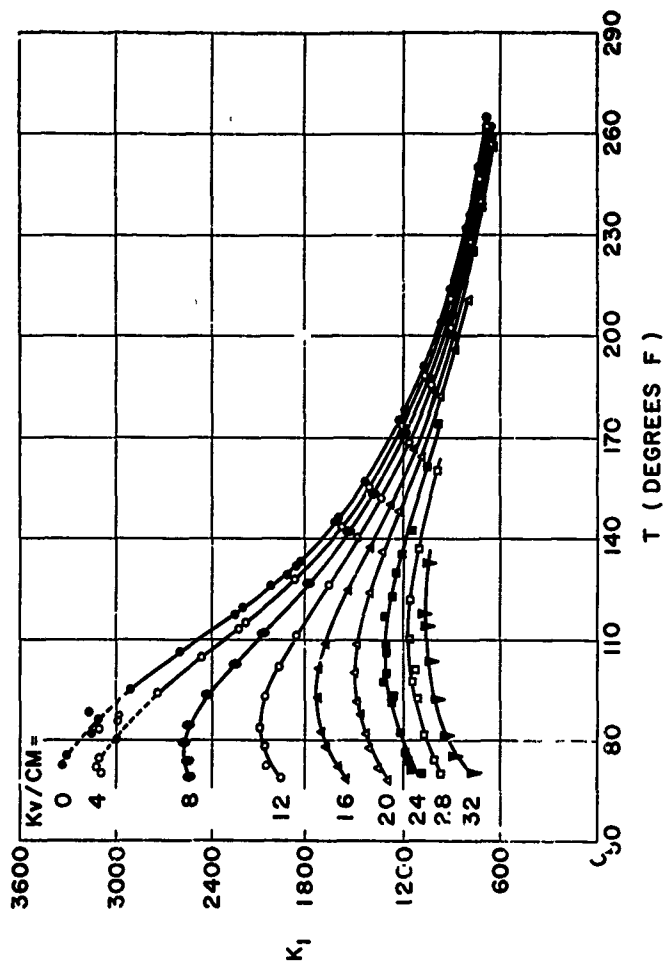
FIG. 6--κ' as a function of temperature with varying dc bias for ceramic of 73% BaTiO₃-27% SrTiO₃ .
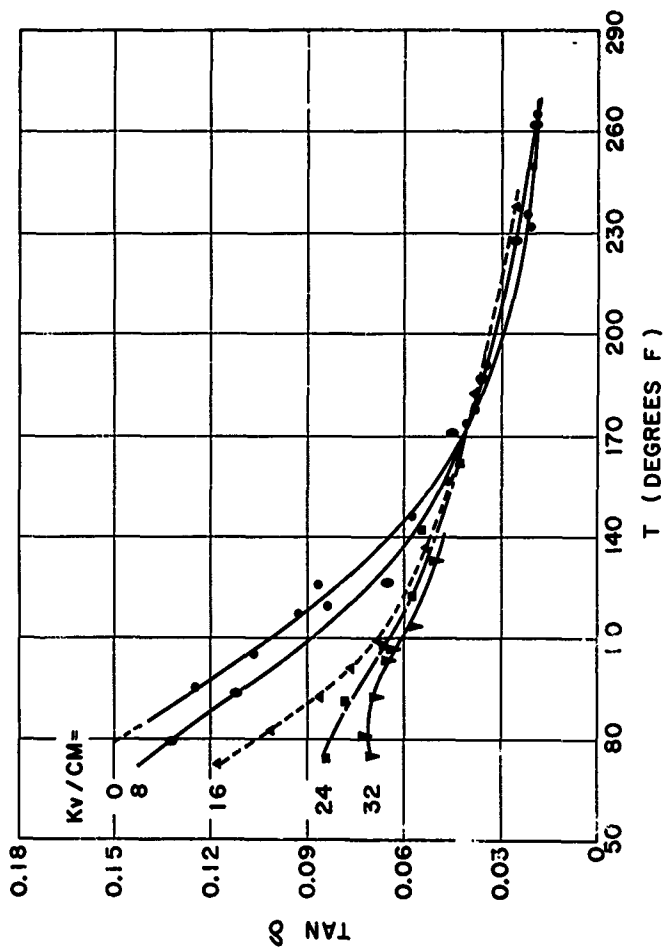
FIG. 7--Tan δ as a function of temperature with varying dc bias for ceramic of 73% BaTiO₃-27% SrTiO₃ .
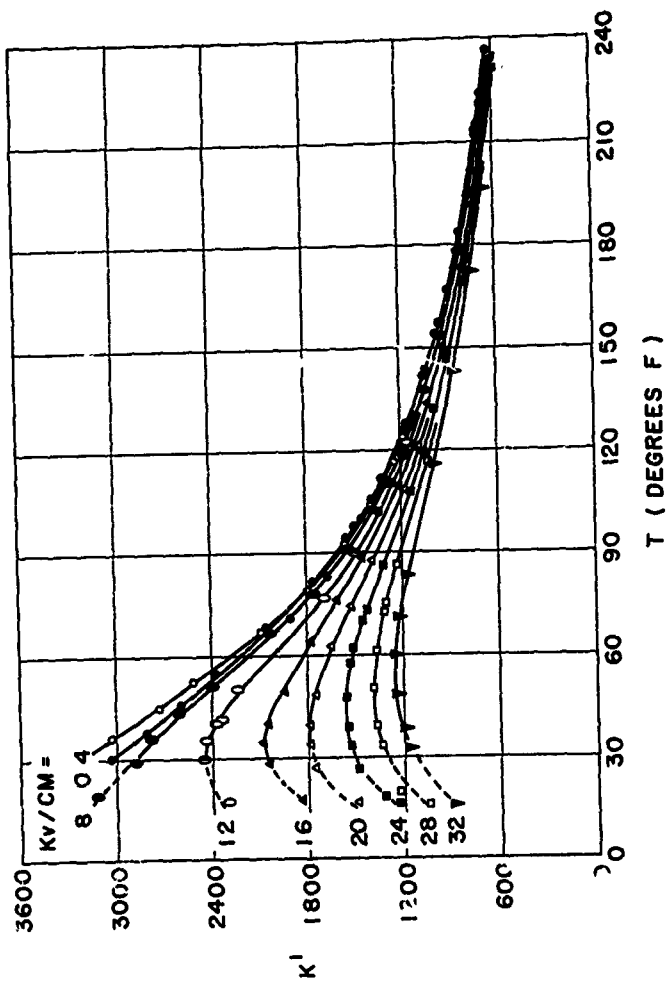
FIG. 8—κ' as a function of temperature with varying dc bias for ceramic of 50% BaTiO$_3$-50% SrTiO$_3$.
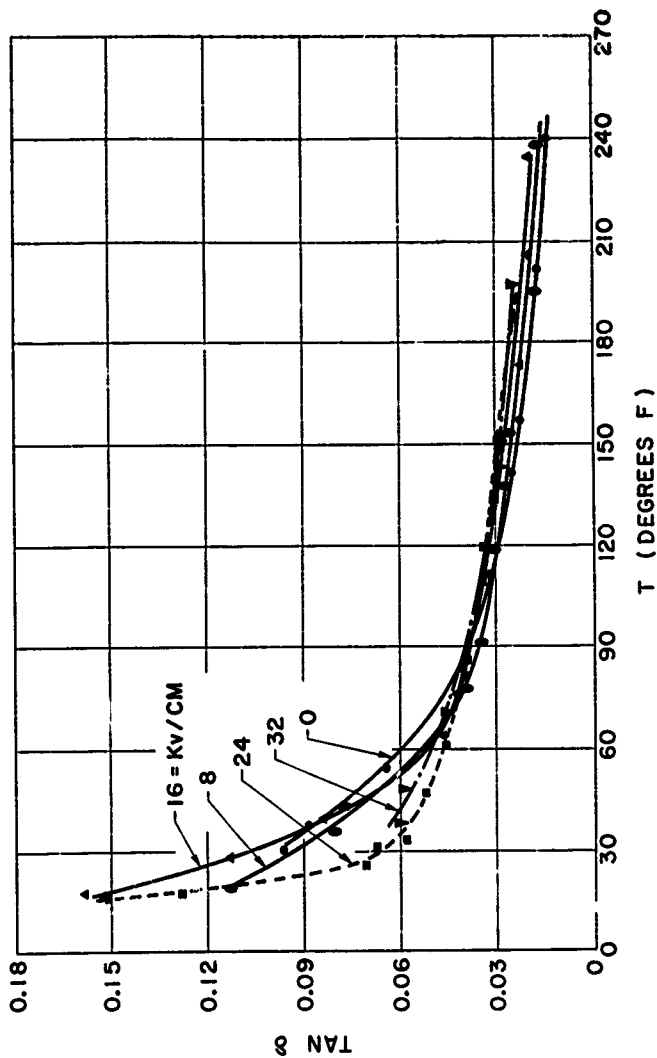
FIG. 9—Tan δ as a function of temperature with varying dc bias for ceramic of 50% BaTiO$_3$-50% SrTiO$_3$.
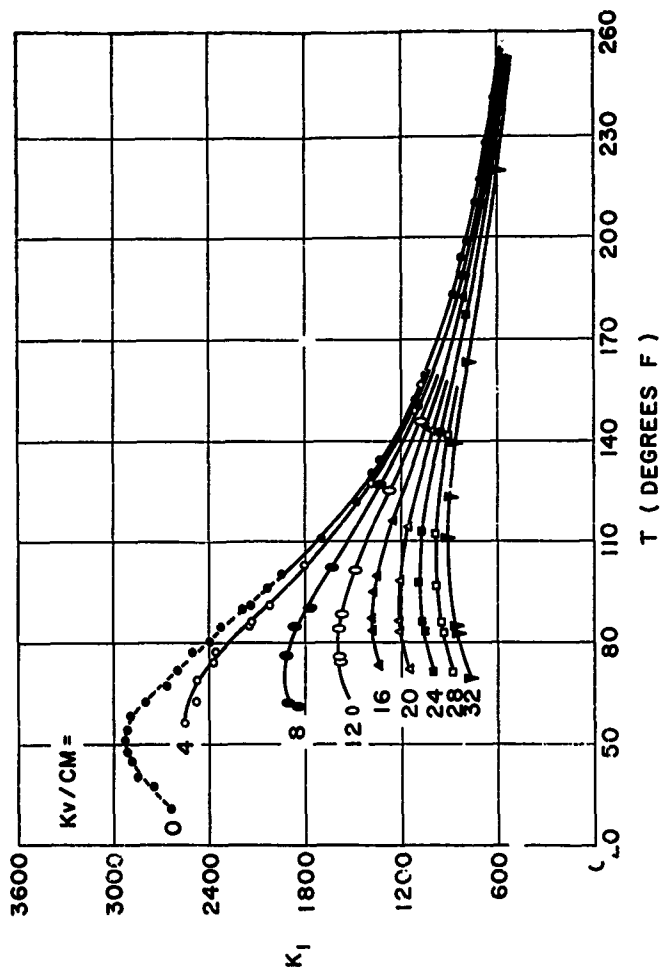
FIG. 10--κ' as a function of temperature with varying dc bias for ceramic of 2% NiTiO$_3$-72% BaTiO$_3$-26% SrTiO$_3$.
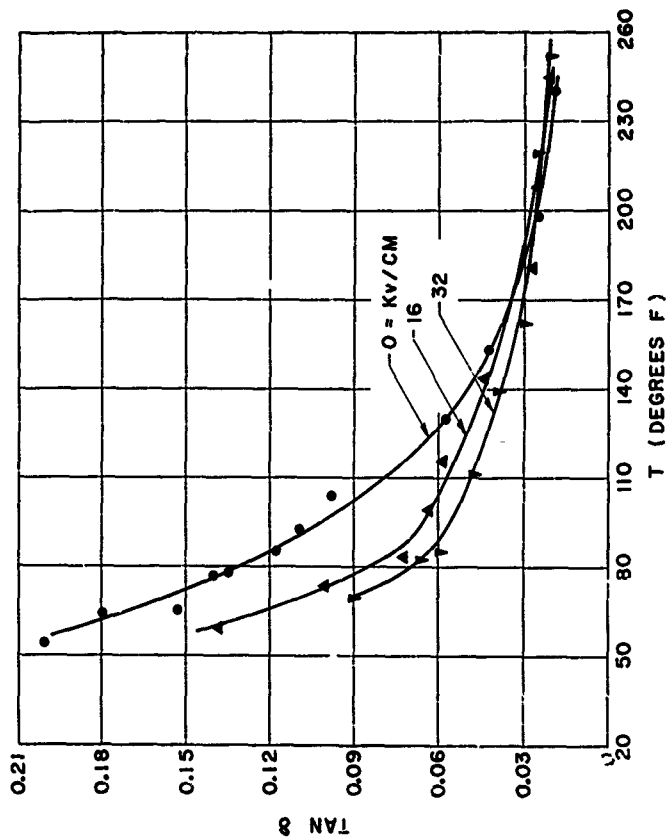
FIG. 11.--Tan δ as a function of temperature with varying dc bias for ceramic of 2% NiTiO₃-72% BaTiO₃-26% SrTiO₃ .
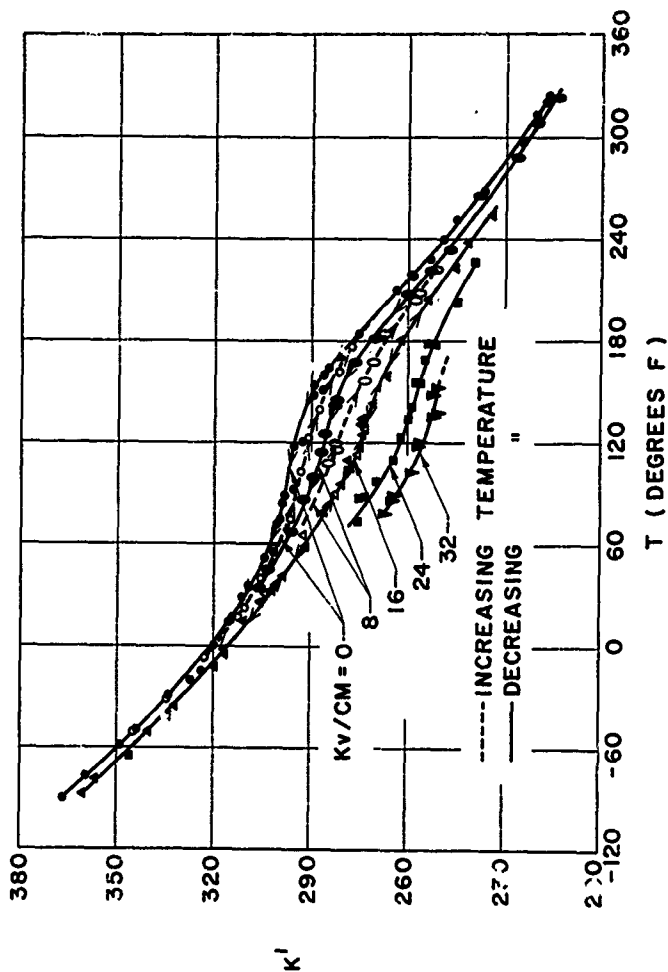
FIG. 12--κ' as a function of temperature with varying dc bias
for ceramic of 50% CaTiO$_3$-36% BaTiO$_3$-14% SrTiO$_3$.
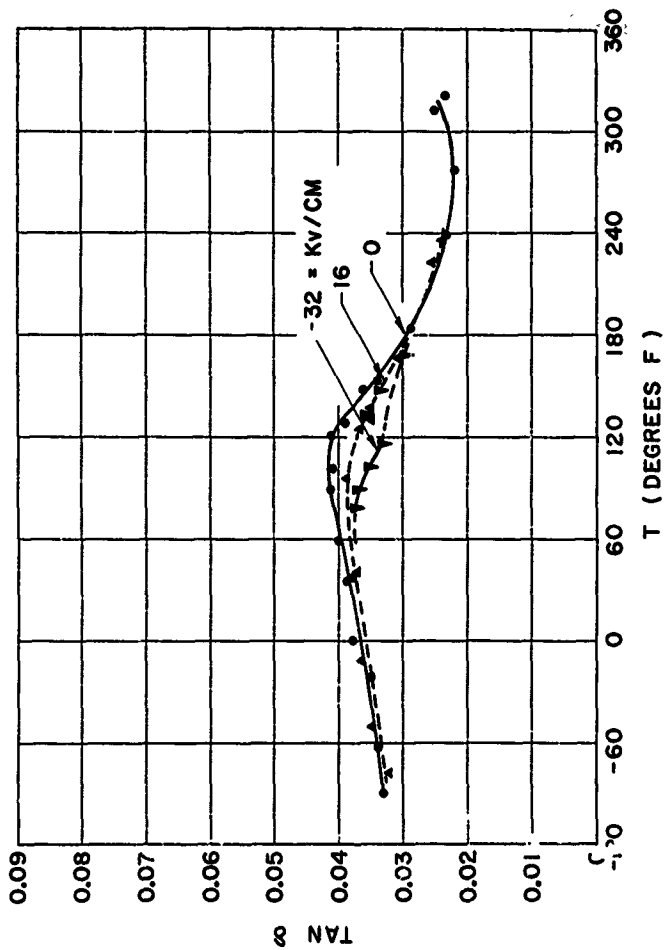
FIG 13--Tan δ as a function of temperature with varying dc bias for ceramic of 50% $CaTiO_3$-36% $BaTiO_3$-14% $SrTiO_3$.

Figures 12 and 13 give κ' and tan δ curves for a ceramic of
50% CaTiO$_3$-36% BaTiO$_3$-14% SrTiO$_3$. The addition of a large amount of
CaTiO$_3$ greatly reduces κ' and also tan δ, yet the material is non-
linear. In addition, the change in κ' and tan δ with temperature in
the range where the material exhibits nonlinearity is fairly small. These
characteristics are very desirable from the point of view of device design,
and indicate that further investigations of this type of mixture may be
warranted. The one undesirable characteristic exhibited by the material
is that a thermal hysteresis occurs for bias fields less than 16 kv/cm.

F. ERROR ESTIMATION

If all the assumptions made in the solution of the boundary value
problem are valid for a given ceramic nonlinear dielectric and if the
equipment is properly calibrat_i prior to taking data, then the major
source of measurement error probably occurs in reading the transmission
and temperature. However, the assumption that the fields in the dielec-
tric were not perturbed when the samples failed to fill the entire width
of the waveguide should be checked. To this end a sample of 73% BaTiO$_3$-
27% SrTiO$_3$ was cut which would entirely fill the cross section of the
X-band waveguide in the sample holder; that is, referring to Fig. 14,
both a and b were unity. The sample had never been subjected to an
electric field.
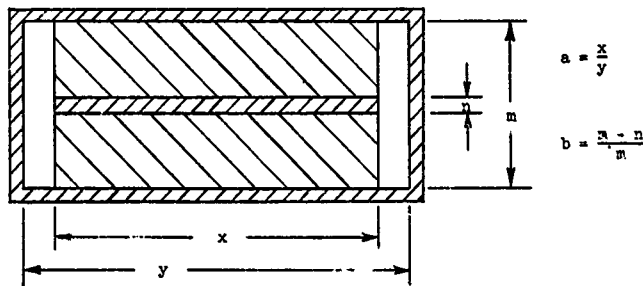
FIG. 14--Diagram of sample configuration.

Curves of the real part of the relative dielectric constant, κ', and the maxima of transmission were taken with the temperature ranging from 260°F to 130°F. The sample was then removed, cut to make the filling factor, a, equal to 0.80, and reinserted. The real part of the relative dielectric constant, κ', and the values of the transmission maxima were again determined over the same temperature range. Once more the sample was removed and cut. In this case, however, the sample was sawed in half to make b equal to 0.96. The sample pieces were painted with conducting paint, reinserted with a copper strip filling the dimension n, and measured as before. The sample was then subjected to a bias field of 16 kv/cm. When the bias field had been removed, the samples were again measured.

An attempt was made to make all measurement runs in the same way. In each case the sample and its holder were heated to 300°F and allowed to drift toward room temperature. In each case the data were taken from 260°F to 130°F, and in each case except the last, where it was not taken out of the guide prior to the run, the sample was cleaned.

The values of the transmission maxima agreed within the reading error. All four curves of κ' agreed within 1% and all data points fell within 2% of their curves, indicating that the application of a bias field had no long-term effect upon the ceramic and that the sample geometry employed did not add appreciable error to the measurements.

The maximum temperature gradient between the sample and the thermometer was approximately 3°F. Since all the measurement runs were made by first heating the sample holder to the maximum, then allowing it to drift to the low temperature, this error is a consistent one. The reading error of the thermometer is estimated to be $\pm 0.2^\circ$F and the thermometer is guaranteed to be accurate within 1%.

The maximum total error in the values of the real part of the relative dielectric constant, κ', is estimated to be $\pm 3\%$, while that of the loss tangent, $\tan \delta$, is estimated to be $\pm 10\%$. These estimates are made on the basis of the scatter of the data, the shift of the curves due to the temperature gradient between the sample and the thermometer, and the reproducibility of the results.

- 27 -

G. THEORETICAL APPLICATION OF MEASUREMENT RESULTS

1. Electrically-Tuned Cavity

The formula describing the behavior of a cavity which is tuned electrically by varying the bias field across a nonlinear dielectric element in the cavity is derived in Appendix B* and presented in Eq. (B.10):

$$\frac{\Delta f}{f} = -\frac{1}{2}\frac{1}{Q \tan \delta}\frac{\Delta \epsilon'}{\epsilon'} \, ,$$

where ϵ' is the real part of the complex dielectric constant,

$\epsilon = \epsilon' - j\epsilon''$,

$\Delta\epsilon'$ is the incremental change in ϵ' occurring with an incremental change in bias,

Q is the unloaded Q of the cavity when it contains the dielectric,

f is the resonant frequency of the cavity,

Δf is the resulting incremental change in the resonant frequency of the cavity.

The assumptions made in the derivation are that the wall losses in the cavity can be neglected when compared to the losses in the dielectric and that the loss tangent of the dielectric material is not much greater than 0.1.

Figure 16 shows the expected change in the resonant frequency of a cavity with changing bias for various values of $Q \tan \delta$. From Eq. (B.10) it is seen that for a given system a desirable operating point is found when $\tan \delta$ is low and the nonlinearity is high. Therefore, an operating temperature of $120^{\circ}F$ was chosen for the 73% BaTiO$_3$-27% SrTiO$_3$ ceramic which was assumed to be the nonlinear element in the cavity of Fig. 16. To facilitate the calculations for Fig. 16, the curves of κ' given in Fig. 5 were replotted in Fig. 15 to give κ' as a function of the bias field at various temperatures. When all the electrical energy is stored in the dielectric, $Q \tan \delta$ is equal to 1; however, if the cavity is designed to store some electrical energy outside the dielectric Q is increased with a resultant increase in $Q \tan \delta$. In the calculation of the curves of Fig. 16 it was assumed that $Q \tan \delta$ is constant over the

*Credit for the derivation in Appendix B is given to R. H. Pantell.
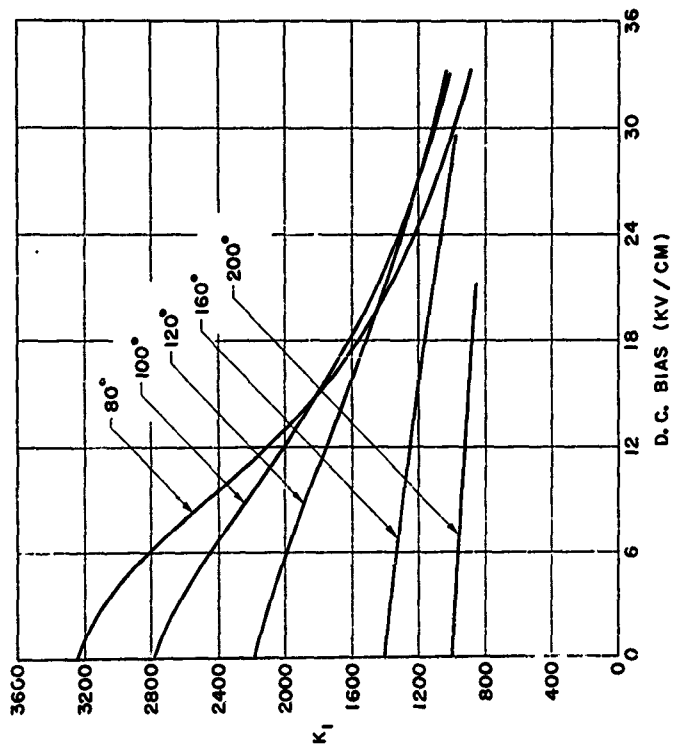
FIG. 15--κ' as a function of dc bias at various temperatures for ceramic of 73% $BaTiO_3$-27% $SrTiO_3$.
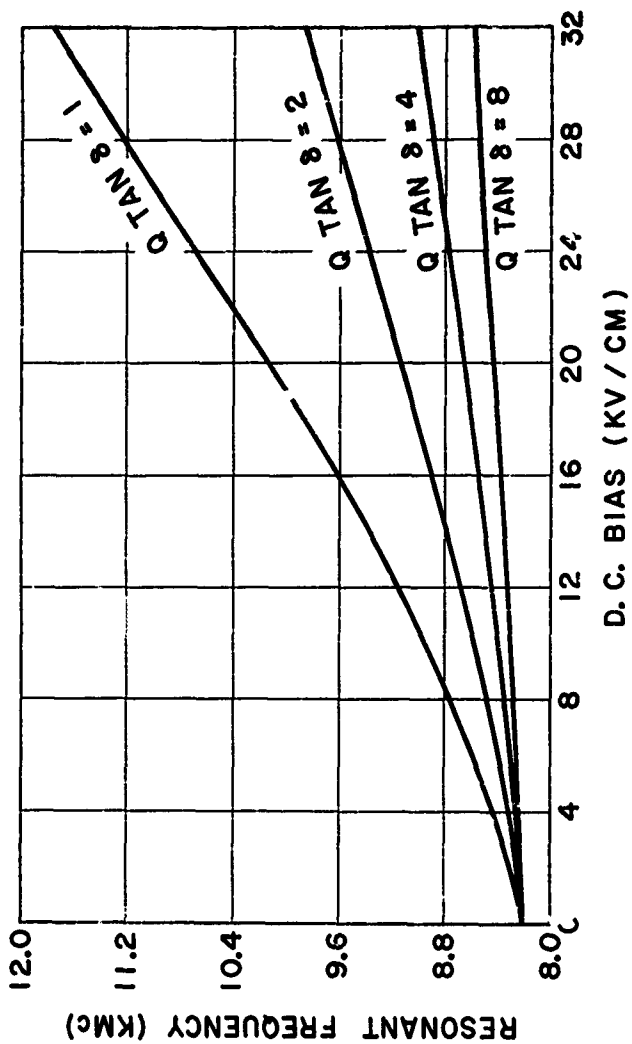
FIG. 16--Expected change in resonant frequency of cavity tuned by a ceramic
of 73% $BaTiO_3$-27% $SrTiO_3$ with dc bias at 120°F.

bias range; but both Q and tan δ will change with the application of
bias. The factor, Q tan δ , will in general increase with increased
bias so that the curves drawn in Fig. 16 will tend to flatten more, than
is shown. Obtaining the exact curves would require solving the boundary
value problem, and this can be quite difficult. For Q tan δ = 4 , the
cavity Q will vary from approximately 45 with no bias to 70 with a bias
of 32 kv/cm while tuning from 8.20 kMc to 8.99 kMc. Although these values
of Q are low for many microwave applications (the Q is about 65 with
a 16 kv/cm bias), such a cavity could be used to tune a reflex klystron by
coupling a cavity filled with dielectric into the re-entrant cavity.

2. Phase Shifter

The formula derived in Appendix C* describes the behavior of a phase
shifter and is presented in Eq. (C.20):

$$\Delta\theta = \frac{1}{2} \frac{P_{lost}}{\tan \delta \, P_{out}} \frac{\Delta\epsilon'}{\epsilon'} ,$$

where ϵ' is the real part of the complex dielectric constant,
$\epsilon = \epsilon' - j\epsilon''$,

$\Delta\epsilon'$ is the incremental change in ϵ' occurring with an
incremental change in bias,

tan δ $= \epsilon''/\epsilon'$ is the loss tangent,

P_{lost} is the power lost in the device,

P_{out} is the power transmitted by the device,

$\Delta\theta$ is the incremental phase shift resulting from the incre-
mental change in dielectric constant, $\Delta\epsilon'$.

It is assumed in the derivation that the insertion loss of the device
is low, that tan δ < 0.1 , that wall losses can be neglected, and that
reflection losses at the input can also be neglected. As with the tuned
cavity, the point of operation should be characterized by a low tan δ
and high nonlinearity. Figure 17 gives the expected phase shift of a
device whose insertion loss, assumed constant, is 2 db when the ceramic
element of 73% $BaTiO_3$-27% $SrTiO_3$ is kept at 120°F. The assumption that
the insertion loss will remain constant is not correct since both κ'

---

*The derivation in Appendix C is accredited to R. H. Pantell.
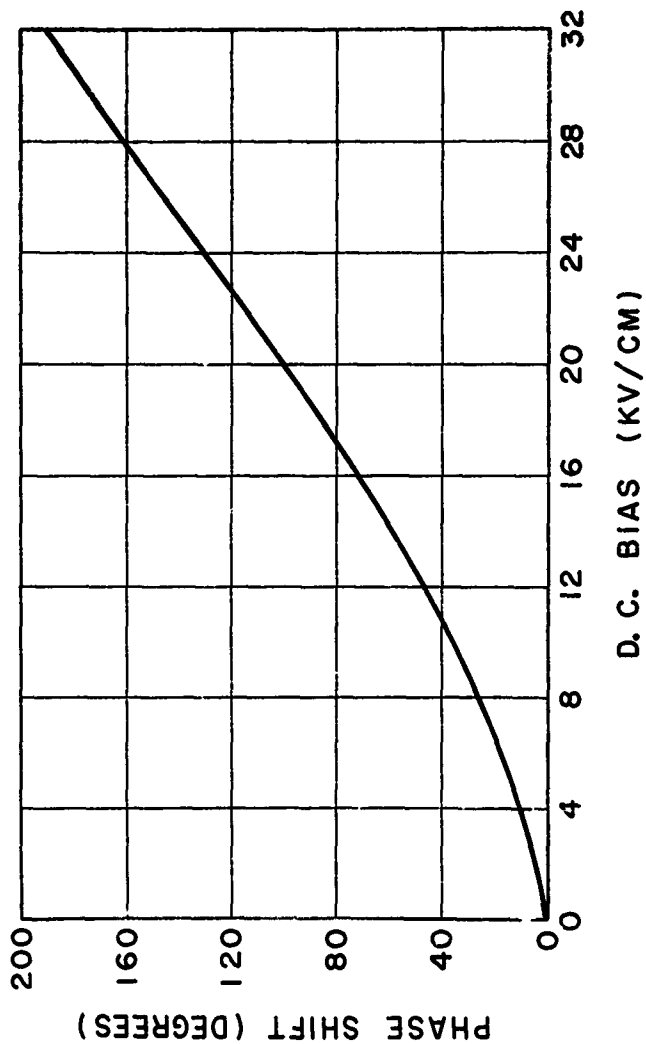
FIG. 17--Expected operation of an electrically biased phase shifter using ceramic of 73% BaTiO$_3$-27% SrTiO$_3$ at 120°F. The designed insertion loss is 2 db.

and tan δ will decrease with bias. The factor

$$\frac{P_{lost}}{P_{out} \tan \delta}$$

will decrease with increased bias; hence the curve shown in Fig. 17 will
flatten with bias. As before, to obtain the exact curve of phase shift,
it would be necessary to solve the boundary value problem for the proposed
geometry. Figure 17 shows that, at most, the total expected phase shift
resulting from the application of a bias field of 32 kv/cm can be expec-
ted to be approximately 190°.

3. Conclusions

    The operating characteristics of an X-band phase shifter and an
electrically tuned cavity ha.. been predicted when a nonlinear ceramic
element of 73% $BaTiO_3$-27% $SrTiO_3$ is employed at $120^{\circ}F$. Neither device
has been built or tested in this part of the study of nonlinear dielec-
trics.

    As yet, most nonlinear dielectrics are quite lossy, and hence the
insertion losses of these devices are high as compared to devices using
other types of elements. For example, Reggia and Spencer[10] have found
that a phase shifter utilizing a ferrite rod in the middle of an X-band
waveguide will give up to 300° phase shift per inch of rod with an inser-
tion loss of only 0.2 db. A fast reflection-type phase shifter employing
a variable capacitance diode has been built and reported by Hardin, Downey,
and Munushian[11] which will give 41° phase shift at 9 kMc, with an inser-
tion loss of 3.9 db. The operating characteristics of this device are
reported to be much better at lower frequencies. A ferroelectric device
might give up to 190° phase shift with an insertion loss of 2 db and can
be expected to have relatively high-power-handling capabilities as well
as to be fast.

    It appears that more work on designing devices employing elements of
nonlinear dielectric is warranted. This is particularly so .. nonlinear
ceramics are developed which have lower losses.

- 33 -

CHAPTER III

SMALL-SIGNAL CHARACTERISTICS AT MILLIMETER WAVELENGTHS

A. INTRODUCTION

Virtually nothing is known of the electrical behavior of ferroelectric titanates at frequencies greater than 25 kMc. Presumably this is because there are very few rf generators available which are capable of producing a range of millimeter waves at power levels sufficient to make such measurements. However, such an rf generator, an electron accelerator with a magnetic undulator, is available at the Microwave Laboratory. This chapter describes how the output of the undulator was used to obtain a curve of the relative dielectric constant of a titanate ceramic with frequency ranging from approximately 60 to 270 kMc. It was believed that this curve might serve two purposes.

First, some physical insight into the mechanism of the nonlinearity might be obtained. An investigation with this objective would probably be more profitable if it were made on a single crystal of the ferroelectric since the structure of such crystals is relatively uncomplicated when compared to that of the corresponding polycrystalline ceramic. However, single crystals were not available and the proposed measurement technique required a three-inch square sample--much greater than the largest titanate crystals. Therefore, a ceramic was used.

Second, the curve would indicate the frequency range over which the nonlinearity could be utilized in the design of microwave devices. This would be particularly so if the curve were established for a ceramic whose small-signal and large-signal properties had already been obtained in the work described in Chapter II and Chapter IV. Therefore, the polycrystalline ceramic 73% $BaTiO_3$-27% $SrTiO_3$ was used, and as described in Chapter IV, the measurements were made at approximately $125^{\circ}F$.

In order to obtain the temperature dependency of the relative dielectric constant at the frequencies above 50 kMc, additional values were taken at lower temperatures. However, even these lower temperatures were above the maximum of the curve of κ' versus temperature (see Fig. 6) corresponding to the Curie temperature of a crystal.

B. INSTRUMENTATION AND MEASUREMENT METHOD

1. Undulator and Interferometer Description

Detailed descriptions of the design and operation of the electron accelerator and magnetic undulator are given by Miller[12] and Szente.[13]

The X-band linear accelerator operates at 9.288 kMc using a 3.5 Mev electron beam. The beam is then introduced into the magnetic undulator which has a transverse dc magnetic-field configuration that is periodic along the electron path. This configuration produces a periodic transverse motion of the beam which results in radiation from the beam. Since the beam initially contains pulsed rf current at the accelerator frequency, the current in the undulator is rich in the harmonics of the fundamental. The undulator spacing and the electron velocity determine the band of harmonics which will be generated. A monochromatic plane wave is then obtained with an echellette grating spectrometer and directed through a modified Fabry-Perot interferometer to measure the relative dielectric constant of the nonlinear ceramic. Figure 18 is a photograph of the instrumentation used in the measurements. The rf wave from the undulator enters from the lower left in Fig. 18, is filtered by the two gratings of the spectrometer, launched through the interferometer shown in the center of the picture, and finally focused on the pickup horn by the parabola shown on the far right and absorbed by the barretter. The dc bias supply for the barretter and the signal pre-amplifier are shown at lower right. The cover which encloses the interferometer and with which the temperature is controlled is shown at the top of Fig. 18. The rf windows in the cover are polystyrene foam, while the heating element inside is a lead-sheathed cable, part of which shows the demountable end.

The interferometer is made up of two 3" $\times$ 3" reflectors, one stationary and one movable, and a lucite coupler placed at 45° to the reflectors and the rf wave as shown in Fig. 19. The movable aluminum reflector is driven by a micrometer drive, and its position measured by the dial indicator to an accuracy of ± 0.0002". The stationary reflector is removable. The relative dielectric constant was measured by looking at the transmission through the interferometer, as a function of the distance between the two reflectors, first with a stationary reflector of aluminum and then with a stationary reflector of the nonlinear ceramic. The temperature of
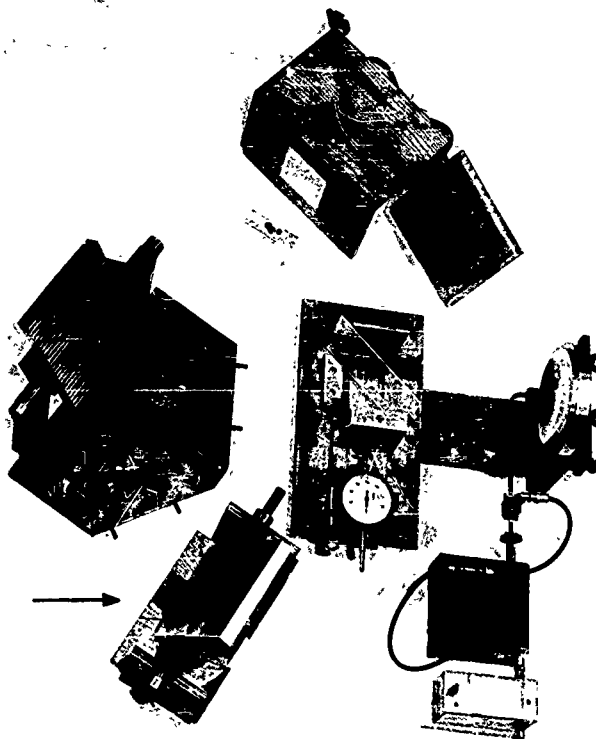
FIG. 18--Photograph of apparatus used to measure the dielectric
constant at millimeter wavelengths.
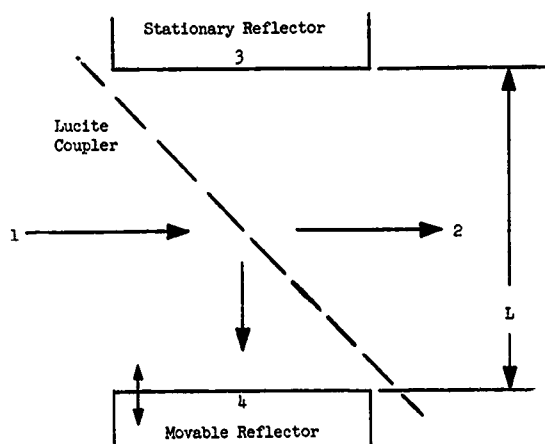
FIG. 19--Schematic diagram of interferometer.

the dielectric was measured by inserting a thermometer through the hole
in the top of the cover into a hole drilled into the aluminum block that
mounts the dielectric reflector. The temperature of the aluminum reflec-
tor shown below the cover in Fig. 18 was monitored in the same way in order
that, when the temperature was maintained at the same level in both measure-
ments, negligible error would be introduced by the thermal expansion or
contraction of the interferometer.

2. Measurement Method

A schematic drawing of the interferometer is shown in Fig. 19. The
monochromatic plane wave enters the interferometer at 1 and leaves at 2.
Part of the wave is reflected by the lucite coupler onto the movable re-
flector at 4, where it is re-reflected through the coupler to the station-
ary reflector at 3. When the spacing, L , between the reflectors is
approximately an integral number of half wavelengths, $m\lambda/2$, the inter-
ferometer is a resonant cavity whose Q is determined by the degree to
which the reflectors are misaligned, reflection losses off the lucite
coupler, power absorption in the air, and power absorbed by the reflec-
tors. The term "approximately" $m\lambda/2$ is used since the reflection co-
efficient of a reflector may not be real, in which case the reflector
will introduce phase shift.

Figure 20 shows the variation of the power received at 2 as a func-
tion of the distance L . Expressions have been derived in Appendix D
giving the index of refraction, n , of the dielectric as a function of
the width and depth of resonance dip in the transmission curve with the
aluminum stationary reflector and the depth of the dip with the dielec-
tric reflector. The derivation is R. M. Miller's. The results of the
derivation are (D.55)

$$n \simeq \frac{1}{\psi_0} \frac{1 - D_1}{D_1 - d_0}$$

where   n is the index of refraction,

the unit subscript indicates that the stationary reflector is
dielectric,

the zero subscript indicates that the stationary reflector is
aluminum,

- 38 -
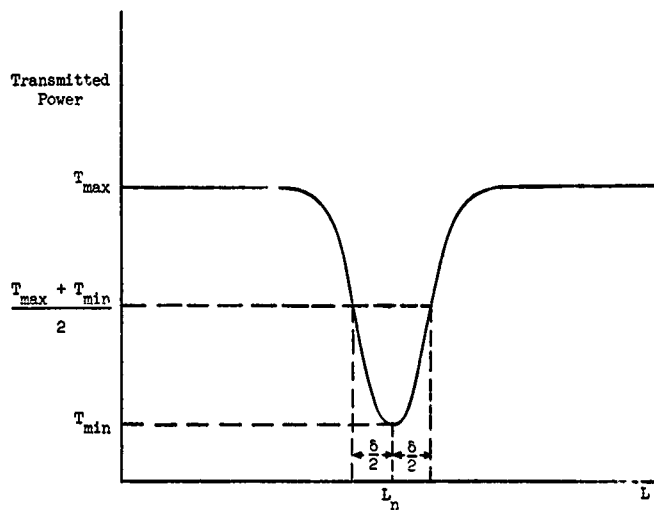
FIG. 20--Power transmitted by interferometer as a function
of the distance, L , between mirrors.

- 39 -

(D.53),

$$\Psi_0 \simeq \sin \frac{\theta_0}{2} \sqrt{1 + \frac{\dot{v}_0^{\,2}(1 - \theta_0 d_0)(1 + d_0^{\,2})}{4}} \,,$$

(D.54),

$$D_1 \simeq d_1\left[1 - \frac{\Psi_0}{2n}(1 - d_0)\right] \,,$$

and (D.9),

$$\theta_0 = \frac{2\pi\delta_0}{\lambda} \,,$$

where $\quad d_1 = \sqrt{T_{min}/T_{max}}\quad$ when the dielectric stationary reflector is used,

$\quad\quad\quad d_0 = \sqrt{T_{min}/T_{max}}\quad$ when the aluminum stationary reflector is used,

$\quad\quad\quad \delta_0 = \quad$ the width of the dip when the transmission is $(T_{max} + T_{min})/2$

$\quad\quad\quad\quad\quad$ and the aluminum stationary reflector is used,

$\quad\quad\quad$ n $\quad$ for Eq. (D.54) is obtained with Eq. (10).

The assumptions made in the derivation are that the reflection coefficient
of the aluminum reflectors is unity, and that the losses suffered by a
wave in a single traverse between the reflectors are the same when L
is set for the minimum of transmission, L_n , and when L is set for the
maximum of transmission. It is also assumed that the index of refraction
of the dielectric reflector is high and that the electrical thickness of
the dielectric is infinite. Any change with frequency in the dielectric
loss of air will not affect the measurements since this attenuation is
taken into account in the derivation given in Appendix D.

The pulse from the pre-amplifier shown in Fig. 18 is placed on the
horizontal axis of an oscilloscope while a sawtooth voltage is placed on
the vertical axis. In this way the full 10 cm on the screen can be util-
ized to read the magnitude of the transmitted signal. The movable reflec-
tor is set with the micrometer drive to give a minimum signal on the scope
face and its position noted. The magnitude of the signal is also read.
The movable reflector is then set to give a maximum of transmission and
the magnitude of the signal again read. If the stationary reflector is
the one of aluminum, d_0 is

$$d_0 = \sqrt{\frac{T_{min}}{T_{max}}} \,. \tag{9}$$

The value of δ_0 can now be obtained directly from the dial indicator readings when the magnitude of the transmitted signal is set at $(T_{max} + T_{min})/2$ as shown in Fig. 20. The term d_1 is obtained in the same way as d_0 except that the dielectric reflector is used. The wavelength is easily determined by reading the distance on the dial indicator between two minima spaced several half-wavelengths apart.

When the stationary reflector is aluminum, the Q of the system is usually high and the dip width in radians, θ_0, small. If, in addition, n is high, Eq. (D.49) reduces to

$$n \simeq \frac{\lambda}{\pi \delta_0} \left(\frac{1 - d_1}{d_1 - d_0} \right) . \tag{10}$$

Before this more appropriate equation is used, however, ψ_0 and D_1 should be evaluated in any given measurement to test its validity.

According to von Hippel,[14] the relation between the index of refraction and the dielectric constant is given for a lossy medium by

$$n = \left\{ \frac{1}{2} \kappa' \left[\sqrt{1 + \tan^2 \delta} + 1 \right] \right\}^{1/2} . \tag{11}$$

Even if $\tan \delta = 0.5$, Eq. (11) reduces to

$$\kappa' \simeq n^2 , \tag{12}$$

with an error in the real part of the relative dielectric constant, κ', of less than 6%.

An expression for the loss tangent, $\tan \delta$, is derived in Appendix D and is (D.63):

$$\tan \delta \simeq 2n \left(\frac{2\pi \Delta L}{\lambda} \right) ,$$

where ΔL is the distance between the minimum position with the aluminum stationary reflector and that with the dielectric stationary reflector.

C. RESULTS

At first, attempts were made to obtain κ' as a continuous function of temperature at a given frequency by heating the interferometer to approximately $125^\circ F$ and then allowing it to drift slowly toward room temperature. Two thermal drifts were required at each frequency: one with the dielectric reflector, and one with the aluminum reflector. The

accelerator and undulator required the frequent tuning of many inter-
dependent adjustments in order to have suitable signal stability and to
keep the output level high enough for accurate readings. But approxi-
mately 5 hours of measurement were needed for each curve of κ' . Usually
the results of these measurement runs would have to be discarded because
the curves of d_1 and d_0 were not smooth and continuous. In a few
cases discontinuous jumps occurred in the curves. Although the cause of
the anomalies was never satisfactorily determined, presumably the diffi-
culty stemmed from the need to tune the machine frequently--perhaps a
change in the power level of the harmonics adjacent to the one being used.
It was felt that the difficulty did not originate in the interferometer.
In spite of this anomalous behavior, two continuous curves of κ' were
obtained: one at 55.8 kMc and one at 148.5 kMc. Although these curves
would accurately display the temperature dependency of κ' , the magnitude
of κ' at 55.8 kMc did not reproduce when later checked by constant
temperature measurements.

Because of the difficulty experienced with continuous runs, it was
decided that single values of κ' should be quickly obtained with the
temperature of the interferometer stabilized, and that two groups of
values should be determined at widely separated temperatures to show the
temperature dependency of κ' . In addition, a second grating was added
to the spectrometer to further suppress adjacent harmonics. The machine
was not tuned during a measurement run. In a given run, 10 values each
of d_0 , δ_0 , and d_1 were obtained at the stable temperature and were
averaged to compute one value of κ' . This process was then immediately
repeated to obtain a second value, and so on.

As can be seen from Eq. (D.49) or Eq. (10), a small difference between
two relatively large numbers, i.e. $(d_1 - d_0)$, must be taken and squared
to obtain κ' . It was found that the greatest error was introduced by
this factor which was critically dependent on the manner in which the
stationary reflector was secured. This experimental error was much greater
than that calculated from the scatter of the individual data points and
that arising out of the assumptions made in the derivation. It is esti-
mated that when the greatest possible care is exercised in the placement
of the stationary reflector, the values of n are accurate within ±5%;
hence the values of κ' are accurate within ±10%.

The results of the measurements of κ' are shown in Fig. 21. The points at 8 and 10 kMc were obtained in the measurements reported in Chapter II and the point at 2.72 kMc was obtained from the measurements reported in Chapter IV.

Figure 22 shows the percent change in κ' with a temperature change from $123^{\circ}F$ to $95^{\circ}F$. The points at 55.8 and 148.5 kMc were taken from the continuous curves described in the first part of this section. However, the points at 102.1 and 269 kMc were obtained from data taken at $123^{\circ}F$ and $83^{\circ}F$. For the point shown at 102.1 kMc, the greater temperature interval resulted in the κ' taken at $83^{\circ}F$ falling outside the ±10% error in the value of κ' at $123^{\circ}F$. The percent change was then scaled to the temperature interval used in Fig. 22. For the point shown at 269 kMc, the use of the greater temperature interval indicated that the percent change was less than 7% over the smaller temperature interval of Fig. 22.

Unless the loss tangent were very large (i.e., on the order of unity), it can be shown that there is little chance of obtaining its value with this measurement technique. Equation (D.57) can be used with Fig. 21 to estimate the distance ΔL that must be measured to obtain $\tan \delta$. By rearranging Eq. (D.57), this distance is given by

$$\Delta L \simeq \frac{\lambda \tan \delta}{4\pi n} . \qquad (13)$$

If it is assumed that $\tan \delta = 0.5$ and that the frequency is 55.8 kMc (the largest value of λ/n occurs here), then Eq. (13) yields

$$\Delta L \approx 0.0002" , \qquad (14)$$

but this is within the experimental error of ±0.0002" experienced in determining the distance, L, between the two reflectors. At no time did the data indicate a loss tangent as large as unity.

The curve of Fig. 21 shows κ' falling rapidly as the frequency of the applied field increases above 50 kMc; and it therefore indicates that the mechanism giving rise to the high dielectric constant above the Curie temperature at lower frequencies undergoes a relaxation in the frequency interval from 50 to 100 kMc. The decrease in κ' shown in Fig. 21 could possibly be due to an electrical resonance within the individual crystallites of the ceramic. A piece of the ceramic was crushed and viewed with a microscope at 100x magnification. The largest dimension of all the

- 43 -
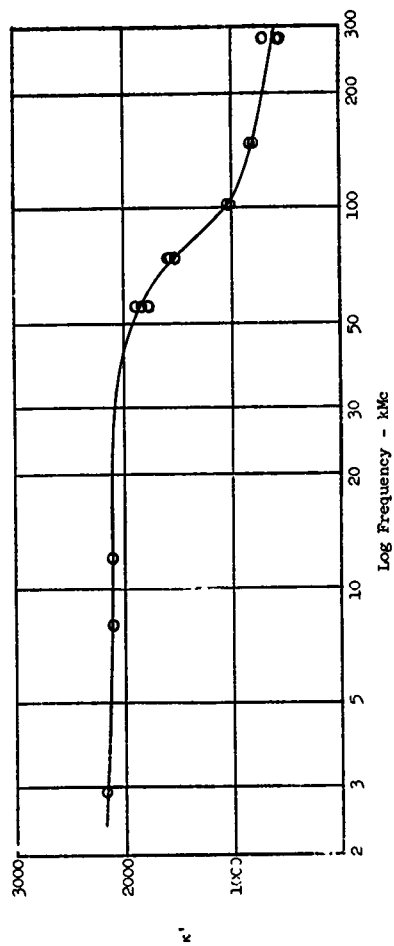
FIG 21--κ' as a function of frequency for ceramic of 73% BaTiO$_3$ - 27% SrTiO$_3$ at 123°F.
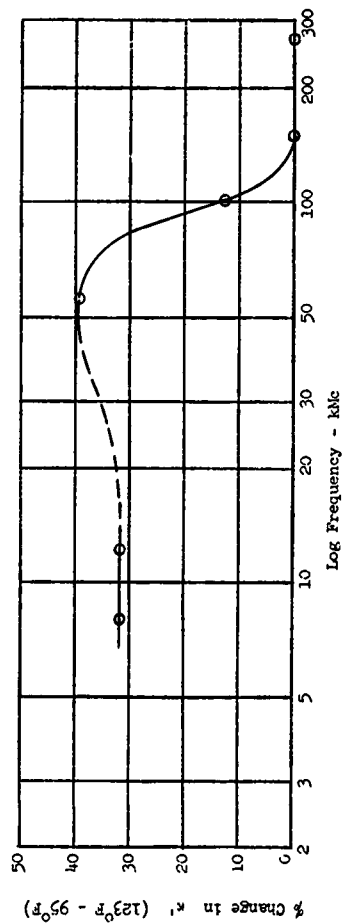
FIG. 22--Per cent change in κ' between T = 123°F
and T = 95°F as a function of frequency.

Log Frequency - kMc

% Change in κ' (123°F - 95°F)

50   40   30   20   10   0

2   3   5   10   20   30   50   100   200   300

crystallites observed was less than 0.0005" and the distance between the
crystallites appeared to be immeasurably small at this magnification.
The lowest frequency at which a crystallite could resonate electrically
would be that at which its major dimension was a half wavelength; hence,
the resonance frequency would be

$$f = \frac{c}{\lambda_0} = \frac{c}{2d\sqrt{\kappa'}} , \qquad (15)$$

where   c = velocity of light in air,

         λ_0 = freespace wavelength,

         d = major dimension of the crystallite,

         κ' = real part of the complex relative dielectric constant.
If a crystallite had a major dimension of 0.0005" and if its relative
dielectric constant were 10^4, then from Eq. (15) its resonant frequency
could be no lower than f = 118 kMc ; hence, the indication is that the
observed decrease in κ' cannot be attributed to electrical resonances
in the crystallites. This indication is further strengthened by the
curve of Fig. 22 which shows that the variation of κ' with temperature
disappears at 150 kMc. As previously mentioned, the temperature interval
used for Fig. 22 is that from 123°F to 95°F; however, the point at 269 kMc
was taken with an even larger temperature range to intensify any variation
of κ' with temperature that might be present. No such variation was
found; hence, it is probable that a Curie temperature cannot be seen
above 200 kMc.

Figures 21 and 22 do indicate, however, that the nonlinear proper-
ties of the measured ceramic can probably be utilized in device work at
frequencies up to 50 kMc. The change in dielectric constant in the
frequency interval from 50 to 100 kMc could be utilized for filter design.

CHAPTER IV

LARGE-SIGNAL MICROWAVE CHARACTERISTICS

A. INTRODUCTION

The design of large-signal microwave devices employing nonlinear
dielectric elements requires expressions that will describe the macro-
scopic electrical behavior of the dielectric when subjected to high-rf-
field intensities. To obtain these expressions a new method has been
evolved to measure the large-signal electrical characteristics of a non-
linear dielectric ceramic. The derivation and use of this technique is
described in this chapter.

The measurements must necessarily be made with some sort of microwave
circuit that uses distributed lements; however, a nonlinear mathematical
analysis is much more easily performed on a circuit containing lumped
elements. For this reason, it was decided that the microwave circuit
should be that of a coaxial re-entrant cavity in which the nonlinear
dielectric is placed in the region of high-electric-field intensity. This
type of cavity can be easily and accurately represented by an equivalent
circuit whose behavior can then be investigated by lumped-element non-
linear analysis.

If the magnitude of the electric-flux density vector, $\vec{D}$, in the
dielectric element were plotted as a function of the magnitude of the
electric-field intensity vector, $\vec{E}$, the slope would decrease with in-
creasing field intensity. That is, what was the real part of a complex
dielectric constant, ϵ' , in the linear small-signal analysis is now a
function of the applied electric field, or

$$\vec{D} = \epsilon'(E)\vec{E} .$$ (16)

The value of $\epsilon'(E)$ depends upon the magnitude, and not the direction,
of the electric field, since the ceramics, unlike the single cryst ls,
are isotropic. In this analysis, $\epsilon'(E)$ is expanded as a power series
in E which is then used to describe the variation of the capacitance
of the element in the cavity and the corresponding nonlinear capacitor
in the lumped equivalent circuit. In like manner, a power-series expan-
sion is made for the dielectric conductivity of the ceramic, $\sigma(E)$, and
used in the expression for the nonlinear conductance in the equivalent
circuit.

- 47 -

A condition on the solution of the differential equation of the equivalent circuit is obtained which could yield curves of the magnitude of the fundamental frequency response of the cavity as a function of the drive frequency at a constant-incident power level. But since it is the determination of the coefficients in the power-series expansions that is of interest, curves of the response of the cavity to a known level of incident power are experimentally obtained as a function of frequency and used with the condition on the differential equation to determine the desired coefficients. In this way the electrical behavior of the nonlinear ceramics is measured and the expressions necessary for the design of large-signal devices are obtained.

B. CAVITY GEOMETRY AND EQUIVALENT CIRCUIT

A cross section of the coaxial cavity is shown in Fig. 23. The nonlinear dielectric element is a right-circular cylinder of ceramic having length, ℓ , and radius, a . This dielectric post is located in the region of maximum electric field between the end of the center conductor of the coaxial transmission line and the upper shorting plane in Fig. 23. The transmission line below plane k-k is much less than a quarter wavelength long, and can, therefore, be considered an inductance at plane k-k whose value is independent of field strength and which
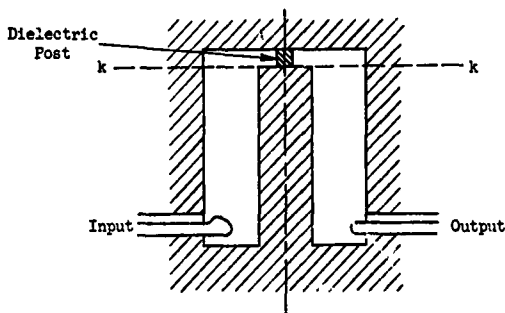
FIG. 23--Schematic cross section of coaxial cavity.

- 48 -

resonates with the nonlinear capacitance above plane k-k . The losses
in the cavity can be represented by two conductances located at plane
k-k : a linear one representing the wall losses in the cavity and a non-
linear one representing the losses in the dielectric. Power is introduced
into the cavity through a coupling loop located in the region of maximum
magnetic field. The response of the cavity is sampled with another loop
placed opposite the input loop.

The lumped element equivalent circuit is shown in Fig. 24.
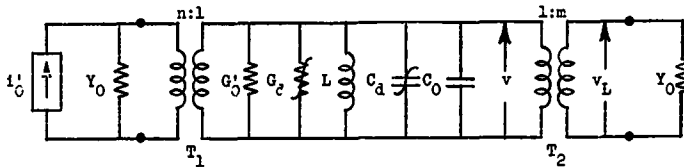
FIG. 24--Equivalent circuit of coaxial cavity.

For Fig. 24,

i_0' is a constant current generator corresponding, as shown
later, to constant power incident on the cavity,

Y_0 is the internal admittance of the generator i_0' and the
load admittance at the output of the cavity,

T_1 and T_2 are ideal transformers representing the input and
output coupling loops; T_1 has a turns ratio n:1 and
T_2 has a turns ratio 1:m,

G_0' represents the wall losses in the cavity,

C_0 represents the capacitance between the end of the center
conductor and the upper shorting plane but does not include
that of the dielectric,

G_d represents the nonlinear loss in the dielectric element,

C_d represents the nonlinear capacitance of the dielectric
element,

- 49 -

L   is the inductance of the shorted transmission line when
     viewed from plane k-k ,

v   is the voltage across the nonlinear dielectric element,

v_L is the voltage across the output load, Y_0 .

The validity of the equivalent circuit shown in Fig. 24 rests upon the
extent to which the elements vary with frequency. Since the length of
the transmission line below plane k-k is much less than a quarter wave-
length, its reactance is inductive over the entire frequency range of the
measurements. The capacitance, C_0 , of the geometry at the end of the
center conductor without the dielectric post will be calculated with a
formula whose validity over the frequency range of interest has been
checked and verified. The conductance, G_0 , will be neglected since
the wall losses in the cavity are much less than the losses in the di-
electric. Since all the dimensions of the dielectric post are much less
than a wavelength, the loss and capacitance of the post can be accurately
represented by G_d and C_d over the entire frequency range used. It is
felt that the major source of error rises out of the uncertainty involved
in calculating the inductive reactance of the transmission line; that is,
should L be calculated at the plane k-k or the shorting plane above
k-k , or somewhere between the two? However, the distance between the
two planes is less than one-tenth the length of the transmission line;
hence the error introduced is probably negligible.

The circuit of Fig. 24 can be reduced to that of Fig. 25.
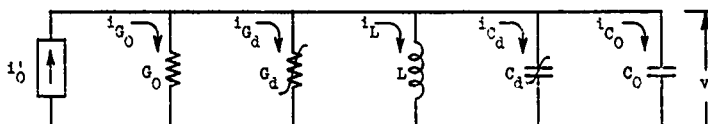
FIG. 25--Equivalent circuit of the coaxial cavity with the
generator and load reflected into the cavity.

For Fig. 25,

G_d , L , C_2 . C_0 , and v are as previously defined,

$i_0 = ni_0'$,

$G_0 = G_0' + n^2 Y_0 + m^2 Y_0$.

The nonlinear conductance, G_d , in the equivalent circuit repre-
sents the rf conductance of the nonlinear dielectric post and is a func-
tion of the voltage, v , across the post. Let G_d be defined by

$$G_d = G_d(v) = \frac{\sigma(v)A}{\ell} \triangleq \sum_{n \text{ even}} a_n v^n , \qquad (17)$$

where $\sigma(v)$ is the rf dielectric conductivity of the ceramic,

A   is the cross sectional area of the post = πa^2 , when

a is the radius,

ℓ is the length of the post.

The summation is over the even values of n since the conductivity of
the dielectric is independent of the direction of the electric field
intensity vector in the ceramic.

The capacitance, C_d , in the equivalent circuit represents the
capacitance of the dielectric post in the cavity and, like the conductance,
G_d , can be expressed as a power series in v . If $q_d(v)$ is the charge
bound at one end of the dielectric post by the polarization within the
dielectric and $\epsilon'(v)$ is as defined for Eq. (16) when $v = E\ell$, then
Eq. (16) can be rewritten as

$$D = \frac{q_d(v)}{A} = \epsilon'(v) \frac{v}{\ell} . \qquad (18)$$

With the use of Eq. (16), $q_d(v)$ can be defined as a power series in v :

$$q_d(v) = \epsilon'(v) \frac{A}{\ell} v = \sum_{m \text{ even}} b_m v^{m+1} = C_d(v)v . \qquad (19)$$

Here, too, the summation is over even integers since the value of $\epsilon'(v)$
is independent of the direction of the electric field intensity vector.

The problem can now be simply stated as that of determining a_n
and b_m .

- 51 -

C. SOLUTION OF DIFFERENTIAL EQUATION

The input current, i_0 , in Fig. 25 is the sum of the currents in the individual elements, i.e.,

$$i_0 = i_{G,0} + i_{G,d} + i_L + i_{C,d} + i_{C,0} . \tag{20}$$

Equation (20) can be put in the differential form

$$i_0 = \frac{d}{dt} C_0 v + \frac{d}{dt} q_d(v) + G_0 v + G_d(v)v + \frac{1}{L} \int v dt . \tag{21}$$

Since the dc terms are not of interest, Eq. (21) can be differentiated with respect to time. Upon performing the differentiation, using Eqs. (17) and (19), and terminating the series when $n = m = 4$, Eq. (21) becomes

$$\frac{di_0}{dt} = \left[(b_0 + C_0) + 3b_2 v^2 + 5b_4 v^4 \right] \frac{d^2 v}{dt^2} + (6b_2 v + 20b_4 v^3)\left(\frac{dv}{dt} \right)^2$$

$$+ \left[(a_0 + G_0) + 3a_2 v^2 + 5a_4 v^4 \right] \frac{dv}{dt} + \frac{1}{L} v . \tag{22}$$

Equation (22) is the desired basic differential equation that describes the behavior of resonant cavity.

Several methods are available for investigating Eq. (22).[15,16,17] The method used in this analysis is an iterative procedure similar to Duffing's method, which is due to Stoker.[17] It is reasonable to make the a-priori assumption that the nonlinearity is small, i.e., $b_0 \gg b_2 \gg b_4$, and $a_0 \gg a_2 \gg a_4$; hence the fundamental component of the response will be much larger than the harmonic components. A periodic solution is sought. Let the known driving function be

$$i_0 = A \cos \omega t + B \sin \omega t . \tag{23}$$

The phase angle is included in the driving function for convenience. As a first approximation, let the circuit response be that of the free linear oscillation

$$v \simeq v_0 = A_0 \cos \omega t . \tag{24}$$

After first dividing both sides by $(b_0 + C_0)$, adding $\omega^2 v$ to both sides,

- 52 -

using Eq. (23), and then rearranging, Eq. (22) becomes

$$\ddot{v} + \omega^2 v = - \frac{A\omega}{(b_0 + C_0)} \sin \omega t + \frac{B\omega}{(b_0 + C_0)} \cos \omega t + \left[\omega^2 - \frac{1}{L(b_0 + C_0)} \right] v$$

$$- \left[\frac{3b_2}{(b_0 + C_0)} v^2 + \frac{5b_4}{(b_0 + C_0)} v^4 \right] \ddot{v} - \left[\frac{6b_2}{(b_0 + C_0)} v + \frac{20b_4}{(b_0 + C_0)} v^3 \right] \dot{v}^2$$

$$- \left[\frac{(a_0 + G_0)}{(b_0 + C_0)} + \frac{3a_2}{(b_0 + C_0)} v^2 + \frac{5a_4}{(b_0 + C_0)} v^4 \right] \dot{v} , \qquad (25)$$

where $\dot{v} = dv/dt$ and $\ddot{v} = d^2v/dt^2$. Equation (24), the first approximation to the response of the circuit, is now substituted into Eq. (25). After considerable use of trigonometric formulas, Eq. (25) reduces to

$$\ddot{v} + \omega^2 v = M_1 \cos \omega t + N_1 \sin \omega t + M_3 \cos 3\omega t$$

$$+ N_3 \sin 3\omega t + M_5 \cos 5\omega t + N_5 \sin 5\omega t , \qquad (26)$$

where

$$M_1 = \frac{B\omega}{(b_0 + C_0)} + \left[\omega^2 - \frac{1}{L(b_0 + C_0)} \right] A_0 + \frac{3}{4} \frac{b_2 \omega^2}{(b_0 + C_0)} A_0^3 + \frac{5}{8} \frac{b_4 \omega^2}{(b_0 + C_0)} A_0^5 ,$$

$$N_1 = - \frac{A\omega}{(b_0 + C_0)} + \frac{(a_0 + G_0)\omega}{(b_0 + C_0)} A_0 + \frac{3}{4} \frac{a_2 \omega}{(b_0 + C_0)} A_0^3 + \frac{5}{8} \frac{a_4 \omega}{(b_0 + C_0)} A_0^5 ,$$

$$M_3 = \frac{9}{4} \frac{b_2 \omega^2}{(b_0 + C_0)} A_0^3 + \frac{45}{16} \frac{b_4 \omega^2}{(b_0 + C_0)} A_0^5 ,$$

$$N_3 = \frac{3}{4} \frac{a_2 \omega}{(b_0 + C_0)} A_0^3 + \frac{15}{16} \frac{a_4 \omega}{(b_0 + C_0)} A_0^5 ,$$

$$M_5 = \frac{25}{16} \frac{b_4 \omega^2}{(b_0 + C_0)} A_0^5 ,$$

$$N_5 = \frac{5}{16} \frac{a_4 \omega}{(b_0 + C_0)} A_0^5 .$$

- 53 -

Now unless $M_1 = N_1 = 0$, the solution will involve $t \cos \omega t$ and $t \sin \omega t$. But this means that the response of the circuit would not be periodic in violation of the basic assumption made above. Setting $M_1 = N_1 = 0$ in Eq. (26), gives the following values for A and B:

$$A = (a_0 + G_0)A_0 + \frac{3}{4} a_2 A_0^3 + \frac{5}{8} a_4 A_0^5 , \tag{27}$$

$$B = -\left[\omega(b_0 + C_0) - \frac{1}{\omega L}\right] A_0 - \frac{3}{4} b_2 \omega A_0^3 - \frac{5}{8} b_4 \omega^2 A_0^5 , \tag{28}$$

and reduces the differential equation to

$$\ddot{v} + \omega^2 v = M_3 \cos 3\omega t + N_3 \sin 3\omega t + M_5 \cos 5\omega t + N_5 \sin 5\omega t . \tag{29}$$

The solution of Eq. (29) is

$$v_1 = M_1' \cos \omega t + N_1' \sin \omega t - \frac{M_3}{8\omega^2} \cos 3\omega t$$

$$- \frac{N_3}{8\omega^2} \sin 3\omega t - \frac{M_5}{24\omega^2} \cos 5\omega t - \frac{N_5}{24\omega^2} \sin 5\omega t , \tag{30}$$

where M_1' and N_1' are fixed by the homogeneous equation. Following Stoker's technique,[17] choose $M_1' = A_0$ and $N_1' = 0$. This can be done since the phase of the drive, i_0 , is adjustable; hence,

$$v_1 = A_0 \cos \omega t - \frac{M_3}{8\omega^2} \cos 3\omega t - \frac{N_3}{8\omega^2} \sin 3\omega t - \frac{M_5}{24\omega^2} \cos 5\omega t - \frac{N_5}{24\omega^2} \sin 5\omega t . \tag{31}$$

Equation (31) is a first approximate solution to the differential equation. It can be used in the same way as the first approximation to v , Eq. (24), to obtain a second approximate solution to the differential equation. This iteration process could be continued until a solution of the desired accuracy were obtained. However, it is not a solution of the differential equation that is sought in this analysis but the condition given by Eqs. (27) and (28). Equation (23) can be rewritten as

$$i_0 = P \cos(\omega t + \phi) = A \cos \omega t + B \sin \omega t . \tag{32}$$

Hence, the magnitude of the drive is

$$P = (A^2 + B^2)^{1/2} . \tag{33}$$

Substituting Eqs. (27) and (28) into Eq. (33) gives the result

$$P^2 = \left\{ (a_0 + G_0)A_0 + \frac{3}{4} a_2 A_0^3 + \frac{5}{8} a_4 A_0^5 \right\}^2$$
$$+ \left\{ \left[\omega(b_0 + C_0) - \frac{1}{\omega L} \right] A_0 + \frac{3}{4} b_2 \omega A_0^3 + \frac{5}{8} b_4 \omega A_0^5 \right\}^2 . \quad (34)$$

Experimental values of A_0 at high known drive levels and various values of ω can be used in Eq. (34) to determine a_2, a_4, b_2, and b_4. The values of a_0, b_0, and G_0 can best be obtained with small-signal measurements of the cavity response, and that of C_0 can be calculated.

D. DESIGN AND FABRICATION OF CAVITY, CAVITY HOLDER, AND CERAMIC SAMPLE

1. Cavity Design

Since a relatively large supply of 73% $BaTiO_3$-27% $SrTiO_3$ ceramic had been obtained and could therefore be used in other phases of the study of nonlinear dielectrics for device work and since it showed considerable nonlinearity under the influence of a dc bias field, it was decided that this material should be used for the large-signal measurements. However, because the real part of the small-signal relative dielectric constant, κ', was so large, the measurements were made in the S-band frequency range so that the physical dimensions of the cavity would not be prohibitively small. The only data available for this particular batch of material was that obtained in the small-signal X-band measurements described in Chapter II. The cavity was therefore designed with the X-band data to resonate at 3.00 kMc. Even with a relatively large change of κ' between the S-band and X-band, the cavity should still resonate in the S-band frequency range. In order that a positive control of the temperature could be maintained and that the losses should be relatively low, the operating temperature was chosen as 125°F. At this temperature, the X-band value of κ' is 2000.

The design procedure was first to choose the size of the dielectric post and calculate its small-signal capacitance. The capacitance, C_0, was calculated and added to that of the dielectric. The input reactance of the shorted transmission line was then set equal to the reactance of the total capacitance, thereby determining the length of the line. The characteristic impedance of the line was chosen as 75Ω, a value which gave rise to a reasonably small C_0 and still made it possible to machine the cavity.

- 55 -

The high κ' of the ceramic made it mandatory that the post be small. A length of 0.020" and a diameter of 0.010" were chosen for the cylinder. The small-signal capacitance of this post is

$$C_d' = \frac{\epsilon_0 \kappa' A}{\ell} = 1.76 \ \mu\mu f , \qquad (35)$$

where ϵ_0 is the dielectric constant of free space,

   A is the area of one end of the post $= \pi a^2$,

   ℓ is the length of the post.

The capacitance, C_0 , can be obtained from a formula given by Marcuvitz[18] for calculating the susceptance of the capacitive gap terminating a coaxial line as shown in Fig 26.
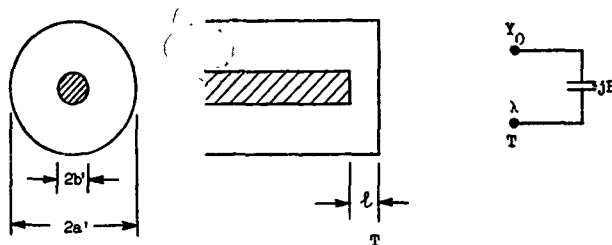
FIG. 26--Geometry and equivalent susceptance of capacitive gap terminating a coaxial line (after Marcuvitz[18]).

At the reference plane, T , in Fig. 26, the susceptance is given by

$$\frac{B}{Y_0} = \frac{4b'}{\lambda} \ln \frac{a'}{b'} \left[\frac{\pi}{4} \frac{b'}{\ell} + \ln \frac{(a' - b')}{\ell} \right] , \qquad (36)$$

where λ is, in this case, the freespace wavelength at the resonant frequency, $f_0 = 3.00$ kMc.

The diameter of the center conductor, 2b' , was arbitrarily chosen to

be 0.125". The ratio a'/b' can be obtained from the characteristic impedance of the line,

$$Z_0 = 60 \ln\left(\frac{a'}{b'}\right) . \tag{37}$$

With a Z_0 of 75Ω, Eq. (37) yields $(a'/b') = 3.49$; hence, $2b' = 0.436"$. As stated previously, $\ell = 0.020"$. With these values, Eq. (36) yields

$$\frac{B}{Y_0} = 0.175 ; \tag{38}$$

hence

$$C_0 = \frac{B}{2\pi f_0} = \frac{0.175 Y_0}{2\pi f_0} = 0.124 \ \mu\mu f . \tag{39}$$

As desired, $C_0 \ll C_d'$. Since $\ell \simeq \lambda/200$, the reference plane T can be used in place of plane k-k, shown in Fig. 23, in this approximate derivation. At the reference plane, T, the total small-signal capacitive reactance is

$$X_c = \frac{1}{2\pi f_0(C_0 + C_d')} = 28.2\Omega . \tag{40}$$

If $f = f_0$, X_c equals X_L where X_L is the input reactance of the shorted transmission line and is given by

$$X_L = Z_0 \tan \beta \ell' , \tag{41}$$

where $\beta = 2\pi/\lambda$ is the propagation constant in the line, and
         ℓ' is the length of the line.
Upon substituting the result of Eq. (40) into Eq. (41) and solving for ℓ', the result is

$$\ell' = 0.226" \simeq \frac{\lambda}{17} .$$

In summary, the electrically important dimensions derived in this section are shown in the top view and cross section of Fig. 27.

2. Cavity and Cavity-Holder Description

The dielectric post is bathed in a moving stream of sulfur hexafluoride gas, SF_6. This is introduced into the cavity through the four 0.013" holes, shown in Fig. 27a, which have been drilled in the end of the
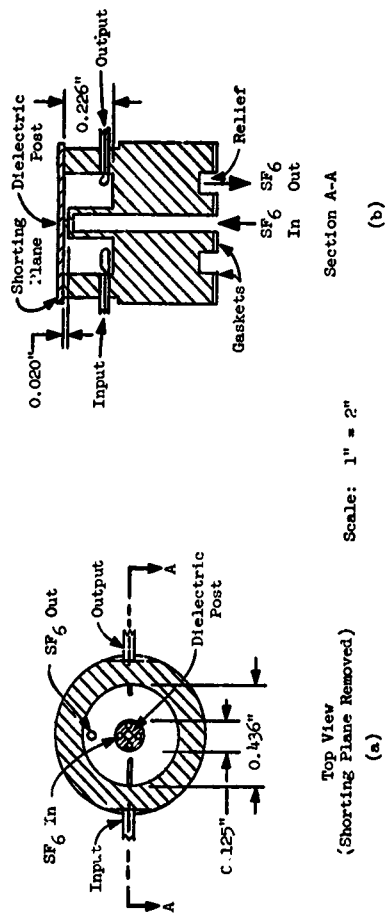
FIG. 27.—Top view and cross section of coaxial cavity.

(a) Top View (Shorting Plane Removed)

(b) Section A-A

Scale: 1" = 2"

- 58 -

center conductor at such an angle that the gas streams move along lines tangent to the post. In this way a circular flow is set up around the post to carry away the heat generated in the dielectric by rf dissipation. The SF_6 also serves to prevent rf breakdown. The gas is brought to these four outlets by a hole drilled from the lower end to meet them as shown in Fig. 27b. The gas outlet hole, shown in Fig. 27a, has been drilled through the bottom of the cavity to the relief, shown in Fig. 27b, cut in the lower end. The outlet was made large enough to insure that the pressure in the cavity would be no greater than one atmosphere. The shorting plane is a thin silver-plated beryllium copper disk. The input and output couplers were made from 0.089" o.d. 50Ω coaxial line. The inside surfaces of the cavity were silver plated. Figure 28 is a photograph of the cavity with the dielectric post.

The cavity holder is primarily a heat reservoir whose temperature can be closely controlled. A photograph of the holder is shown in Fig. 29. It was made from a four-inch diameter brass cylinder which was bored to receive the cavity. The temperature was controlled by mounting a thermo-switch in the brass that was in series with a Variac and the lead-covered heating cable wrapped around the outside of the holder. A thermometer was also inserted into the holder to monitor the temperature. The holder was wrapped in asbestos tape and then enclosed by an asbestos box which was, in turn, covered with aluminum foil. In this way it was possible to keep the thermal drift of the cavity holder to less than $\pm 0.5^\circ F$.

The sulfur hexafluoride gas was fed to the cavity by means of a hole drilled up through the center of the holder to meet that drilled in the cavity. Likewise, the gas exhausted from the relief cut in the bottom of the cavity through a second hole in the holder to a tube which vented to the fume hood. When introduced through the long hole drilled in the holder, the gas was preheated to the cavity temperature.

Figure 30 is an exploded-view photograph of the parts as they go into the cavity holder. In order to show how the parts fit into the holder, a detailed description of their assembly is given in Appendix 8.

3. Sample Fabrication

The first step in fabricating the cylindrical post of the nonlinear dielectric was to cut and grind a slab of the ceramic to a 0.020" thickness. After the slab had been cleaned, a film of metallic silver was
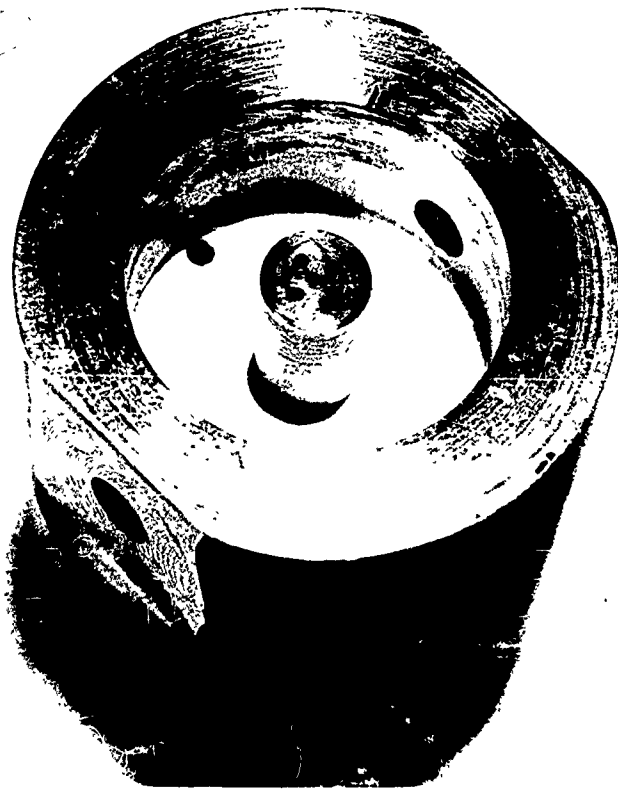
FIG. 28--Microphotograph of coaxial cavity with shorting plane removed. The dielectric post is seen on the end of the center conductor.
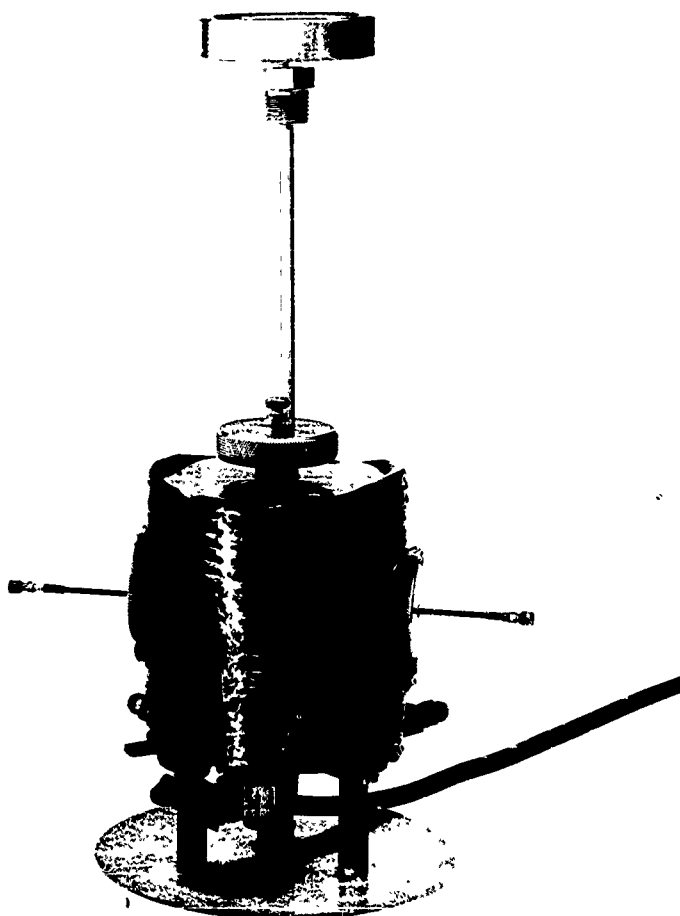
FIG. 20--Photograph of assembled cavity holder.
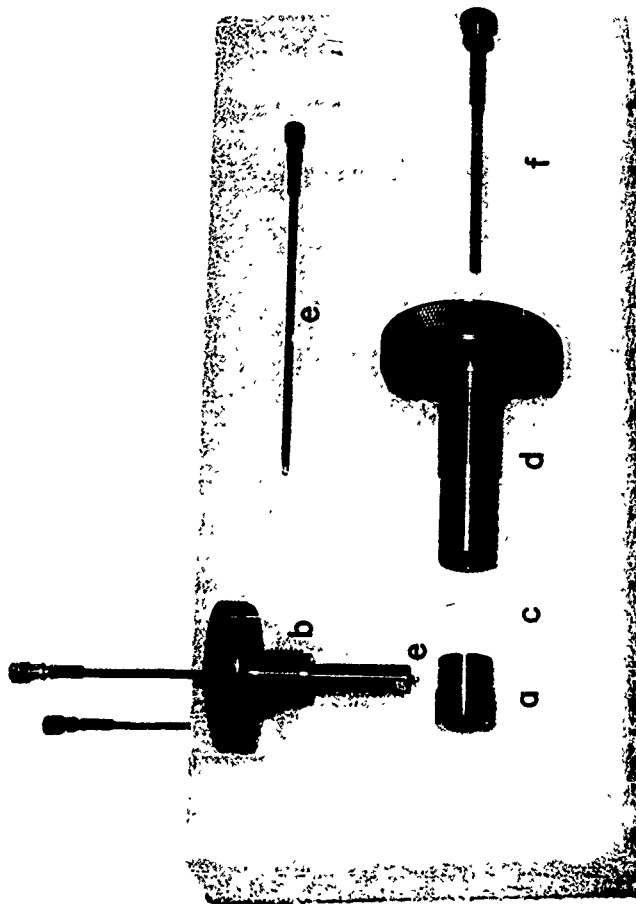
FIG. 30--Exploded-view photograph of cavity and cavity holder parts.

chemically deposited on it by the same process used in silvering mirrors.
Just enough copper was then electroformed onto the slab to protect the
silver and stop its oxidation (approximately 0.0002"). In this way it
was possible to coat the ceramic with a conducting film which would not
peel off with subsequent grinding. Other methods of deposition were
tried, including the evaporation of silver onto the ceramic; however, with
this latter method the bond of the metal to the ceramic was poor, with
the result that the film later peeled. The processes involving the firing
of paints were not tried since it was felt that the firing might alter the
structure of the ceramic by allowing grain growth, in which case the meas-
ured sample would not characterize the lot from which it was cut.

Cylindrical blanks were then cut from the slab with an ultrasonic
impact grinder using boron carbide #800 grinding dust. The cutting tool
was a 1/4" length of 0.020" o.d.-0.002" o.d. w.th. nickel cathode sleeve
which was driven through the slab at right angles to its surface. The
blank was that portion of the slab left uncut in the hole of the tubing.
Figure 31 is a microphotograph taken from above the slab of dielectric
after two holes had been cut. The hole on the left was not cut all the
way through the slab; therefore the sample blank is still in place. The
blanks had an average diameter of 0.015" and were tapered to an approxi-
mate diameter of 0.013" on that end first cut by the tool. In most cases
the metal on the ends of the blanks was intact.

The blanks were then hand ground between two flat hard Arkansas grind
stones to their final diameter of approximately 0.0105". A spacer o.
0.0102" thick polyethylene sheet was cut to the same size as the stones.
A hole was then cut from the center of the spacer and all grinding was
done in this hole. When the grinding action was stopped by the spacer,
the blank's diameter had been reduced to the desired size. During the
grinding, the blank was often put into a dish of light oil under a micro-
scope and the feather edge of the metal on the ends removed with a fine
brush. The blank was then dipped in acetone to remove the oil and the
grinding was resumed. All the grinding was done dry with a circular
motion and with little or no pressure applied to the stones. An end view
and side view of the finished sample is given by the microphotograph of
Fig. 32. As shown in this figure, the metal on the ends of the sample is
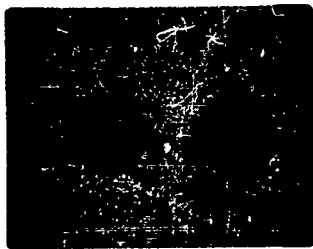
FIG. 31--Microphotograph of dielectric slab after being cut
with the impact grinder. The hole on the left shows
the sample blank in place.

FIG. 32--Microphotograph of ceramic dielectric post. Magni-
fication is 32x.

intact and there is no observable taper. The photograph was taken with a magnification of 32x.

The diameter of the sample used in the large-signal measurements was measured with an optical comparitor and found to be 0.0104" ± 0.0001". The length was 0.0200" ± 0.0001".

There are three reasons for using such a small sample:

(1) The capacitance of the sample should be small in order to use a reasonable value of inductance to resonate the cavity in the desired frequency range and therefore a reasonable length of transmission line.

(2) The length of the post, ℓ , should be small in order to have high electric-field intensities in the dielectric at reasonable power levels.

(3) The radius of the post should be small since a constant field strength within the post is desired; and, as shown elsewhere in this chapter, the longitudinal fields in the post decreased with increasing radius as $J_0(\omega\sqrt{\mu\epsilon'}r)$, (on the basis of a small-signal linear analysis), where the ϵ is that of the dielectric and therefore high; hence the radius, a , must be small in order to have $J_0(\omega\sqrt{\mu\epsilon'}a) \simeq 1$.

E. SMALL-SIGNAL MEASUREMENTS ON CAVITY

The following linear parameters of the circuit shown in Fig. 24 are unknown and must be evaluated before large-signal measurements can be made:

(1) G_0' , the conductance representing the wall losses in the cavity,

(2) a_0 , the linear term in the power series expansion of the nonlinear conductance, G_d , given in Eq. (17),

(3) b_0 , the linear term in the power series expansion of the nonlinear capacitance, C_d , given in Eq. (19),

(4) L , the inductance representing the shorted transmission line,

(5) n , the turns ratio of the input transformer, T_1 ,

(6) m , the turns ratio of the output transformer, T_2 .

In addition, the magnitude of the drive, i_0 , in the circuit of Fig. 25 must be related to the power incident on the cavity, P_{inc} ; and the response of the circuit, v , must be related to the power, P_{out} , absorbed by the load at the output of the cavity.

- 65 -

Since the cavity walls were silver plated, the wall losses are negligibly small when compared to the losses in the dielectric; therefore G_0' can be neglected.

The Q circle measurement technique described by Ginzton[19] was used to determine the unloaded Q of the cavity, Q_0 ; the loaded Q of the cavity, Q_L ; the resonant frequency of the cavity, f_0 ; and the standing-wave ratio of the cavity, r_{in} , when viewed from the input side at the resonant frequency. The values, together with standing-wave ratio of the cavity, r_{out} , when viewed from the output side with $f = f_0$, will determine a_0 , b_0 , n , and m . The results of these small-signal measurements are:

$$
\begin{aligned}
Q_0 &= 44 \\
Q_L &= 31 \\
f_0 &= 2.902 \text{ kMc} \\
r_{in} &= 2.0 \\
r_{out} &= 30 \ .
\end{aligned}
$$

The Q_0 of the cavity, as determined by the Q circle measurements, included the effects of the load at the output; however, as will be shown, the output was so undercoupled that the effect of the output load on Q_0 was negligible. Since the wall losses were much less than the losses in the dielectric, the unloaded Q was approximately

$$
Q_0 \approx Q_d = \frac{1}{\tan \delta} , \tag{42}
$$

where Q_d is the dielectric Q . Hence, the loss tangent of the 73% $BaTiO_3$-27% $SrTiO_3$ ceramic at 2.902 kMc and $123^\circ F$ is

$$
\tan \delta \simeq 0.023 . \tag{43}
$$

The linear capacitance term, b_0 , can be computed from the resonant frequency, f_0 . Using Eq. (41) and the dimensions of the cavity given in Fig. 27, the reactance of the transmission line at the reference plane k-k (see Fig. 23) is

$$
X_L = Z_0 \tan \beta_0 \ell' = 24.7\Omega , \tag{44}
$$

where $\quad \ell' = 0.226 - 0.020 = 0.206"$

$\quad\quad Z_0 = 75\Omega$

$\quad\quad \beta_0 = 2\pi/\lambda_0$

$\quad\quad \lambda_0 = c/f_0 = 10.32 \text{ cm} = 4.06'.$

Now when $f = f_0$, the reactances are given by $X_L = X_C = 1/\omega(C_0 + b_0)$. Thus,

$$(C_0 + b_0) = \frac{1}{X_C\omega} = 2.22 \ \mu\mu f \ ; \tag{45}$$

and with Eq. (39) the dc term in the expansion for Cd is determined to be

$$b_0 \approx 2.53 - C_0 = 2.10 \ \mu\mu f \ . \tag{46}$$

The real part of the relative dielectric constant can be obtained by using Eq. (46) in Eq. (35), and at $123°F$ and $f = 2.902 \text{ kMc}$ is

$$k' = \frac{b_0 \ell}{\epsilon_0 A} = 2200 \ . \tag{47}$$

The inductance, L , can be determined by rewriting Eq. (44) as

$$L = \frac{X_L}{\omega} = \frac{Z_0}{\omega} \tan \frac{2\pi\ell'}{\lambda} \ . \tag{48}$$

The large-signal measurements were taken in the frequency range from 2.6 to 3.1 kMc. At $f = 2.6$ kMc, Eq. (48) gives $L = 1.34$ mμh , while at $f = 3.1$, the inductance is $L = 1.36$ mμh . This is a change in L of less than 2%; hence an average value of

$$L = 1.35 \text{ m}\mu\text{h} \tag{49}$$

will incur less than 1% error.

The small-signal Q_0 of the circuit in Fig. 25, when G_0' is neglected, is

$$Q_0 = \frac{\omega(C_0 + b_0)}{a_0} \ . \tag{50}$$

By rearranging Eq. (50) and using the known values of $\omega_0 = 2\pi f_0$, C_0 , b_0 , and Q_0 , the value of a_0 is determined to be

$$a_0 = \frac{\omega_0(C_0 + b_0)}{Q_0} = 0.92 \times 10^{-3} \text{ mhos} \ . \tag{51}$$

The turns ratio, n, of the input transformer, T_1, can be determined in two ways. The first involves Q_L and the second involves the standing-wave ratio, r_{in}, of the cavity when $f = f_0$ and when the cavity is viewed from the input side.

The loaded Q of the circuit of Fig. 25, when G_0' and the effect of the load admittance are neglected, is

$$Q_L = \frac{\omega_0(C_0 + b_0)}{n^2 Y_0 + a_0} . \tag{52}$$

Equation (52) can be solved for n and, when the known values of ω, C_0, b_0, Y_0, a_0, and Q_L are used, yields

$$n = \left\{ \frac{1}{Y_0} \left[\frac{\omega_0(C_0 + b_0)}{Q_L} - a_0 \right] \right\}^{1/2} = 0.139 . \tag{53}$$

To evaluate n by the second method, consider the circuit of Fig. 24 when the output admittance, Y_0, and G_0' are neglected, when $f = f_0$, and when all the impedances (now real) are reflected into the input side of T_1.
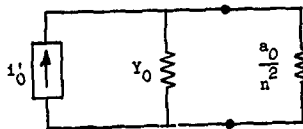
FIG. 33--Equivalent circuit for cavity when resonant and viewed at the input.

The cavity is undercoupled by the input loop; hence its impedance at resonance is less than the characteristic impedance of the input transmission line. Ginzton shows[20] that in this special case,

$$r = \frac{Z_0}{Z_L} = \frac{Y_L}{Y_0} , \tag{54}$$

- 68 -

where $\quad r = r_{in}$.
$\qquad Y_L = a_0/n^2$.

The measured value of r_{in} is 2.0; hence from Eq. (54)

$$n = \left[\frac{a_0}{r_{in}Y_0}\right]^{1/2} = 0.152 .$$ (55)

The values of n obtained in Eqs. (53) and (55) agree within 9%. The average of the two values will be used and is

$$n = 0.146 .$$ (56)

The turns ratio, m, of the output transformer, T_2, can be determined with the standing-wave ratio, r_{out}, of the cavity when $f = f_0$ and when the cavity is viewed from the output side. The output coupling is very light and since the impedance presented by the cavity is resistive, Eq. (54) can again be used:

$$r = \frac{Z_0}{Z_L} = \frac{Y_L}{Y_0} ,$$ (57)

where $r = r_{out}$. In this case, however, the resistance coupled into the cavity from the input side can not be neglected; hence the circuit of Fig. 24 becomes that of Fig. 34 when G_0' is neglected, when $f = f_0$, and when all the impedances are transferred to the output side of T_2.
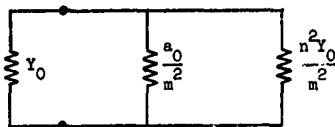
FIG. 34--Equivalent circuit for cavity when resonant
and viewed at the output.

The circuit of Fig. 34 shows that Y_L in Eq. (57) is

$$Y_L = \frac{n^2 Y_0}{m^2} + \frac{a_0}{m^2}. \tag{58}$$

By substituting Eq. (58) into Eq. (57), using the known values of n, Y_0, a_0, and r_{out}, and solving for m, one obtains

$$m = \left[\frac{n^2 Y_0 + a_0}{r_{out} Y_0} \right]^{1/2} = 0.0475. \tag{59}$$

It was assumed that, as a result of the light output coupling, the effect of the load, Y_0, on Q_0 and on the input impedance of the cavity at resonance could be neglected. This assumption was used in Eqs. (42), (50), (52), and (54), and can now be checked. When reflected into the cavity, the output load is

$$m^2 Y_0 = 0.045 \times 10^{-3}, \tag{60}$$

and is 4.9% of a_0; hence the maximum error incurred with this assumption is 4.9%--an acceptable error when compared to those incurred elsewhere.

To obtain the magnitude, P, of the drive, i_0, in terms of the power incident on the cavity, P_{inc}, consider the circuit of Fig. 35 where it is assumed that the cavity presents a matched load to the line and that the constant current generator is that of Fig. 24.
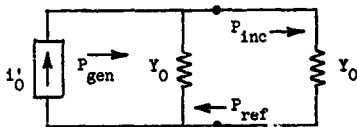
FIG. 35--Equivalent circuit of Fig. 24 when the cavity is assumed to be matched to the generator.

Since the load is matched, all the power incident on the cavity is absorbed and none is reflected. The total power output, P_{gen}, of the ideal current generator, i'_0, is

$$P_{gen} = \frac{i'^2_0}{4Y_0} . \tag{61}$$

Half of this power is absorbed by the generator admittance, Y_0, and half is carried as P_{inc} to the cavity admittance; hence in this matched system,

$$P_{inc} = \frac{P_{gen}}{2} = \frac{i'^2_0}{8Y_0} , \tag{62}$$

or,

$$i'_0 = \left[8Y_0 P_{inc} \right]^{1/2} . \tag{63}$$

Now assume that the load presented by the cavity is changed. The power output of the generator, P_{gen}, will also change; however, the generator admittance will now be absorbing not only power from the generator but also the power reflected from the cavity, P_{ref}, due to the mismatch. But by definition, the magnitude of the current output of the generator, $\left| i'_0 \right|$, has not changed, and therefore the power incident on the cavity has not changed. Thus, in the large-signal measurements, keeping the power incident on the cavity constant is equivalent to keeping the magnitude of the current generator in Fig. 25, $\left| i_0 \right| = P$, constant. By reflecting the current generator, i'_0, across the input transformer, T_1, and using Eq. (63), the magnitude of the generator in Fig. 25 can be written as

$$P = \left| n i'_0 \right| = n \left[8Y_0 P_{inc} \right]^{1/2} = 0.058 \, P_{inc}^{1/2} , \tag{64}$$

where from Eq. (32)

$$P = \left| i_0 \right| = \left| A \cos \omega t + B \sin \omega t \right| = \left[A^2 + B^2 \right]^{1/2} .$$

The voltage, v, across the nonlinear capacitance, C_d, is linearly related to the power absorbed in the output load of the cavity. In

reference to Fig. 24, the power absorbed in the load admittance is

$$P_{out} = \frac{v_L^2 Y_0}{2} . \tag{65}$$

By writing Eq. (65) in terms of v instead of v_L and solving for A_0, one obtains

$$A_0 = |v| = \frac{1}{m}\left[\frac{2 \, P_{out}}{Y_0}\right]^{1/2} = 210 \, P_{out}^{1/2} . \tag{66}$$

In summary, the values of the linear parameters in the circuit of Fig. 25 have been obtained in Eqs. (51), (39), (46), (56), (59), and (49), respectively, and are

$$G_0 = (n^2 + \hat{m}\,)Y_0 = 0.43 \times 10^{-3} \text{ mhos}$$
$$a_0 = 0.92 \times 10^{-3} \text{ mhos}$$
$$C_0 = 0.12 \ \mu\mu f$$
$$b_0 = 2.10 \ \mu\mu f$$
$$n = 0.146$$
$$m = 0.0475$$
$$L = 1.35 \ \mu h ,$$

and from Eqs. (64) and (66) the magnitude of the drive, $|i_0|$, and the response, $|v|$, are

$$P = |i_0| = 0.058 \, P_{inc}^{1/2}$$
$$A_0 = |v| = 210 \, P_{out}^{1/2} .$$

Thus, in the large-signal measurements, curves of the response of the cavity with a constant incident power level can be obtained by measuring the power absorbed by the load as a function of frequency. These curves can then be used with Eqs. (64) and (66) to solve Eq. (34) ~ multaneously for the unknowns a_2, a_4, b_2, and b_4.

F. LARGE-SIGNAL MEASUREMENTS

1. Preliminary Considerations

The response curve of a linear resonant system, when plotted for a constant drive level as a function of the drive frequency, is a symmetrical resonance curve. However, if the system contains a nonlinear element, the curve of the response will no longer be symmetrical but will be skewed toward higher or lower frequencies depending upon the sign of the coefficients describing the nonlinearity. If the losses in the nonlinear system are not too great and if a large enough drive is used, the response can be expected not only to skew but also to have a frequency range in which the curve is double-valued. This type of behavior is discussed by many authors[16,17,18] and predicted from equations that are similar in form to Eq. (34). However, to show the double-valued portion of the curve, it is ne   ary to sweep the frequency into the bistable region as shown in Fi   . To establish the upper branch, the frequency of the drive must start from below the double-valued region and sweep upwards until there is a discontinuous jump downward in the response; and to establish the lower branch, the frequency must be swept from above the bistable region until a discontinuous jump upward is experienced.

When the small-signal measurements described in the previous section were made on the cavity, the temperature of the ceramic dielectric post could be assumed to be that of the cavity. However, if large rf fields are established in the cavity, the power carried in these fields will be dissipated in the dielectric with the result that its temperature will rise. Therefore, in order to maintain the dielectric post at the cavity temperature, all the large-signal measurements were made with pulsed power. But with a pulsed system, the frequency sweeps necessary to show the double-valued portions of the response curve are not possible; hence a hysteresis such as that shown in Fig. 36 may not be seen.

When the measurements are made with pulsed power, the cavity must reach the steady state in a time that is short compared to the pulse length. The fields in a cavity will reach 1/e of their final value in Q_L/π cycles. Hence, on a linear basis, the time constant of this cavity is

$$\tau = \frac{2Q_L}{\omega} = 3.4 \ \mu\text{sec} , \qquad (68)$$
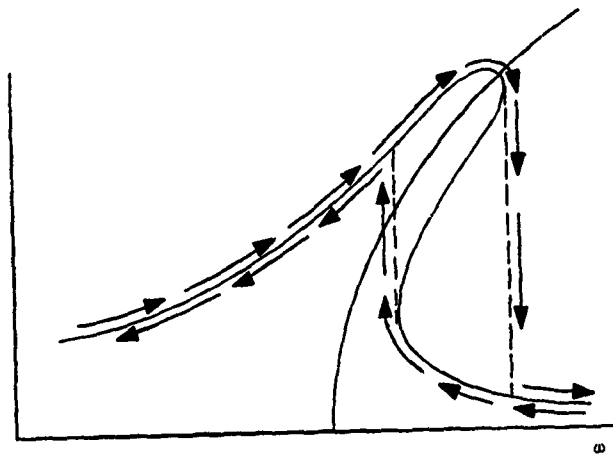
FIG. 36--Typical curve of the response of a resonant system
containing a nonlinear element (after Stoker[19]).

where the frequency is that of the small-signal resonance. The cavity
can be assumed to have reached the steady state in 4τ or approximately
14 mµsec. The shortest pulse length used in the large-signal measure-
ments was 1.4 µsec; thus, a negligible error was introduced by neglecting
the effects of electrical transients in the cavity.

As shown in Appendix F, a negligible error (i.e., less than 2%) was
introduced by assuming that the electric field was constant across the
dielectric post.

2. Instrumentation

A block diagram of the instrumentation used in the large-signal
measurements is given in Fig. 37. The klystron oscillator supplied a
continuous signal to the traveling-wave amplifiers. The final amplifier
was triggered 10 times per second and supplied a 1.4 µsec pulse to the
cavity. The power incident on the cavity was monitored through a 20 db
directional coupler with a thermistor and power meter so that it could be
kept at a constant level by means of the variable attenuator. The inci-
dent power was also sampled by a 20 db directional coupler and put through
a transmission wavemeter to a crystal. The output of the crystal was fed
to vertical channel no. 1 on the oscilloscope for observation of the pulse
shape and determination of the frequency. The power transmitted by the
cavity to the output load was sampled with a 10 db directional coupler
and broadband crystal, and the power level at the crystal could be con-
trolled with the precision variable attenuator. The output of the crystal,
after being amplified with a 30 db amplifier, was fed to vertical input
channel no. 2 on the oscilloscope. For each point of the data, the pre-
cision attenuator was set to give a 3 cm displacement on the oscilloscope,
and the necessary attenuation was read and used to calculate the peak
output power of the cavity. This procedure was repeated at different
frequencies with a constant incident power level until a complete curve
of the cavity response was obtained.

The equipment used to measure the cavity response was calibrated by
removing the cavity from the circuit and placing a matched load at point B
in Fig. 37. The variable attenuator was set to give a convenient power
level at point C where the average power level was read with the thermis-
tor and power meter. Following this, the thermistor was removed and
point A was connected to point C. The attenuation needed to give the 3 cm

- 75 -
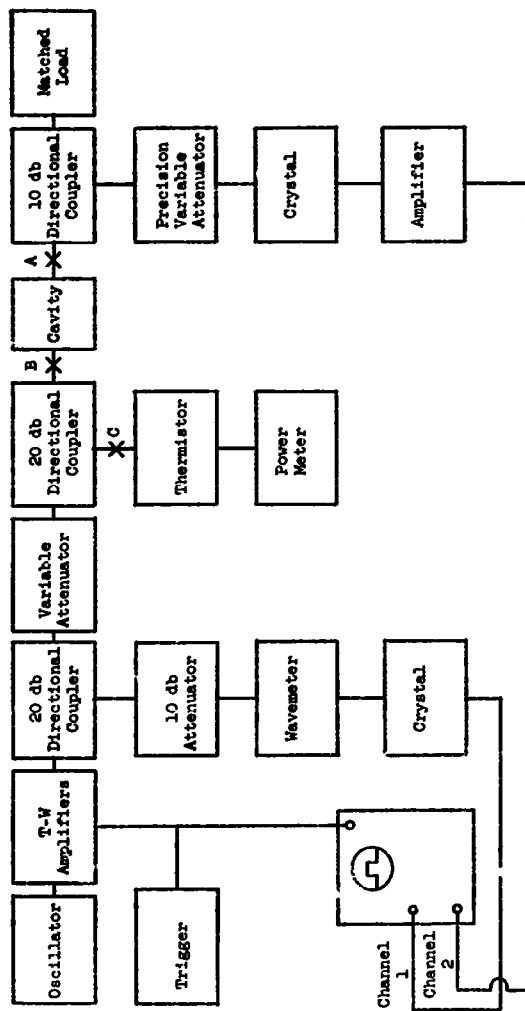
FIG. 31.--Block diagram of apparatus used in large-signal measurements.

deflection on the oscilloscope was found on the precision variable attenu-
ator and read. The peak power at point A was then calculated from the
average power reading given by the thermistor, and finally, the peak power
needed at point A to given the 3 cm deflection when no attenuation was
set into the precision attenuator was calculated. Hence all the readings
of attenuation obtained during the experimental runs gave the peak power
level at the cavity output, point A, as the number of db above the cali-
bration signal level.

3. Thermal Effects

The shape of the cavity output pulse as seen on the oscilloscope
depended upon the frequency of the applied signal. This variation of
shape with frequency is shown by the photographs of the oscilloscope
trace given in Fig. 38 where. in all cases, the sweep was 1 cm/μsec.
Figure 38a shows the 1.4 μsec incident pulse from the final amplifier;
while Figs. 38b, 38c, 38d, and 38e show the output pulse when the fre-
quency of the drive was varied through the resonance from low to high
frequencies, respectively, and when the precision variable attenuator
was set to give a 3 cm deflection on the oscilloscope. Figure 38b was
taken when the frequency was far below resonance and shows a slight drop
in the magnitude of the pulse from its initial value (the pulse starts
on the right in the photographs). As the frequency of the drive was
increased, the magnitude of the output pulse increased as did the rate
at which the pulse magnitude fell off with time until a frequency was
reached at which the initial value of the pulse was at a maximum. The
pulse shape at this frequency is shown in Fig. 38c. As the frequency of
the drive was increased still further, the peak of the response became
displaced in time from the start of the pulse. That is, the peak would
move to the left in the photographs as the frequency was increased
(Fig. 38d) until it had moved completely off the pulse (Fig. 38e). The
output level of the pulse shown in Fig. 38d 's approximately 12 c.n above
that shown in Fig. 38e. This motion of the peak of the response is better
shown with a longer pulse. Figure 39a shows an incident pulse of approxi-
mately 7 μsec duration. Figure 39b shows the output pulse when the fre-
quency was slightly above that where the initial response was at a maximum
and shows that the peak of the response occurred approximately 0.5 μsec
after the start of the pulse; while Figs. 39c and 39d show that when the

- 77 -

(a) Incident Pulse

(b) f = 2.593 kMc

(c) f = 2.948 kMc

(d) f = 3.090 kMc
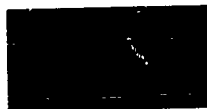
(e) f = 3.110 kMc

FIG. 38--Oscilloscope trace photographs of the cavity output pulse at various frequencies when the peak incident power level is 2000 watts. The sweep speed is 1 cm/μsec and time increases to the left.

(a) Incident Pulse

(b) f = 3.140 kMc

(c) f = 3.178 kMc

(d) f = 3.233 kMc

FIG. 39--Oscilloscope trace photographs of the cavity
output pulse at various frequencies when the
peak incident power level is 2000 watts. The
sweep speed is 1 cm/μsec and time increases
to the left.

frequency was further increased, the peak of the response was displaced
approximately 1.7 μsec and 5.4 μsec, respectively, from the start of the
pulse.

The cause of this phenomenon can be understood by considering the
heat generated in the ceramic during a single pulse. The dielectric post
is virtually an isolated thermal system during the time of the pulse
because its thermal conductivity was low; hence during the pulse the
ceramic did not rid itself of the heat generated by the rf fields, and
its temperature therefore rose. An approximation of the temperature rise
can be obtained by considering the following elementary equation:

$$Q = cm\Delta T \tag{69}$$

where   Q   is heat in cal,

       c   is the specific heat in cal/g·$^\circ$C ,

       m   is mass in g , and

       ΔT is the change in temperature in $^\circ$C .

The density of the ceramic was determined to be 5.2 g/cc and the mass of
the dielectric post was calculated to be 1.33×10^{-4} g. It is reasonable
to assume that the specific heat of the ceramic was approximately
0.2 cal/g·$^\circ$C. If it is also assumed that the peak input power to the
cavity (hence the power dissipated in the ceramic post) was 1 kw, that
the ceramic post was an isolated thermal system and that the electrical
system was linear, then the temperature rise during a 1.4 μsec pulse
calculated from Eq. (69), was

$$\Delta T = \frac{Q}{cm} \simeq 12.6^\circ C = 22.6^\circ F \ . \tag{70}$$

The small-signal resonance of the cavity occurred at approximately 2.9 kMc
when the temperature of the dielectric was 123°F; however, if its tempera-
ture were 150°F, the resonance would have occurred at a higher frequency
due to the change in the dielectric constant. From Fig. 6 the relative
dielectric constant of this ceramic at 123°F is approximately 2100 while
at 150°F it is approximately 1550. Since the small-signal resonant fre-
quency would be shifted by approximately the square root of the ratio of
the dielectric constant at the lower temperature to that at the higher
temperature, the resonant frequency would shift by a factor of approxi-
mately 1.16 or from 2.9 kMc at 123° to 3.4 kMc at 150°F.

- 80 -

On the basis of the simplified analysis made above, one can predict the manner in which the magnitude of the cavity response would vary during the time of a pulse when the cavity is driven with a high-power incident pulse whose magnitude is constant. The initial response, as seen on the oscilloscope, would be proportional to the fields in the cavity when the temperature of the dielectric was that of the cavity (123°F) and when the maximum of the resonance curve was in the region of 2.9 kMc. But as time increased, the temperature of the dielectric would rise until, at the end of the pulse, the response would be proportional to the cavity fields when the temperature of the dielectric was greater than that of the cavity (150°F) where the maximum of the resonance curve would now occur at a higher frequency (3.4 kMc). This is roughly equivalent to the resonance curve sliding toward higher frequencies during the time of the pulse. If the frequency of the drive were above 2.9 kMc but below 3.4 kMc, one could expect that, during the pulse, the response would start at a low value, build up to a peak and then fall off. As shown by Figs. 38d, 39b, 39c, and 39d, this is what was observed.

This analysis does not take into account either the nonlinearity of the dielectric or the changes in the nonlinearity of the dielectric which probably occur during the time of the pulse. Also, it was assumed that the input power was constant when, in fact, the incident power was held constant and the shape of reflected pulse was the inverse of that of the response pulse. The analysis does indicate, however, that only the initial response of the cavity should be used for the measurements.

Another thermal effect must also be considered. If the heat generated by the rf in the dielectric during a pulse is not dissipated before the next pulse, the initial response of the cavity will be for the ceramic operating at some temperature above that measured with the thermometer. To insure that this was not happening, the pulse repetition frequency was reduced while monitoring the shape of the output pulse. The system was triggered automatically at 10 pulses per second and then triggered manually at approximately 1 pulse per second. No change in either the initial response or in the overall pulse shape was observed; however, when the trigger rate was set at 100 pulses per second, the response was radically changed. A pulse repetition frequency of 10 pulses per second was therefore used in all the large-signal measurements.

4. Results

Curves of the peak output power of the cavity are given in Fig. 40 as a function of frequency for three constant incident power levels.

The portions of the response curves on the high-frequency side of the maxima are not shown since here the initial response of the cavity was obscured by the heating effect and, at any given incident power level, it was necessary to increase the frequency until the peak of the response was well removed from the start of the pulse and an initial step was evident as shown in Figs. 38d and 39b.

The curves of Fig. 40 can be used with Eq. (34) to determine the unknown coefficients,

$$P^2 = \left\{ (a_0 + G_0)A_0 + \frac{3}{4} a_2 A_0^3 + \frac{5}{8} a_4 A_0^5 \right\}^2$$
$$+ \left\{ \left[\omega(C_0 + b_0) - \frac{1}{\omega L} \right] A_0 + \frac{3}{4} b_2 \omega A_0^3 + \frac{5}{8} b_4 \omega A_0^5 \right\}^2 .$$

The constant parameters of this equation have been evaluated in Eqs. (39), (46), (49), (51), (56), (59), (64), and (65) and are:

$$a_0 = 0.92 \times 10^{-3} \text{ mhos}$$
$$G_0 = (n^2 + m^2)Y_0 = 0.43 \times 10^{-3} \text{ mhos}$$
$$b_0 = 2.10 \text{ μμf}$$
$$C_0 = 0.12 \text{ μμf}$$
$$L = 1.35 \text{ μμh}$$
$$P = 0.058 \ P_{inc}^{1/2} \text{ where } P_{inc} \text{ is in watts of peak power}$$
$$A_0 = 210 \ P_{out}^{1/2} \text{ where } P_{out} \text{ is in watts of peak power.}$$

Using these values, Eq. (34) becomes

$$3.36 \times 10^{-3} \frac{P_{inc}}{P_{out}} = \left\{ 0.283 + 6.95 \times 10^6 \ P_{out} \ a_2 + 2.56 \times 10^{11} \ P_{out}^2 \ a_4 \right\}^2$$
$$+ \left\{ \left[2.94 \times 10^{-9} f - \frac{24.8 \times 10^9}{f} \right] \right.$$
$$\left. + 4.36 \times 10^7 f \ P_{out} \ b_2 + 1.61 \times 10^{12} f \ P_{out}^2 \ b_4 \right\}^2 .$$

$$(71)$$
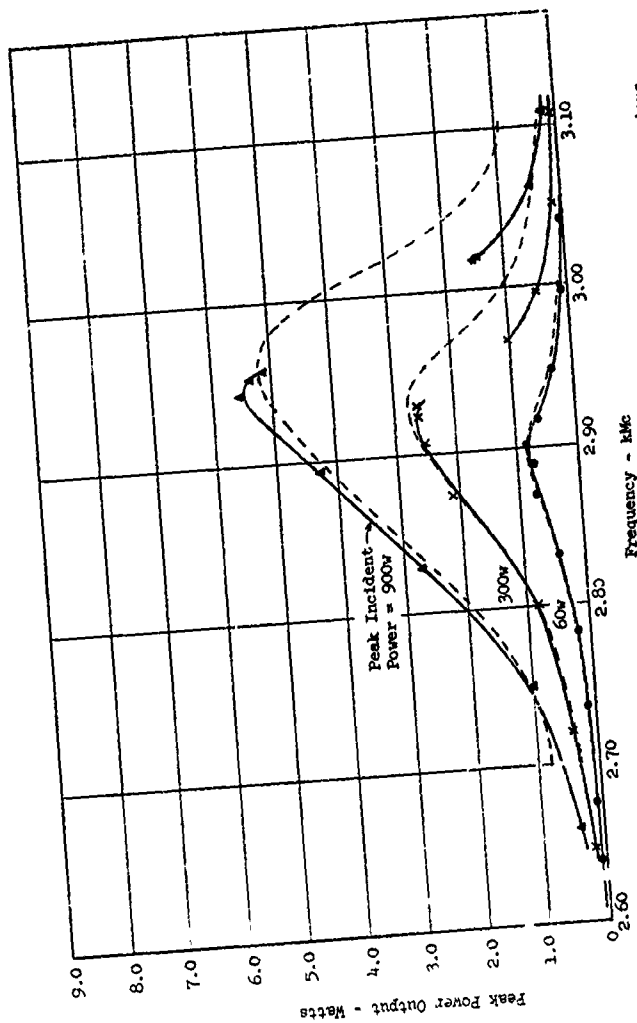
FIG. 40.--Peak output power of coaxial cavity as a function of frequency for various peak incident power levels. The dashed curves are theoretical.

- 83 -

The use of a Burroughs 220 computer to solve Eq. (71) simultaneously with values of P_{inc}, P_{out}, and f taken from the curves of Fig. 40 indicated that the experimental errors were too large to allow a_4 and b_4 to be determined but that a range for a_2 and b_2 could be estimated. The estimated range of a_2 was

$$- 1 \times 10^{-8} < a_2 < 1.5 \times 10^{-8} \ ,$$

and that of b_2 was

$$- 2 \times 10^{-18} < b_2 < 0 \ .$$

These limits on a_2 and b_2 are so broad as to be virtually meaningless.

It was therefore decided that, after dropping the terms involving a_4 and b_4, Eq. (71) should be fitted to the curves of Fig. 40. The largest error in the constant terms of Eq. (71) could be expected to occur in the turns ratio, m, of the output transformer in the equivalent circuit, since, as shown by Eq. (59), the calculated value of this ratio includes the errors arising from the determination of the input turns ratio n, from the determination of the loss term a_0, and from the measurement of the large standing-wave ratio r_{out}. As can be seen from Eqs. (34) and (66), a change in m has a relatively large effect since the square as well as the sixth power of the reciprocal of this ratio enters into Eq. (71) when the terms in a_4 and b_4 are dropped. To offset this error, Eq. (71) was fitted to the 60 watt curve of Fig. 40 (since here the contribution of the nonlinear terms is relatively small) with a change in m of 1.6. Curves were then plotted using the modified form of Eq. (71) with various values of a_2 and b_2. In this way it was possible to set much narrower limits on a_2 and b_2 than those obtained with the computer because a relatively small change in the value of either term radically changed the shape of the plotted curves. The estimated value of a_2 is

$$a_2 = + 2.4 \times 10^{-9} \pm 1.0 \times 10^{-9}$$

while that of b_2 is

$$b_2 = - 2.4 \times 10^{-19} \pm 0.6 \times 10^{-19} \ .$$

It is felt that these limits are wide enough to allow additional correction of the turns ratio or changes in the other linear terms. These

values agree with those obtained during the testing of an harmonic generator which employs this ceramic dielectric as its nonlinear element and which has been designed and built in this laboratory.

The dashed curves of Fig. 40 are plotted with values of $+2.4 \times 10^{-9}$ and -2.4×10^{-19} for a_2 and b_2 respectively and, while the fit is not exact, changes on the order of 10% in either a_2 or b_2 caused the fit to deteriorate markedly.

The value of the rf conductivity of the ceramic (73% $BaTiO_3$-27% $SrTiO_3$) can be calculated from the value of a_2 and Eq. (17) and is

$$\sigma(E) = \frac{\ell}{A} \sum_{n \text{ even}} a_n (\ell E)^n \approx 8.5 + (5.7 \times 10^{-12} \pm 2.4 \times 10^{-12}) E^2 \text{ mhos/meter}$$

where ℓ is the length o. the dielectric post in meters

A is the cross-sectional area of the post in square meters and

E is the electric field intensity in volts per meter.

The large-signal dielectric constant can be similarly obtained with Eq. (19) and is

$$\epsilon'(E) = \frac{\ell}{A} \sum_{n \text{ even}} b_m (\ell E)^2 \approx \epsilon_0 [2200 - (6.5 \times 10^{-11} \pm 1.6 \times 10^{-11}) E^2]$$

where ϵ_0 is the dielectric constant of free space.

The peak incident power levels of the curves shown in Fig. 40 range from 60w to 900w, and the corresponding peak rf fields established in the dielectric can be obtained with Eq. (66) and the maxima of the curves of the cavity response. Using this equation and the correction factor for m , the peak electric fields in the dielectric were

$$E = \frac{|v|}{\ell} = \frac{210 \ P_{out}^{1/2}}{\ell} \times 1.6 = 6610 \ P_{out}^{1/2} . \tag{72}$$

From Fig. 40 and Eq. (72), the maximum electric field in the dielectric ranged from approximately 6.0 kv/cm with 60 w peak incident power to 15.5 kv/cm with 900w peak incident power.

The field strength obtained experimentally from the 60 watt curve and Eq. (72) can be used to check the correction factor for m by calculating the field strength in the dielectric with the definition of Q

- 83 -

and the expression for energy storage:

$$Q = \frac{\omega W}{P}$$

$$W = \frac{1}{2} \int \epsilon E^2 dV = \frac{1}{2} \epsilon E^2 V \ ,$$

where, in this case,

      W is the energy stored in the cavity

      P is the power dissipated $= P_{inc}[(r_{in} - 1)/(r_{in} + 1)]^2$

      V is the volume of the dielectric cylinder, and

      E is assumed to be a constant in the dielectric.

Solving for E and substituting the known values of Q , ω , P , ϵ , and V gives a maximum electric field field in the dielectric of 6.5 kv/cm. This value is within 10% of that obtained above and is, therefore, a reasonable check on the correction factor for m .

    A more accurate method for measuring the nonlinearity of a ceramic dielectric would probably result from casting the response of the equivalent circuit in terms of the power reflected by the cavity for in this case it would not be necessary to use an output transformer whose turns ratio could only be obtained with a limited accuracy.

SOLUTION OF BOUNDARY VALUE PROBLEM FOR SMALL-SIGNAL MEASUREMENTS

The geometry used is that of Fig. A.1.
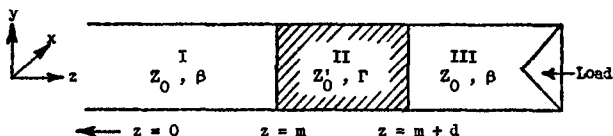
FIG. A.1--Schematic diagram of sample configuration.

For Fig. A.1,

> Region I, an air-filled section of the waveguide, has a real
> characteristic impedance, Z_0 , and a real propagation
> constant, β .

> Region II, a section of the waveguide which is filled with a
> nonlinear dielectric, extends from $z = m$ to $z = m + d$;
> and has both a complex characteristic impedance, Z_0' , and
> a complex propagation constant, Γ .

> Region III, an air-filled section of the waveguide, is termin-
> ated by a matched load and has a real characteristic imped-
> ance, Z_0 , and a real propagation constant, β .

Since both faces of the dielectric are perpendicular to the axis of the
waveguide, only the dominant mode should be excited. And since wall
losses in the waveguide can be neglected when compared to those in the
dielectric, the fields in Regions I, II, and III can be written as.

$$\text{Region III:} \quad E_y = Ae^{-j\beta z}$$

$$R_x = \frac{A}{Z_0} e^{-j\beta z} \qquad\qquad (A.1)$$

Region II: $E_y = Be^{-\Gamma z} + Ce^{+\Gamma z}$

$$H_x = \frac{B}{Z_0'} e^{-\Gamma z} - \frac{C}{Z_0'} e^{+\Gamma z}$$

$$\quad (A.1)$$

Region I: $E_y = De^{-j\beta z} + Ee^{+j\beta z}$

$$H_x = \frac{D}{Z_0} e^{-j\beta z} - \frac{E}{Z_0} e^{+j\beta z}$$

where A , B , C , D , and E are functions of x and y , and the time dependency, $e^{j\omega t}$, is assumed but not written.

The boundary conditions are that E_y and H_x must be continuous at $z = m$ and $z = m + d$, hence

$$\left. \begin{array}{l} E_{y,I} = E_{y,II} \quad \text{and} \quad H_{x,I} = H_{x,II} \quad \text{at } z = m \\[2mm] E_{y,II} = E_{y,III} \quad \text{and} \quad H_{x,II} = H_{x,III} \quad \text{at } z = m + d \end{array} \right\} \quad (A.2)$$

Substituting Eqs. (A.1) into Eqs. (A.2) yields

$$\left. \begin{array}{l} De^{-j\beta m} + Ee^{+j\beta m} = Be^{-\Gamma m} + Ce^{+\Gamma m} \\[3mm] \dfrac{D}{Z_0} e^{-j\beta m} - \dfrac{E}{Z_0} e^{+j\beta m} = \dfrac{B}{Z_0'} e^{-\Gamma m} - \dfrac{C}{Z_0'} e^{+\Gamma m} \\[3mm] Be^{-\Gamma(m+d)} + Ce^{+\Gamma(m+d)} = Ae^{-j\beta(m+d)} \\[3mm] \dfrac{B}{Z_0'} e^{-\Gamma(m+d)} - \dfrac{C}{Z_0'} e^{+\Gamma(m+d)} = \dfrac{A}{Z_0} e^{-j\beta(m+d)} \end{array} \right\} \quad (A.3)$$

Letting $z = m = 0$ and solving Eqs. (A.3) simultaneously for D/A , gives

$$\frac{D}{A} = \frac{Z_0 Z_0'}{4} e^{-j\beta d} \left[\left(\frac{1}{Z_0} + \frac{1}{Z_0'} \right)^2 e^{+\Gamma d} - \left(\frac{1}{Z_0} - \frac{1}{Z_0'} \right)^2 e^{-\Gamma d} \right] . \quad (A.4)$$

The transmission through the dielectric is

$$T = \frac{\text{Power to the load in Region III}}{\text{Power incident to the dielectric in Region I}} = \frac{A}{D} \frac{A^*}{D^*} , \quad (A.5)$$

where * indicates the complex conjugate.

Substituting Eq. (A.4) into Eq. (A.5) and noting that Z_0 and β are real while Z_0' and Γ are complex, gives the reciprocal of transmission as

$$\frac{1}{T} = \frac{D}{A}\frac{D^*}{A^*} = \left\{ \frac{Z_0 Z_0'}{4} e^{-j\beta d} \left[\left(\frac{1}{Z_0} + \frac{1}{Z_0'}\right)^2 e^{+\Gamma d} - \left(\frac{1}{Z_0} - \frac{1}{Z_0'}\right)^2 e^{-\Gamma d}\right]\right\}$$

$$\left\{ \frac{Z_0 Z_0'^*}{4} e^{+j\beta d} \left[\left(\frac{1}{Z_0} + \frac{1}{Z_0'^*}\right)^2 e^{+\Gamma^* d} - \left(\frac{1}{Z_0} - \frac{1}{Z_0'^*}\right)^2 e^{-\Gamma^* d}\right]\right\}$$

$$= \frac{1}{16 Z_0^2 Z_0' Z_0'^*} \left| (Z_0 + Z_0')^2 e^{+\Gamma d} - (Z_0 - Z_0')^2 e^{-\Gamma d}\right|^2 . \tag{A.6}$$

In order to reduce Eq. (A.6), expressions for Z_0, Z_0', and Γ are needed. The wave equation for transverse electric waves in rectangular waveguide is

$$\nabla_T^2 H_z = -k_c^2 H_z , \tag{A.7}$$

where in Region II,

$$k_c^2 = \Gamma^2 + k^2 = \Gamma^2 + \omega^2 \mu \epsilon , \tag{A.8}$$

and ∇_T^2 is the Laplacian operator taken with respect to the transverse coordinates, x and y.

From the solution of Eq. (A.7)[22] it can be shown that, in Regions I and III,

$$Z_0 = Z_{TE} = \sqrt{\frac{\mu_0}{\epsilon_0}} \left[1 - \left(\frac{f_c}{f}\right)^2\right]^{-1/2} , \tag{A.9}$$

where f_c is the cutoff frequency of the air-filled waveguide, and
μ_0 is the permeability of free space.

For the dominant TE_{10} mode in the waveguide, k_c is given by

$$k_c = k_x = \frac{\pi}{a} , \tag{A.10}$$

where a is the width of the waveguide, i.e., the x-dimension.
The definitions of the complex dielectric constant and loss tangent have already been given and are Eqs. (2) and (4), respectively:

$$\epsilon = \epsilon' - j\epsilon'' \quad \text{and} \quad \tan \delta = \frac{\epsilon''}{\epsilon'} .$$

Substituting Eqs. (4), (2), and (A.10) into Eq. (A.8), results in

$$\Gamma = \left[\left(\frac{\pi}{a}\right)^2 - \omega^2\mu\epsilon'(1 - j\tan\delta)\right]^{1/2} . \tag{A.11}$$

It is assumed that for the nonlinear dielectrics of interest
$(\epsilon'/\epsilon_0) = k' \geq 100$, hence,

$$\omega^2\mu_0\epsilon' \gg \left(\frac{\pi}{a}\right)^2 . \tag{A.12}$$

Therefore, Eq. (A.11) can be written

$$\Gamma \cong \left[-\omega^2\mu_0\epsilon'(1 - j\tan\delta)\right]^{1/2} = j\omega\sqrt{\mu_0\epsilon'}\left[1 - j\tan\delta\right]^{1/2} . \tag{A.13}$$

Using a binomial series expansion for Eq. (A.13) produces

$$\Gamma \cong j\omega\sqrt{\mu_0\epsilon'}\left[1 - j\frac{\tan\delta}{2} + \frac{\tan^2\delta}{8} - \dots\right] . \tag{A.14}$$

It can be assumed that in Region II $\tan^2\delta \ll 1$; therefore Eq. (A.14)
becomes

$$\Gamma \cong j\omega\sqrt{\mu_0\epsilon'}\left[1 - j\frac{\tan\delta}{2}\right] . \tag{A.15}$$

Also in Region II, the complex characteristic impedance is

$$Z_0' = Z_{TE} = \frac{j\omega\mu_0}{\Gamma} . \tag{A.16}$$

Substituting Eq. (A.15) into Eq. (A.16), gives

$$Z_0' = \sqrt{\frac{\mu_0}{\epsilon'}}\frac{1}{[1 - j(\tan\delta)/2]} = \sqrt{\frac{\mu_0}{\epsilon'}}\left[1 + j\frac{\tan\delta}{2}\right] . \tag{A.17}$$

Substituting Eqs. (A.15) and (A.17) into Eq. (A.6), neglecting the term
involving $\tan^2\delta$, and simplifying, results in

$$\frac{1}{T} = \frac{1}{16Z_0^2(\mu_0/\epsilon')}\left[\left(Z_0 + \sqrt{\frac{\mu_0}{\epsilon'}}\right)^4 \exp\left(\omega\sqrt{\mu_0\epsilon'}\,d\,\tan\delta\right)\right.$$

$$+ \left(Z_0 - \sqrt{\frac{\mu_0}{\epsilon'}}\right)^4 \exp\left(-\omega\sqrt{\mu_0\epsilon'}\,d\,\tan\delta\right) - 2\left(Z_0^2 - \frac{\mu_0}{\epsilon'}\right)^2 \cos 2d\omega\sqrt{\mu_0\epsilon'}$$

$$\left. + 4Z_0\sqrt{\frac{\mu_0}{\epsilon'}}\tan\delta\left(Z_0^2 - \frac{\mu_0}{\epsilon'}\right)\sin 2d\omega\sqrt{\mu_0\epsilon'}\right] . \tag{A.18}$$

Since it has been assumed that $(\epsilon'/\epsilon_0) \geq 100$, the term involving $\sin 2d\omega\sqrt{\mu_0\epsilon''}$ in Eq. (A.18), can be neglected. Simplifying Eq. (A.18) further reduces the expression for $1/T$ to

$$\frac{1}{T} = \frac{1}{16b^2}\left\{\left[(1 + b)^2 e^{+x} - (1 - b)^2 e^{-x}\right]^2 + 4(1 - b^2)^2\sin^2d\omega\sqrt{\mu_0\epsilon''}\right\}, (A.19)$$

where $\quad b = \frac{1}{Z_0}\sqrt{\frac{\mu_0}{\epsilon'}}$

$$x = \frac{\omega d\sqrt{\mu_0\epsilon''}}{2}\tan\delta$$

$\quad d$ = sample thickness in meters.

Since $1 \gg b \gg b^2$, terms in b^2 can be neglected in Eq. (A.19), which, after still further simplification, becomes

$$\frac{1}{T} = \frac{1}{4b^2}\left\{[\sinh x + 2b\cosh x]^2 + \sin^2d\omega\sqrt{\mu_0\epsilon'}\right\} . \quad (A.20)$$

Let T_{max} be the maximum of transmission when $\omega = \omega_0$, and $\omega_{1/2}$ be the ω when $T = T_{max}/2$. Assume x , b , and ϵ' vary slowly with ω . When $\omega = \omega_0$,

$$d\omega_0\sqrt{\mu_0\epsilon''} = n\pi \qquad n = 1,2,3,4,\ldots, \quad (A.21)$$

and Eq. (A.20) becomes

$$\frac{1}{T_{max}} = \frac{1}{4b^2}\left\{[\sinh x + 2b\cosh x]^2 + \sin^2d\omega_0\sqrt{\mu_0\epsilon'}\right\} . \quad (A.22)$$

When $\omega = \omega_{1/2}$, Eq. (A.20) becomes

$$\frac{2}{T_{max}} = \frac{1}{4b^2}\left\{[\sinh x + 2b\cosh x]^2 + \sin^2d\omega_{1/2}\sqrt{\mu_0\epsilon'}\right\} . \quad (A.23)$$

Let

$$\Delta\omega = \omega_{1/2} - \omega_0 . \quad (A.24)$$

Subtracting Eq. (A.22) from Eq. (A.23), employing Eqs. (A.21) and (A.24), and simplifying, gives

$$\sin n\pi \; \frac{\Delta\omega}{\omega_0} = \frac{2[1 - (f_c/f)^2]^{1/2}}{(T_{max})^{1/2}(\kappa')^{1/2}} \; . \tag{A.25}$$

Substituting Eq. (A.21) into Eq. (A.25) and rearranging yields

$$\sin n\pi \; \frac{\Delta f}{f_0} = \frac{a}{15n} \qquad n = 1,2,3,4,\ldots, \tag{A.26}$$

where

f_0 = the frequency of the maximum of transmission, T_{max} ,

$f_{1/2}$ = the frequency at $T_{max}/2$,

Δf = $f_{1/2} - f_0$

a = $\dfrac{2[1 - (f_c'f_0)^2]^{1/2}}{(T_{max})^{1/2}} \; d' f_{0,kMc}$,

d' = sample thickness in cm,

$f_{0,kMc}$ = $f_0 \times 10^{-9}$,

f_c = cutoff frequency of the waveguide.

Equation (A.21) can now be restated as

$$(\kappa')^{1/2} = \left(\frac{\epsilon'}{\epsilon_0}\right)^{1/2} = \frac{15n}{d'f_{0,kMc}} \qquad n = 1,2,3,4,\ldots. \tag{A.27}$$

When $\omega = \omega_0$, Eq. (A.20) becomes Eq. (A.22), which can be simplified with Eqs. (A.21) and (A.27) to become

$$\frac{a}{15n} = \sinh \frac{n\pi}{2} \tan \delta + \frac{a}{15n} (T_{max})^{1/2} \cosh \frac{n\pi}{2} \tan \delta \; . \tag{A.28}$$

Equation (A.28) can be put into a form that is not transcendential by expressing the sinh and cosh terms as exponentials, simplifying, and using the quadratic form, to give

$$\exp\left(\frac{n\pi}{2} \tan \delta\right) = \frac{H + \sqrt{H^2 + 4G}}{2} \; , \tag{A.29}$$

where

$$G = \frac{1 - F}{1 + F} \; , \qquad H = \frac{2a/15n}{1 + F} \; , \qquad F = \frac{a/15n}{(1/T_{max})^{1/2}} \; .$$

As explained in the text, Eqs. (A.26) and (A.27) yield the real part of
the relative dielectric constant, κ' , from the measured data, while
Eq. (A.29) yields the loss tangent, $\tan \delta$.

APPENDIX B

DERIVATION OF INCREMENTAL BEHAVIOR OF A TUNED CAVITY

Consider a resonant cavity containing a dielectric whose dielectric constant can be changed. At a given dielectric constant, Maxwell's curl equations can be written for the volume inside the cavity as

$$\left. \begin{array}{l} \nabla \times E = - j\omega\mu H \\ \nabla \times H = j\omega\epsilon E \end{array} \right\} , \qquad\qquad (B.1)$$

where

$$\epsilon = \epsilon_1 - j\epsilon_2 .$$

Note that a notation different from that of the text is used to distinguish the real and imaginary parts of the complex dielectric constant. At a slightly different value of dielectric constant, one can write

$$\left. \begin{array}{l} \nabla \times E' = - j\omega'\mu H' \\ \nabla \times H' = j\omega'\epsilon'E' \end{array} \right\} . \qquad\qquad (B.2)$$

By vector identity,

$$\int E' \cdot (\nabla \times H)dV = \int H \cdot (\nabla \times E')dV - \int E' \times H \cdot dA , \qquad (B.3)$$

where V is the volume enclosed by the cavity and A is the surface area enclosing V. Employing Eqs. (B.1) and (B.2) in Eq. (B.3), assuming that wall losses can be neglected, and assuming that the cavity is not externally loaded, gives

$$\omega \int \epsilon E \cdot E'dV = - \omega' \int \mu H \cdot H'dV . \qquad (B.4)$$

Similarly, one obtains

$$\omega' \int \epsilon'E \cdot E'dV = - \omega \int \mu H \cdot H'dV . \qquad (B.5)$$

Combining Eqs. (B.4) and (B.5) produces

$$\left(\frac{\omega'}{\omega} \right)^2 = \frac{\int \epsilon E \cdot E'dV}{\int \epsilon'E \cdot E'dV} . \qquad (B.6)$$

- 94 -

Let

$$\omega' = \omega + \Delta\omega$$

and

$$\epsilon' = \epsilon_1' - j\epsilon_2' = (\epsilon_1 + \Delta\epsilon_1) - j(\epsilon_2 + \Delta\epsilon_2) \qquad . \qquad (B.7)$$

Substituting Eq. (B.7) into Eq. (B.6), neglecting second-order terms in Δ and assuming $\tan \delta \ll 1$, results in

$$\frac{\Delta\omega}{\omega} = -\frac{1}{2} \frac{\int \epsilon_1 E \cdot E' dV_d}{\int \epsilon_0 E \cdot E' dV_0 + \int \epsilon_1' E \cdot E' dV_d} \frac{\Delta\epsilon_1}{\epsilon_1} , \qquad (B.8)$$

where ϵ_0 is the dielectric constant of free space,

   V_0 is the volume inside the cavity but external to the dielectric,

   V_d is the volume of the dielectric.

The fields are changed very little by the incremental change in dielectric constant, $\Delta\epsilon_1$, since Eq. (B.8) can be written as

$$\frac{\Delta f}{f} = -\frac{1}{2} \frac{\omega W_1}{P_L} \frac{P_L}{\omega(W_1 + W_0)} \frac{\Delta\epsilon_1}{\epsilon_1} , \qquad (B.9)$$

where W_1 is the electrical energy stored in the dielectric
   $= \frac{1}{2} \int \epsilon_1 E \cdot E dV_d$,

   W_0 is the electrical energy stored in the electric field
   outside the dielectric $= \frac{1}{2} \int \epsilon_0 E \cdot E dV_0$,

   P_L is the total power lost and is assumed equal to the power
   lost in the dielectric.

Now the quality factor of the dielectric, Q_d , equals $(1/\tan \delta) \cong (\omega W_1/P_L)$ and the system

$$Q = \frac{\omega(W_1 + W_0)}{P_L} ;$$

hence,

$$\frac{\Delta f}{f} = -\frac{1}{2} \frac{1}{Q \tan \delta} \frac{\Delta\epsilon_1}{\epsilon_1} ,$$

or in the notation of the text,

$$\frac{\Delta f}{f} = -\frac{1}{2} \frac{1}{Q \tan \delta} \frac{\Delta\epsilon'}{\epsilon'} . \qquad (B.10)$$

It should be emphasized that here Q is the Q of the cavity when the dielectric is included.

DERIVATION OF INCREMENTAL BEHAVIOR OF PHASE SHIFTER

Consider some waveguide configuration containing a dielectric whose dielectric constant can be changed.
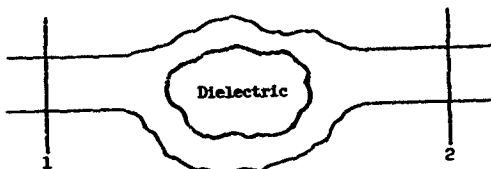
FIG. C.1--Waveguide configuration with nonlinear dielectric.

Only the dominant waveguide mode propagates at planes 1 and 2. For a given dielectric constant, Maxwell's curl equations can be written for the volume between planes 1 and 2. These are

$$\nabla \times E = - j\omega\mu H , \qquad (C.1)$$

$$\nabla \times H = j\omega\epsilon E , \qquad (C.2)$$

where

$$\epsilon = \epsilon_1 - j\epsilon_2 .$$

Note that, as in Appendix B, a notation different from that of the text is used to distinguish the real and imaginary parts of the complex dielectric constant.

At a slightly different value of dielectric constant, one can write

$$\nabla \times E' = - j\omega\mu H' , \qquad (C.3)$$

$$\nabla \times H' = j\omega\epsilon'E' . \qquad (C.4)$$

Using Eqs. (C.1) and (C.4) yields the expression

$$\int \nabla \cdot (E \times H'^*) dV = \int E \times H'^* \cdot dA = \int E \times H'^* \cdot dA_2 - \int E \times H'^* \cdot dA_1$$

$$= \int H'^* \cdot \nabla \times E \, dV - \int E \cdot \nabla \times H'^* \, dV$$

$$= \int H'^* \cdot (- j\omega\mu) H \, dV - \int E \cdot (- j\omega\epsilon'^*) E'^* \, dV , \qquad (C.5)$$

where   *   indicates the complex conjugate,

           V   is the volume enclosed between planes 1 and 2, and

           A_1 and A_2 are the areas at planes 1 and 2 respectively.

Similarly using Eqs. (C.2) and (C.3) gives

$$\int E' \times H^* \cdot dA_2 - \int E' \times H^* \cdot dA_1 = - j\omega\mu \int H^* \cdot H' dV + \int (j\omega \epsilon^*) E' \cdot E^* dV \; . \qquad (C.6)$$

For a constant input signal at plane 1, one has

$$\left. \begin{array}{l} E'(1) = E(1) \\ H'(1) = H(1) \end{array} \right\} \; . \qquad (C.7)$$

The fields at plane 2 are

$$\left. \begin{array}{l} E\,(2) = E(1)\ e^{-j\theta}\ e^{-\alpha} \\[4pt] H\,(2) = H(1)\ e^{-j\theta}\ e^{-\alpha} \\[4pt] E'(2) = E(1)\ e^{-j\theta'} e^{-\alpha'} \\[4pt] H'(2) = H(1)\ e^{-j\theta'} e^{-\alpha'} \end{array} \right\} \quad , \qquad (C.8)$$

where θ is the total phase shift between planes 1 and 2, and

           α represents total loss between planes 1 and 2.

For small changes in dielectric constant, one can write

$$\left. \begin{array}{l} \epsilon' = \epsilon + \Delta\epsilon \\[4pt] \alpha' = \alpha + \Delta\alpha \\[4pt] \theta' = \theta + \Delta\theta \end{array} \right\} \quad , \qquad (C.9)$$

and

$$\left. \begin{array}{l} E' = E + \Delta E \\[4pt] H' = H + \Delta H \end{array} \right\} \quad . \qquad (C.10)$$

In this analysis only the first-order incremental terms are included. From Eqs. (C.8) and (C.9) one obtains

$$\int E \times H'^* \cdot dA_2 - \int E \times H'^* \cdot dA_1 = \left[e^{j\Delta\theta} e^{-2\gamma} e^{-\Delta\alpha} - 1 \right] \int E(1) \times H(1)^* \cdot dA_1 \; . \qquad (C.11)$$

Similarly, one can obtain

$$\int E' \times H^* \cdot dA_2 - \int E' \times H^* \cdot dA_1 = \left[e^{-j\Delta\theta} e^{-2\alpha} e^{-\Delta\alpha} - 1 \right] \int E(1) \times H(1)^* \cdot dA_1 \; . \qquad (C.12)$$

- 97 -

Subtracting Eq. (C.12) from (C.11) and employing Eqs. (C.5) and (C.6),

$$\left[e^{j\Delta\theta} - e^{-j\Delta\theta}\right]e^{-2\alpha}e^{-\Delta\alpha}\int E(1) \times H(1)^*\cdot dA_1 = -j\omega\mu\int(H'^*\cdot H - H'\cdot H^*)dV$$

$$+ \int(j\omega\epsilon^*)(E'^*\cdot E - E'\cdot E^*)dV + j\omega(\Delta\epsilon)^* \int E\cdot E'^* dV_d , \qquad (C.13)$$

where the last integral is taken over the volume of the dielectric since $\Delta\epsilon$ exists only within the dielectric. Substituting Eq. (C.10) into Eq. (C.13) and equating the imaginary terms while assuming $\Delta\theta$ and $\Delta\alpha$ small gives

$$2\Delta\theta e^{-2\alpha} \text{ Re}\left\{\int E \times H^*\cdot dA_1\right\}$$

$$= \omega \frac{\Delta\epsilon_1}{\epsilon_1}\int\epsilon_1|E|^2 dV_d \left[1 + \frac{2 \tan \delta \text{ Im}\left\{\int(\Delta E/E)\epsilon_1|E|^2 dV_d\right\}}{(\Delta\epsilon_1/\epsilon_1)\int\epsilon_1|E|^2 dV_d}\right], \quad (C.14)$$

where $\text{Re}\{\ \}$ means "real part of $\{\ \}$ ",
$\text{Im}\{\ \}$ means "imaginary part of $\{\ \}$ ", and
$\tan \delta = \epsilon_2/\epsilon_1$.

Now $\tan \delta < .1$ and if the insertion loss is low, Eq. (C.14) reduces to

$$2\Delta\theta e^{-2\alpha} \text{ Re}\left\{\int E \times H^*\cdot dA_1\right\} \cong \omega \frac{\Delta\epsilon_1}{\epsilon_1} \int\epsilon_1|E|^2 dV_d . \qquad (C.15)$$

To evaluate the right-hand side of Eq. (C.15), use

$$\int \nabla \cdot E \times H^* dV = \int E \times H^*\cdot dA_2 - \int E \times H^*\cdot dA_1 . \qquad (C.16)$$

Substituting Eqs. (C.1) and (C.8) into Eq. (C.16) and equating the real parts yields

$$\int\epsilon_1|E|^2 dV_d = -\frac{\epsilon_1}{\omega\epsilon_2} (e^{-2\alpha} - 1) \text{ Re}\left\{\int E \times H^*\cdot dA_1\right\} . \qquad (C.17)$$

Using Eq. (C.17), Eq. (C.15) becomes

$$\Delta\theta = \frac{1}{2} \frac{(e^{2\alpha} - 1)}{\tan \delta} \frac{\Delta\epsilon_1}{\epsilon_1} . \qquad (C.18)$$

- 98 -

Assuming a matched system, it is possible to write

$$e^{2\alpha} = \frac{P_{in}}{P_{out}} \qquad (C.19)$$

where P_{in} is the power incident at plane 1,

         P_{out} is the power at plane 2.

Hence, the incremental phase shift is

$$\Delta\theta = \frac{1}{2 \tan \delta} \frac{P_{lost}}{P_{out}} \frac{\Delta\epsilon_1}{\epsilon_1} \; ,$$

or in the notation of the text

$$\Delta\theta = \frac{1}{2 \tan \delta} \frac{P_{lost}}{P_{out}} \frac{\Delta\epsilon'}{\epsilon'} \qquad (C.20)$$

- 99 -

DERIVATION OF METHOD TO MEASURE DIELECTRIC CONSTANT

USING RESONANT INTERFEROMETER

The geometry of the interferometer is shown in Figure D.1.
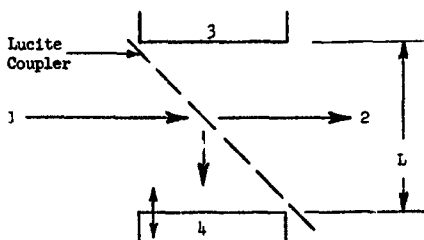
FIG. D.1--Schematic diagram of interferometer.

The monochromatic plane wave enters at 1, and after being partially
reflected by the lucite coupler placed at 45° to its direction of propag-
ation, exits at 2. Two flat aluminum reflectors are labeled 3 and 4--
3 being fixed and 4 movable. Let the following terms be defined as

S_{12} = complex scattering coefficient from 1 to 2,

Γ_3 , Γ_4 = reflection coefficients of reflectors 3 and 4
respectively,

L = distance between the reflectors,

t = transmission coefficient of the lucite coupler,

$j\gamma$ = reflection coefficient of the lucite coupler,

$\alpha + j\beta$ = complex propagation constant of the wave where α
represents the losses suffered by the wave, such
as diffraction loss and dielectric loss in air and
is not necessarily independent of L .

From Fig. B.1, the scattering coefficient, S_{12}, can be written as

$$S_{12} = t + \left[(jr)^2 \Gamma_k \, tr_3 \, e^{-2(\alpha+j\beta)L} \right.$$

$$\left. + (jr)^2 \Gamma_k \, tr_3 \, e^{-2(\alpha+j\beta)L} \; tr_3 \, tr_3 \, e^{-2(\alpha+j\beta)L} + \dots \right], \quad (D.1)$$

or

$$S_{12} = t - r^2 \Gamma_3 \Gamma_k \, t e^{-2(\alpha+j\beta)L} \left\{ 1 + r \Gamma_3 \Gamma_k \, t^2 e^{-2(\alpha+j\beta)L} \right.$$

$$\left. + \left[\Gamma_3 \Gamma_k \, t^2 e^{-2(\alpha+j\beta)L} \right]^2 + \dots \right\} . \quad (D.2)$$

Equation (D.2) can be reduced to

$$S_{12} = t \left[\frac{1 - (t^2 + r^2) \Gamma_3 \Gamma_k \, e^{-2(\alpha+j\beta)L}}{1 - \Gamma_3 \Gamma_k \, t^2 e^{-2(\alpha+j\beta)L}} \right] . \quad (D.3)$$

Let L_m be the distance between the reflectors that makes $|S_{12}|$ a minimum. For the aluminum reflectors, L_m is

$$L_m = \frac{m\lambda}{2} \qquad m = 1,2,3,\dots, \quad (D.4)$$

since the phase angle of Γ_3 and $\Gamma_k = 0$. Figure D.2 shows the behavior of $|S_{12}|$ as a function of L.

Define a length δ for which

$$\left| S_{12} \left(L_m \pm \frac{\delta}{2} \right) \right|^2 = \frac{1}{2} \left\{ |S_{12}|^2_{max} + |S_{12}|^2_{min} \right\} , \quad (D.5)$$

where $\quad |S_{12}|_{min} = |S_{12}(L_m)|$

$\quad |S_{12}|_{max} = |S_{12}(L_{max})|$ is S_{12} when the interferometer is far off resonance.

Using Eq. (D.3) in Eq. (D.5) and simplifying, one finds

$$2 \left| \frac{1 - (t^2 + r^2) |\Gamma_3 \Gamma_k| \exp(-2\alpha L_m) \exp(-j\beta\delta)}{1 - t^2 |\Gamma_3 \Gamma_k| \exp(-2\alpha L_m) \exp(-j\beta\delta)} \right|^2$$

$$= \left[\frac{1 + (t^2 + r^2) |\Gamma_3 \Gamma_k| \exp(-2\alpha L_{max})}{1 + t^2 |\Gamma_3 \Gamma_k| \exp(-2\alpha L_{max})} \right]^2 + \left[\frac{1 - (t^2 + r^2) |\Gamma_3 \Gamma_k| \exp(-2\alpha L_m)}{1 - t^2 |\Gamma_3 \Gamma_k| \exp(-2\alpha L_m)} \right]^2$$

$$(D.6)$$
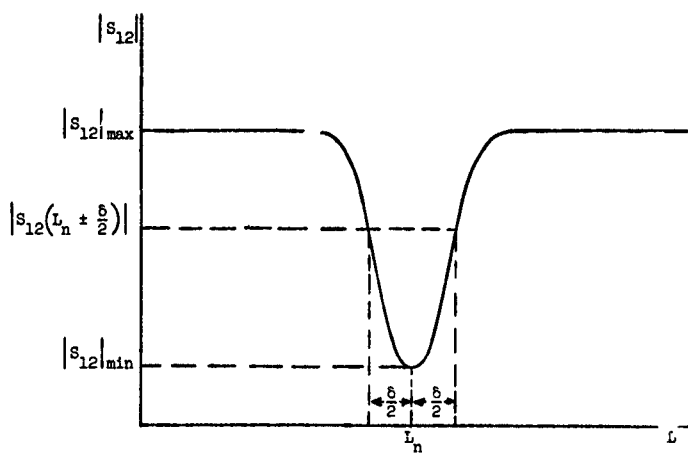
FIG. D.2--Magnitude of transfer scattering coefficient
of interferometer as a function of tne dis-
tance, L , between the reflectors.

where $\quad \arg \Gamma_3 + \arg \Gamma_4 - 2\beta L_n = 0$,

$\qquad \arg \Gamma_3 + \arg \Gamma_4 - 2\beta L_{max} = \pi$, and

$e^{-2\alpha\delta} = 1$ is assumed.

For simplicity define the following:

$$S \triangleq |S_{12}|_{max} = t \left[\frac{1 + (t^2 + \gamma^2)|\Gamma_3\Gamma_4|\exp(-2\alpha L_{max})}{1 + t^2|\Gamma_3\Gamma_4|\exp(-2\alpha L_{max})} \right] \qquad (D.7)$$

$$d \triangleq \frac{|S_{12}|_{min}}{|S_{12}|_{max}} = \frac{t}{S} \left[\frac{1 - (t^2 + \gamma^2)|\Gamma_3\Gamma_4|\exp(-2\alpha L_n)}{1 - t^2|\Gamma_3\Gamma_4|\exp(-2\alpha L_n)} \right] \qquad (D.8)$$

$$\theta \triangleq \beta\delta = \frac{2\pi\delta}{\lambda} . \qquad (D.9)$$

Substituting Eqs. (D.7), (D.8), and (D.9) into Eq. (D.6) and using the law of cosines gives

$$\left\{ \frac{1 + \left[(t^2 + \gamma^2)|\Gamma_3\Gamma_4|\exp(-2\alpha L_n) \right]^2 - 2\left[(t^2 + \gamma^2)|\Gamma_3\Gamma_4|\exp(-2\alpha L_n) \right]\cos\theta}{1 + \left[t^2|\Gamma_3\Gamma_4|\exp(-2\alpha L_n) \right]^2 - 2\left[t^2|\Gamma_3\Gamma_4|\exp(-2\alpha L_n) \right]\cos\theta} \right\}$$

$$= \frac{S^2}{2t^2}(1 + d^2) , \qquad (D.10)$$

or by using a half-angle formula, Eq. (D.10) becomes

$$\left\{ \frac{\left[1 - (t^2 + \gamma^2)|\Gamma_3\Gamma_4|\exp(-2\alpha L_n) \right]^2 + 4(t^2 + \gamma^2)|\Gamma_3\Gamma_4|\exp(-2\alpha L_n)\sin^2(\theta/2)}{\left[1 - t^2|\Gamma_3\Gamma_4|\exp(-2\alpha L_n) \right]^2 + 4t^2|\Gamma_3\Gamma_4|\exp(-2\alpha L_n)\sin^2(\theta/2)} \right\}$$

$$= \frac{S^2}{2t^2}(1 + d^2) . \qquad (D.11)$$

Solving Eq. (D.11) for $4\sin^2(\theta/2)$ yields

$$4\sin^2\frac{\theta}{2}$$

$$= \frac{\left\{ \frac{S^2}{2t^2}(1 + d^2) - \frac{\left[1 - (t^2 + \gamma^2)|\Gamma_3\Gamma_4|\exp(-2\alpha L_n) \right]^2}{\left[1 - t^2|\Gamma_3\Gamma_4|\exp(-2\alpha L_n) \right]^2} \right\} \left[1 - t^2|\Gamma_3\Gamma_4|\exp(-2\alpha L_n) \right]^2}{|\Gamma_3\Gamma_4|\exp(-2\alpha L_n)\left[(t^2 + \gamma^2) - \frac{S^2}{2}(1 + d^2) \right]} . \qquad (D.12)$$

- 103 -

Substituting Eq. (D.8) into Eq. (D.12) gives

$$4 \sin^2 \frac{\theta}{2} = \frac{(s^2/t^2)(1 - d^2)\left[1 - t^2 |\Gamma_3 \Gamma_4| \exp(-2\alpha L_n)\right]^2}{|\Gamma_3 \Gamma_4| \exp(-2\alpha L_n)\left[2(t^2 + \gamma^2) - s^2(1 + d^2)\right]} \quad . \qquad (D.13)$$

The loss suffered by a wave, when making a complete traverse between the reflectors and when $L = L_n$, is very nearly the same as when $L = L_{max}$; therefore

$$\tau^2 \triangleq \exp(-2\alpha L_n) \approx \exp(-2\alpha L_{max}) \quad . \qquad (D.14)$$

And for convenience, the following can be defined as

$$\sigma^2 \triangleq (t^2 + \gamma^2) \qquad (D.15)$$

$$a^2 \triangleq \sigma^2 - s^2 \quad . \qquad (D.16)$$

Using Eqs. (D.8), (D.14), (D.15), and (D.16), and simplifying, Eq. (D.13) finally becomes

$$4 \sin^2 \frac{\theta}{2} = \frac{\left[1 - \sigma^2 \tau^2 |\Gamma_3 \Gamma_4|\right]^2}{\tau^2 |\Gamma_3 \Gamma_4|} \cdot \frac{1}{d^2 \left[\sigma^2 + s^2 (1 + d^2)/(1 - d^2)\right]} \quad . \qquad (D.17)$$

Now replace the aluminum reflector at 3 in Fig. D.1 with a dielectric reflector that has the same shape and has a thickness which is electrically infinite. Let the reflection coefficient of the dielectric face be Γ. It can be assumed that $\Gamma_4 = 1$. Using these definitions and Eq. (D.14), Eq. (D.8), for the case of the dielectric reflector, becomes

$$d_1 = \frac{1 - \sigma^2 \tau^2 |\Gamma|}{1 - t^2 \tau^2 |\Gamma|} \cdot \frac{1 + t^2 \tau^2 |\Gamma|}{1 + \sigma^2 \tau^2 |\Gamma|} \quad . \qquad (D.18)$$

When both reflectors are aluminum, it can be assumed $\Gamma_3 = \Gamma_4 = 1$; hence in this case, Eq. (D.8) is

$$d_0 = \frac{1 - \sigma^2 \tau^2}{1 - t^2 \tau^2} \cdot \frac{1 + t^2 \tau^2}{1 - \sigma^2 \tau^2} \quad . \qquad (D.19)$$

For convenience, ψ_0' can be defined as

$$\psi_0' \triangleq 2 \sin \frac{\theta_0}{2} \sqrt{\sigma^2 + s_0^2 \frac{(1 + d_0^2)}{(1 - d_0^2)}} \quad , \qquad (D.20)$$

where the zero subscript indicates that a quantity is defined for the case in which both reflectors are aluminum. With Eqs. (D.19) and (D.20), Eq. (D.17) becomes

$$\psi_0' d_0 = \frac{1 - \sigma^2 \tau^2}{\tau} . \tag{D.21}$$

With the above preliminary work, it is now possible to solve for the index of refraction of the dielectric in terms of the measurable experimental quantities, d_0 , d_1 , δ_0 , and θ_0 by using Eqs. (D.18), (D.19), and (D.21). The index of refraction is

$$n = \frac{1 + |\Gamma|}{1 - |\Gamma|} \tag{D.22}$$

where $|\Gamma|$ is the negative of the reflection coefficient of the dielectric.

Rearranging Eq. (D.18) yields

$$|\Gamma| = \frac{\dfrac{1 + t^2 \tau^2 |\Gamma|}{1 + \sigma^2 \tau^2 |\Gamma|} - d_1}{\tau^2 \left[\sigma^2 \dfrac{1 + t^2 \tau^2 |\Gamma|}{1 + \sigma^2 \tau^2 |\Gamma|} - t^2 d_1 \right]} . \tag{D.23}$$

Substituting Eq. (D.23) into Eq. (D.22) yields

$$n = \frac{(1 + \sigma^2 \tau^2) \left(\dfrac{1 + t^2 \tau^2 |\Gamma|}{1 + \sigma^2 \tau^2 |\Gamma|} \right) - d_1 (1 + t^2 \tau^2)}{d_1 (1 - t^2 \tau^2) - (1 - \sigma^2 \tau^2) \left(\dfrac{1 + t^2 \tau^2 |\Gamma|}{1 + \sigma^2 \tau^2 |\Gamma|} \right)} , \tag{D.24}$$

but from Eq. (D.21), one finds that

$$1 - \sigma^2 \tau^2 = \psi_0' d_0 \tau , \tag{D.25}$$

and from Eq. (D.19),

$$1 - t^2 \tau^2 = \frac{1 - z^2 \tau^2}{d_0} \frac{1 + t^2 \tau^2}{1 + \sigma^2 \tau^2} , \tag{D.26}$$

or, using Eq. (D.25), Eq. (D.26) becomes

$$1 - \sigma^2 \tau^2 = \psi_0'' \pi \frac{1 + t^2 \tau^2}{1 + \sigma^2 \tau^2} .$$ (D.27)

Substituting Eq. (D.25) and (D.27) into Eq. (D.24) and simplifying gives

$$m = \frac{1 + \sigma^2 \tau^2}{\psi_0'' \pi} \left[\frac{1 - \Phi_1 \left(\dfrac{1 + t^2 \tau^2}{1 + t^2 \tau^2 |\Gamma|} \right) \left(\dfrac{1 + \sigma^2 \tau^2 |\Gamma|}{1 + \sigma^2 \tau^2} \right)}{\Phi_1 \left(\dfrac{1 + t^2 \tau^2}{1 + t^2 \tau^2 |\Gamma|} \right) \left(\dfrac{1 + \sigma^2 \tau^2 |\Gamma|}{1 + \sigma^2 \tau^2} \right) - \Phi_0} \right] .$$ (D.28)

Except for the last two pages of Appendix D, the balance of this derivation is devoted to reducing Eq. (D.28) to a relatively simple equation by using suitable approximations. The resulting expression for m, together with a more approximate expression for m derived in the text, was used to calculate the dielectric constant of the nonlinear ceramic.

To investigate the factors multiplying Φ_1 in Eq. (D.28), one can define

$$\Phi_1 \triangleq \Phi_1 \left(\frac{1 + t^2 \tau^2}{1 + t^2 \tau^2 |\Gamma|} \right) \left(\frac{1 + \sigma^2 \tau^2 |\Gamma|}{1 + \sigma^2 \tau^2} \right) .$$ (D.29)

Adding and subtracting Φ_1 to the right-hand side of Eq. (D.29) yields

$$\Phi_1 = \Phi_1 \left[1 - \frac{\tau^2 (\sigma^2 - t^2)(1 - |\Gamma|)}{(1 + \sigma^2 \tau^2)(1 + t^2 \tau^2 |\Gamma|)} \right] .$$ (D.30)

The transmission coefficient of the lucite coupler is close to unity, and the losses suffered by a wave in a single traverse between the two reflectors is small. Furthermore, the index of refraction of the dielectric is high. Hence, the following assumptions can be made:

$$1 - t^2 \ll 1$$ (D.31)

$$1 - \sigma^2 \tau^2 \ll 1$$ (D.32)

$$\frac{1}{n} \ll 1 .$$ (D.33)

Equation (D.25) can be rewritten as

$$\sigma^2 \tau^2 = 1 - \psi_0' \Phi_0 \pi ,$$ (D.34)

and using the assumption of Eq. (D.32) gives

$$\tau \simeq \frac{1}{\sigma} \left(1 - \frac{\psi_0' d_0 \tau}{2} \right) . \tag{D.35}$$

With Eqs. (D.31) and (D.32), Eq. (D.27) becomes

$$t^2 \tau^2 = 1 - \psi_0' \tau \left(\frac{1 + t^2 \tau^2}{1 + \sigma^2 \tau^2} \right) \simeq 1 - \psi_0' \tau , \tag{D.36}$$

or

$$\tau(\sigma^2 - t^2) \simeq \frac{1}{\tau} (\sigma^2 \tau^2 - 1 + \psi_0' \tau) . \tag{D.37}$$

Using Eq. (D.34) in Eq. (D.37) yields

$$\tau(\sigma^2 - t^2) \simeq \psi_0'(1 - d_0) . \tag{D.38}$$

Using Eq. (D.33) in Eq. (D.22) gives

$$|\Gamma| = \frac{n - 1}{n + 1} \simeq 1 - \frac{2}{n} , \tag{D.39}$$

or

$$1 - |\Gamma| = \frac{2}{n} . \tag{D.40}$$

Now with Eqs. (D.34), (D.35), (D.36), (D.38), (D.39), and (D.40), Eq. (D.30) can be reduced to

$$D_1 \simeq d_1 \left\{ 1 - \frac{(\psi_0'/\sigma)\left[1 - (\psi_0' d_0 \tau/2)\right](1 - d_0)(2/n)}{(2 - \psi_0' d_0 \tau)\left[1 + (1 - \psi_0' \tau)(1 - 2/n)\right]} \right\} . \tag{D.41}$$

Equation (D.41) can be further reduced by using Eqs. (D.33) and (D.35) and neglecting the term in $\psi_0'^2$ to give

$$D_1 \simeq d_1 \left\{ 1 - \frac{\psi_0'(1 - d_0)}{2\sigma n \left[1 - (\psi_0'/2\sigma)\right]} \right\} . \tag{D.42}$$

The term s_0^2 appears in the definition of ψ_0', Eq. (D.20), and should also be investigated. Equation (D.16) defines s_0^2 as

$$s_0^2 = \sigma^2 - S_0^2 = \sigma^2 - t^2 \frac{(1 + \sigma^2 \tau^2)^2}{(1 + t^2 \tau^2)^2} = \frac{(\sigma^2 - t^2)(1 - \sigma^2 t^2 \tau^4)}{(1 + t^2 \tau^2)^2} . \tag{D.43}$$

- 107 -

From Eq. (D.36) one obtains

$$(\sigma^2 - t^2) \simeq \frac{\psi_0'}{\tau} (1 - d_0) , \tag{D.44}$$

and from Eqs. (D.34) and (D.36),

$$(1 - \sigma^2 t^2 \tau^4) \simeq \psi_0' \tau (1 + d_0) , \tag{D.45}$$

where the term in $\psi_0'^2$ has been neglected. Rearranging Eq. (D.36) gives

$$(1 + t^2 \tau^2) = \frac{(1 - t^2 \tau^2)(1 + \sigma^2 \tau^2)}{\psi_0' \tau} , \tag{D.46}$$

and

$$1 - t^2 \tau^2 \simeq - \psi_0' \tau . \tag{D.47}$$

Substituting Eq. (D.47) into Eq. (D.46), using Eqs. (D.34) and (D.35), and neglecting the term in $\psi_0'^2$ yields

$$(1 + t^2 \tau^2)^{-2} \simeq \frac{1}{\left[2 - (\psi_0' d_0 / \sigma)\right]} \simeq \frac{1}{4} \left(1 + \frac{\psi_0' d_0}{\sigma}\right) . \tag{D.48}$$

Substituting Eqs. (D.44), (D.45) and (D.48) into Eq. (D.43) gives

$$s_0^2 = \frac{\psi_0'^2 \left[1 + (\psi_0' d_0 / \sigma)\right]}{4} (1 - d_0^2) . \tag{D.49}$$

To first order, $\psi_0' \approx \sigma \theta_0$; therefore, substituting Eq. (D.49) into Eq. (D.20) yields

$$\psi_0' \simeq 2 \sin \frac{\sigma \theta_0}{2} \sqrt{1 + \frac{\theta_0^2 (1 + \theta_0 d_0)(1 + d_0^2)}{4}} . \tag{D.50}$$

The term $(1 + \sigma^2 \tau^2)/\tau$ in Eq. (D.28) can be evaluated with Eqs. (D.34) and (D.35) as

$$\frac{1 + \sigma^2 \tau^2}{\tau} = \frac{2 - \psi_0' d_0 \tau}{(1/2\sigma)(2 - \psi_0' d_0 \tau)} = 2\sigma . \tag{D.51}$$

- 108 -

Substituting Eqs. (D.29) and (D.51) into Eq. (D.28) yields

$$n \simeq \frac{2\sigma}{\psi_0'} \left(\frac{1 - D_1}{D_1 - d_0} \right) , \qquad (D.52)$$

where these terms are defined by Eqs. (D.50), (D.42), (D.9), (D.15), respectively,

$$\psi_0' \simeq 2 \sin \frac{\sigma\theta_0}{2} \sqrt{1 + \frac{\theta_0^2(1 + \theta_0 d_0)(1 + d_0^2)}{4}} ,$$

$$D_1 \simeq d_1 \left\{ 1 - \frac{\psi_0'(1 - d_0)}{2\sigma n\left[1 - (\psi_0'/2\sigma) \right]} \right\} ,$$

$$\theta_0 = \frac{2\pi\delta_0}{\lambda} ,$$

and

$$\sigma^2 = (t^2 + \gamma^2) .$$

Now θ_0 is small and σ is close to unity, hence, Eq. (D.50) can be written as

$$\psi_0' \sim 2\sigma \sin \frac{\theta_0}{2} \sqrt{1 + \frac{\theta_0^2(1 + \theta_0 d_0)(1 + d_0^2)}{4}} , \qquad (D.53)$$

and Eq. (D.42) can be written as

$$D_1 \simeq d_1 \left[1 - \frac{\psi_0'}{2\sigma n} (1 - d_0) \right] . \qquad (D.54)$$

With Eqs. (D.53) and (D.54), Eq. (D.52) can be finally written as

$$n \simeq \frac{1}{\psi_0} \left(\frac{1 - D_1}{D_1 - d_0} \right) , \qquad (D.55)$$

where   n = index of refraction,

$$\psi_0 = \frac{\psi_0'}{2\sigma} \simeq \sin \frac{\theta_0}{2} \sqrt{1 + \frac{\theta_0^2(1 + \theta_0 d_0)(1 + d_0^2)}{4}} ,$$

$$D_1 \simeq d_1 \left[1 - \frac{\psi_0}{n} (1 - d_0) \right] ,$$

and

$$\theta_0 = \frac{2\pi\delta_0}{\lambda} .$$

An expression for the loss tangent, $\tan \delta$, of the dielectric will now be obtained. The complex index of refraction is defined as

$$n^* = n(1 - jk) , \tag{D.56}$$

where k is the index of absorption. Von Hippel[14] gives $\tan \delta$ in terms of k as

$$\tan \delta = \frac{2k}{1 - k^2} ,$$

which, for small k , reduces to

$$\tan \delta \simeq 2k . \tag{D.57}$$

When rationalized, the reflection coefficient of the dielectric reflector becomes

$$\Gamma = \frac{n^* - 1}{n^* + 1} = \frac{(n^2 + k^2 - 1) - j2nk}{(n + 1)^2 + n^2 k^2} . \tag{D.58}$$

With Eq. (D.57), the argument of Γ is

$$\arg \Gamma \simeq \arctan \frac{\tan \delta}{n\left[1 + (\tan^2 \delta/4) \right]} \approx \frac{\tan \delta}{n} . \tag{D.59}$$

Now when the aluminum stationary reflector is used and when the interferometer is resonant (i.e., $L = L_n$), a wave undergoes a phase shift of 2π when making a complete traverse of the interferometer from 4 to 3 and back to 4, in Fig. D.1, or

$$2\beta L_n + \phi = 2n\pi \qquad n = 1,2,3,\ldots, \tag{D.60}$$

where ϕ is the phase shift suffered in the lucite coupler. However, when the dielectric stationary reflector is used, the wave undergoes additional phase shift when reflected at 3; hence the total phase shift

- 110 -

is given by

$$2\beta L_n' + \phi + \arg \Gamma = 2n\pi \qquad n = 1,2,3,\ldots, \qquad (D.61)$$

where L_n' is the resonant spacing with the dielectric reflector.
Subtracting Eq. (D.61) from Eq. (D.60) yields

$$2\beta\Delta L - \arg \Gamma = 0 , \qquad (D.62)$$

where

$$\Delta L = L_n - L_n' .$$

Using Eq. (D.59), Eq. (D.62) becomes

$$\tan \delta = 2n \left(\frac{2\pi\Delta L}{\lambda} \right) \qquad (D.63)$$

where $\beta = 2\pi/\lambda$,

   n = real part of the complex index of refraction.

APPENDIX E

ASSEMBLY OF CAVITY USED IN LARGE-SIGNAL MEASUREMENTS

An exploded-view photograph of the parts as they fit into the cavity is shown in Fig. 30. A photograph of the assembled cavity holder is shown in Fig. 29. In the description of the method of assembly, all letter references are made to Fig. 30.

Before assembly, all parts should be carefully cleaned. The coupling loops should be inspected under a microscope to insure that the end of the insulation is free of all dirt which could provide an arc path. The dielectric post is cleaned with Versene as described on page 15 of Chapter II, and then inspected under a microscope to make sure that the metal deposited on the ends of the post is still intact.

First the two gaskets, shown in Fig. 27b, are put on the lower end of the cavity, a , with high-temperature grease. They are made from a 0.002" sheet of polyethylene and serve to stop the SF_6 from bypassing the cavity. The dielectric post is put on the end of the center conductor and the cavity lowered into the hole bored in the center of the holder. The locking pins, b , are then screwed in so that their ends fall onto the flats milled in the side of the cavity. This not only holds the cavity in place but also insures that the holes in the side of the cavity are aligned with the holes in the locking pins through which the coaxial lines with their coupling loops will be inserted. Next the beryllium copper disk, c , is stuck to the end of a glass rod with a small amount of rubber cement and lowered gently into place on top of the cavity with care being taken not to dislodge the dielectric post. When the disk is in place, the glass rod is moved sideways to free it and removed. The set pin, d , can now be screwed down until it forces the disk down onto the cavity and also seals the gaskets on the lower end of the cavity. The coaxial lines with the coupling loops, e , are then inserted through the locking pins and cavity wall so that the plane of the loops is vertical. The tension pin, f , is screwed into the set pin, d , but not far enough to touch the disk, c . Finally the whole assembly is connected into a transmission measurement setup and brought to operating temperature in order to set the tension on the disk and maximize the coupling. The

measurement setup differs from that of Fig. 2 only in that 3-band instead
of X-band equipment is used and that the 10 db output coupler is replaced
by a 10 db pad between the 20 db coupler and the holder. The crystal that
measures the transmission is put directly on the output of the cavity.
While watching the transmission trace on the oscilloscope, the tension
pin, f, is very slowly screwed down. When the resonance curve has
reached its maximum amplitude without shifting the resonant frequency,
the correct setting has been found, since the disk will now be making
good contact with the metalized end of the dielectric post. The coupling
is then maximized by changing the orientation and depth of penetration of
the loops.

DETERMINATION OF FIELD CURVATURE IN CERAMIC SAMPLE

In Chapter IV the electric field intensity across the ceramic sample is assumed to be a constant. To estimate the validity of this assumption, the wave equation can be solved for the region in the dielectric where the cylindrical coordinate system is that of Fig. F.1.
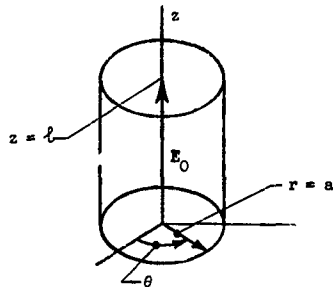
FIG. F.1--Coordinate system for cylindrical post
of nonlinear dielectric.

Since the length of the sample, ℓ, is small compared to the free space wavelength in the transmission line of the cavity, the electric field can be assumed constant in the z-direction. Let E_0 be the electric field intensity at $r = 0$. The wave equation is

$$\nabla_T^2 E_z = - k_c^2 E_z , \qquad (F.1)$$

where ∇_T^2 is the Laplacian operator taken with respect to he
transverse coordinates,
$k_c^2 = \gamma^2 + k^2$
γ = propagation constant in the z-direction
$k^2 = \omega^2 \mu_0 \epsilon$

There are no variations of E_z with θ. There is no propagation in the z-direction, therefore $\gamma = 0$. Since $\tan \delta \ll 1$, the dielectric constant can be assumed to be

$$\epsilon = \epsilon' = \epsilon_0 k' ;$$

hence Eq. (F.1) in cylindrical coordinates reduces to Bessel's equation, which is

$$\frac{\partial^2 E_z}{\partial r^2} + \frac{1}{r}\frac{\partial E_z}{\partial r} + \omega^2 \mu_0 \epsilon_0 k' E_z = 0 , \tag{F.2}$$

for which the solution is

$$E_z = E_0 J_0(\omega\sqrt{\mu_0 \epsilon_0 k'}\ r) . \tag{F.3}$$

Equation (F.3) can now be evaluated at $r = a$ and $r = (2/3)a$. At $r = a$, E_z is

$$E_z = 0.967\ E_0 ,$$

and at $r = (2/3)a$, it is

$$E_z = 0.985\ E_0 ;$$

hence a negligible error (i.e., less than 2%) is introduced by assuming E_z to be a constant from $r = 0$ to $r = a$.

REFERENCES

1. E. T. Jaynes and V Varenhorst, "Measurement of the Dielectric Constant of Single-Crystal BaTiO$_3$ at Microwave Frequencies," Microwave Laboratory Report No. 287, Stanford University (1955).

2. J. G. Powles and W. Jackson, "The Measurement of the Dielectric Properties of High-Permittivity Materials at Centimetre Wavelengths," Proc. Inst. Elect. Engr. (London) 96, Part III, 383-389 (1949).

3. H. J. Schmitt, "Dielectric Constant of Barium Titanate at 10 kMc," Z. angew. Physik 9, 107-111 (1957).

4. L. Davis and L. G. Rubin, "Some Dielectric Properties of Barium-Strontium Titanate Ceramics at 3000 Megacycles," J. Appl. Phys. 24, 1194-1197 (1953).

5. C. B. Sharpe and C. G. Brockus, "Investigations of Microwave Properties of Ferroelectric Materials (Final Report)," University of Michigan Research Institute, Report No. 2732-4-F (1959).

6. A. von Hippel, Dielectric Materials and Applications, The Technology Press of M.I.T. (John Wiley and Sons, Inc., New York, 1954), pp. 47-73.

7. C. G. Montgomery, Technique of Microwave Measurements, M.I.T. Radiation Laboratory Series #11 (McGraw-Hill Book Company, New York, 1947), pp. 561-676.

8. W. J. Gemulla and R. D. Hall, "Ferroelectrics at Microwave Frequencies," Microwave Journal 3, 47-51 (1960).

9. H. Diamond, "On the Polarization Microwave Dispersion and Loss in High Permittivity Ferroelectrics," (Ph.D. dissertation, University of Michigan, 1959).

10. F. Reggia and E. G. Spencer, "A New Technique in Ferrite Phase Shifting for Beam Scanning of Microwave Antennas," Proc. IRE 45, 1510-1517 (1957).

11. R. H. Hardin, E. J. Downey, and J. Munushian, "Electronically-Variable Phase Shifters Utilizing Variable Capacitance Diodes," Proc. IRE 48, 944-945 (1960).

12. R. M. Miller, "The Design and Use of a Linear Electron Accelerator for Submillimeter Wave Generation," (unpublished Ph.D. dissertation, Stanford University, 1961).

13. P. A. Szente, "Submillimeter Wave Generation with Relativistic Electron Beams," (unpublished Ph.D. dissertation, Stanford University, 1961).

14. A. von Hippel, Dielectrics and Waves, (John Wiley and Sons, Inc., New York, 1954).

15. K. Klotter, "Nonlinear Vibration Problems Treated by the Averaging Methods of W. Ritz," Technical Report No. 17, Part II, Contract N6onr-215, Task Order 2, Division of Engr. Mech., Stanford University, (1951).

16. Y. H. Ku, Analysis and Control of Nonlinear Systems, (Roland Press Company. New York, 1958).

17. J. J. Stoker. Nonlinear Vibrations, (Interscience Publishers, Inc., New York, 1950), pp. 85-86.

18. N. Marcuvitz, Waveguide Handbook, M.I.T. Radiation Laboratory Series #10 (McGraw-Hill Book Company, New York, 1947), p. 176.

19. E. L. Ginzton, Microwave Measurements, (McGraw-Hill Book Company, New York, 1957), pp. 391-434.

20. E. L Ginzton, Microwave Measurements, (McGraw-Hill Book Company, New York, 1957), p. 223.

21. N. W. McLachlan, Ordinary Non-linear Differential Equations in Engineering and Physical Sciences, (Oxford University Press, Glasgow, 1950).

22. S. Ramo and J. R. Whinnery, Fields and Waves in Modern Radio, 2d ed., (John Wiley and Sons, Inc., New York, 1953), pp. 266-370.

23. H. Margenau and G. M. Murphy, The Mathematics of Physics and Chemistry, 2d ed., (D. Van Nostrand Company, Inc., New York, 1957).

24. C. J. Trantor, Integral Transforms in Mathematical Physics, Methuen's Monographs on Physical Subjects, (John Wiley and Sons, Inc., New York, 1956), pp. 88-93.

INTRODUCTORY MATERIAL

A. von Hippel, Dielectrics and Waves, (John Wiley and Sons, Inc., New York, 1954).

E. T. Jaynes, "Nonlinear Dielectric Materials," Proc. IRE 43, 1733-1737 (1955).

G. Shirane, F. Jona, and R. Pepinsky, "Some Aspects of Ferroelectricity," Proc. IRE $\underline{43}$, 1738-1793 (1955).

An extensive bibliography has been compiled by Hall:

R. Hall, "Bibliography on Ferroelectrics," Sylvania Electronic Defense Laboratory Report No. EDL-M165 (January 1959). (This report is available from ASTIA.)

GOVERNMENTAL

Agency	cc	Agency	cc
Commander AF Office of Scientific Research Washington 25, D.C. Attn: SRY	3	Armed Services Technical Information Agency Arlington Hall Station Arlington 12, Virginia Attn: TIPCR	10
Commander AF Research Division Washington 25, D.C. Attn: RRRTL	2	Director of Research and Development Headquarters USAF Washington 25, D.C. Attn: AFDRD	1
Commander Wright Air Development Division Wright-Patterson Air Force Base Ohio Attn: WWAD	4	Office of Naval Research Department of the Navy Washington 25, D.C. Attn: Code 420	1
Commander AF Cambridge Research Laboratories Laurence G. Hanscom Field Bedford, Massachusetts Attn: CRREL	1	Director, Naval Research Laboratory Washington 25, D.C. Attn: Technical Information Officer	1
Commander Rome Air Development Center Griffiss Air Force Base Rome, New York Attn: RCOIL-2	1	Director, Army Research Office Department of the Army Washington 25, D.C. Attn: Scientific Information Branch	1
Commander Detachment 1 Hq AF Research Division The Shell Building Brussels, Belgium	2	Chief, Physics Branch Division of Research U. S. Atomic Energy Commission Washington 25, D.C.	1
P. O. Box AA Wright-Patterson Air Force Base Ohio	1	U. S. Atomic Energy Commission Techinical Information Extension P. O. Box 62 Oak Ridge, Tennessee	1
Aeronautical Research Laboratories Building 450 Wright-Patterson Air Force Base Ohio Attn: Technical Library	1	National Bureau of Standards Library Room 203, Northwest Building Washington 25, D.C.	1
Physics Program National Science Foundation Washington 25, D.C.	1	Director, Department of Commerce Office of Technical Services Washington 25, D.C.	1

Agency	cc	Agency	cc

Director, Office of Ordnance   1
   Research
Box CM, Duke Station
Durham, North Carolina

ARO, Inc.   1
Arnold Air Force Station
Tullahoma, Tennessee
Attn: AEDC Library

Commanding General   1
U. S. Army Signal Corps Research
   and Development Laboratory
Fort Monmouth, New Jersey
Attn: SIGFM/EL-RPO

Advanced Research Projects Agency   1
Washington 25, D.C.

Commander   1
AF Special Weapons Center
Kirtland Air Force Base
New Mexico
Attn: SWOI

Commander   1
AF Missile Development Center
Holloman Air Force Base
New Mexico
Attn: HDOI

Commander   1
Army Rocket and Guided Missile
   Agency
Redstone Arsenal
Alabama
Attn: ORDXR-OTL

Commandant   1
Air Force Institute of Technology
   (AU) Library
MCLI-LIB, Bldg. 125, Area B
Wright-Patterson Air Force Base
Ohio

NONGOVERNMENTAL

Professor Donald C. Stinson   1
Electrical Engineering Department
University of Arizona
Tucson 25, Arizona

Commander
Air Research and Development
   Command
Andrews Air Force Base
Washington 25, D.C.
Attn: RDR   2 cys
       RDRA   1 cy
       RDRB   1 cy
       RDRC   1 cy
       RDRS   1 cy

National Aeronautics and Space   6
   Administration
Washington 25, D.C.

Commander   1
AF Flight Test Center
Edwards Air Force Base
California
Attn: FTOTL

Rand Corporation   1
1700 Main Street
Santa Monica, California

Chairman   1
Canadian Joint Staff
For DRB/DSIS
2450 Massachusetts Ave., N.W.
Washington 25, D.C.

Commander   1
AF Cambridge Research Laboratories
Office of Aerospace Research
Laurence G. Hanscom Field
Bedford, Massachusetts
Attn: CROOTR

Applied Mechanics Reviews   1
Southwest Research Institute
8500 Culebra Road
San Antonio 6, Texas

University of Southern California 1
Electrical Engineering Department
Los Angeles 7, California
Attn: Z. Kaprielian

Institute of the Aeronautical 1
  Sciences
2 East 64th Street
New York, New York
Attn: Librarian

Dr. J. T. Senise 1
Instituto Tecnológico de Aeronáutica
São José dos Campos
São Paulo, Brazil

Air Force Office of Scientific 5
  Research
Washington 25, D.C.
Attn: SRYP

Radio Research Laboratory 1
Kokubunji P. O.
Tokyo, Japan

Dr. Bertram A. Mulcahy 6
Chief, Division of Research
  Information
National Aeronautics and Space
  Administration
1520 H. Street Northwest
Washington 25, D.C.

Dr. A. L. Cullen 1
Department of Electrical Engineering
University of Sheffield
St. George's Square
Sheffield 1, England

Dr. W. R. Luebke 1
Supporting Research Group
Eitel-McCullough, Inc.
301 Industrial Way
San Carlos, California

Stanford Research Institute 1
Menlo Park, California
Attn: Documents Center

Professor R. W. Gould 1
Electron Tube Laboratory
California Institute of Technology
Pasadena, California

Dr. C. W. Barnes 1
Senior Research Engineer
Electron Devices Laboratory
Stanford Research Institute
Menlo Park, California

Raytheon Company 1
Research Division
28 Seyon Street
Waltham 54, Massachusetts

General Electric Company 1
Power Tube Department
Electronic Components Division
Building 267, Room 205
One River Road
Schenectady 5, New York

The Science Library 1
Science Museum
South Kensington, London, S.W. 7
England

Dr. Hellmut Golde 1
Department of Electrical Engineering
University of Washington
Seattle 5, Washington

Dr. P.J.B. Clarricoats 1
Department of Light Electrical
  Engineering
The Queen's University
Belfast, Northern Ireland

Philips Laboratories 1
A Division of North American
  Philips Company, Inc.
Irvington-on-Hudson, New York

Wayland D. George 1
Hughes Aircraft Company
Radiation Systems Department
Culver City, California

The University of British Columbia 1
Department of Electrical Engineering
Vancouver 8, British Columbia
Canada
Attn: Dr. G. B. Walker

Oxford University 1
Oxford, England
Attn: H. Motz

Agency	cc	Agency	cc
AVCO Manufacturing Corporation Research and Advanced Development Division Wilmington, Massachusetts Attn: E. Carnevale	1	University of Minnesota Electrical Engineering Department Minneapolis 14, Minnesota Attn: H. Oskam	1
Northeastern University Physics Department Boston, Massachusetts Attn: G. Lanza	1	Dr. J. E. Drummond Head Plasma Physics Laboratory Boeing Scientific Research Laboratories Boeing Airplane Company P. O. Box 3707 Seattle 24, Washington	1
Philip S. Carter, Jr. Stanford Research Institute 333 Ravenswood Avenue Menlo Park, California	1	Stevens Institute of Technology Physics Department Hoboken, New Jersey Attn: W. Bostick	1
Dr. E. Nalos General Electric Research Laboratory European Office Pelikan Strasse 37 Zurich, Switzerland	1	University of New Hampshire Department of Physics Durham, New Hampshire Attn: L. Mower	1
SFD Laboratories 800 Rahway Avenue Union, New Jersey Attn: J. A. Saloom, President	1	University of California Electronics Research Laboratory Berkeley 4, California Attn: J. Whinnery	1
Dr. M. O. Bryant S.E.R.L. (Admiralty) West Road, Harlow Essex, England	1	Rutgers University Microwave Laboratory New Brunswick, New Jersey Attn: M. Sirkis	1
University of Illinois Department of Electrical Engineering Urbana, Illinois Attn: P. Coleman	1	Office of Naval Research, New York 346 Broadway New York 12, New York Attn: I. Rowe	1
Columbia University Radiation Laboratory New York 27, New York Attn: C. Townes	1	New York University Institute of Mathematical Sciences 25 Waverly Place New York 3, New York, Attn: M. Kline	1
California Institute of Technology Electrical Engineering Department Pasadena 4, California Attn: C. Papas	1	Dr J. C. Anderson Laboratories RCA, Limited An Associate Company of Radio Corporation of America Zurich 5, Switzerland	1
Brooklyn Polytechnic Institute Microwave Research Institute 55 Johnson Street Brooklyn 1, New York Attn: N. Marcuvitz	1	Professor Elie Roubine 78, Avenue des Ternes-XVII Paris, France	1

Agency	cc	Agency	cc

W. E. Cantrell 1
Senic Engineer
Operational and Systems Analysis
Vought Electronics
P. O. Box 1500
Arlington, Texas

Mr. H. Wilhelmsson 1
Research Laboratory of Electronics
Chalmers University of Technology
Gibraltargatan 5 G
Gothenburg, Sweden

J. W. Nielson, Manager 1
Solid State Materials Laboratory
Research Center for the Airtron
    Division of Litton Industries
200 East Hanover Avenue
Morris Plains, New Jersey

Research and Development 1
Bomac Laboratories, Inc.
Salem Road
Beverly, Massachusetts
Attn: Arthur McCoubrey, Manager

L. F. Broadway, Head 1
Research Laboratories
Electrical and Musical Industries,
    Limited
Blyth Road, Hayes
Middlesex, England

Dr. J. G. Linhart 1
Euratom Plasma Physics Group
Instituto di Fisica dell' Universita
Piazzale delle Scienze 5
Rome, Italy

The Electronics Department 1
Royal Institute of Technology
Stockholm, Sweden
Attn: Care of the Librarian

Dr. R. Shersby Harvie 1
SERL
Baldock, Herts
England

J. Van Bladel 1
The University of Wisconsin
Department of Electrical Engineering
Madison 6, Wisconsin

Applied Physics Laboratory 1
The Johns Hopkins University
8621 Georgia Avenue
Silver Springs, Maryland
Attn: Library

Christina Walsh 1
Research Laboratory of Electronics
Chalmers Institute of Technology
Gothenburg, Sweden

H. Okanobori, Chief 1
Planning Section
The Radio Research Laboratories
Ministry of Ports and Tele-
    communications
Kokubunji, P. O., Koganei-shi
Tokyo, Japan

Dr. Gunter Ecke
Institut fur Theoretische . ... .
Universitat
Bonn, West Germany

Max-Plank Institute of Physics 1
and Astrophysics
Munich, West Germany
Attn: Care of the Librarian

Professor G. K. Emeleus 1
Queen's University
Belfast, Northern Ireland

Dr. J. E. Allen 1
CNRN Laboratorio Gas Ionizzati
Instituto di Fisica dell' Universita
Piazzele delle Scienze 5
Rome, Italy

Dr. Bertil Agdur 1
Microwave Department
Royal Institute of Technology
Stockholm, Sweden

Professor H. W. Konig 1
Institut fur Hochfrequenztechnik
Technischen Hochschule
Wien, Austria

The Oak Ridge National Laboratory 1
Central Research Laboratory
P. O. Box X
Oak Ridge, Tennessee